

NANOSCALE REAGENTS FOR THE DETECTION AND TREATMENT OF
TUBERCULOSIS IN RESOURCE LIMITED REGIONS

by

CANDICE ASHLEY SMITH

B.S., University of Michigan, 2009

A thesis submitted to the
Faculty of the Graduate School of the
University of Colorado in partial fulfillment
of the requirement for the degree of
Doctor of Philosophy
Department of Chemistry and Biochemistry

2015

This thesis entitled:
Nanoscale Reagents for the Detection and Treatment of Tuberculosis in
Resource Limited Regions
written by Candice Ashley Smith
has been approved for the Department of Chemistry and Biochemistry

Daniel Feldheim

Date November 9, 2015

The final copy of this thesis has been examined by the signatories, and we
Find that both the content and the form meet acceptable presentation standards
Of scholarly work in the above mentioned discipline.

IACUC protocol # 1110.01

ABSTRACT

Smith, Candice Ashley (Ph.D., Chemistry)

Nanoscale Reagents for the Detection and Treatment of Tuberculosis in Resource Limited Regions

Thesis directed by Professor Daniel Feldheim

Tuberculosis (TB) remains the second deadliest infectious disease after HIV/AIDS. TB most stubbornly has been spreading in resource limited regions. People in these regions need diagnostics and therapeutics tailored to their available resources. Developing countries would best benefit from a diagnostic that is robust, gives quick results, and requires minimal electricity or materials. Likewise, a high impact therapeutic for these communities would promote patient compliance through oral administration and low toxicity. In this thesis work, these challenges are confronted by development of an orally bioavailable gold nanoparticle platform, a surface enhanced Raman spectroscopy assay for the detection of an TB biomarker in urine, and isolating modified-aptamers affinity reagents for the detection of TB biomarkers in urine.

DEDICATION

Some of my greatest lessons came from humbling and humiliating experiences. No matter the intent, I am grateful for every single one of those lessons both in my life and in this graduate school experience. They have made me a stronger person. I have such love for those of you that show me unconditional kindness. You continuously inspire me, remind me to balance my life, and provide the occasional helping hand to lift my chin up. Thank you. I love you. I will never be alone, because of the impact you all have made in my life.

Table of Contents

Chapter 1: Tuberculosis Incites Call for New Diagnostics and Therapeutics	1
1.1. Tuberculosis a Persistent Disease.....	1
Figure 1.1. Ancient Native American mummy infected by <i>Mycobacterium tuberculosis</i>	1
Figure 1.2. (A) Estimated prevalence of TB cases (in millions per year), for 1990-2013. (B) The documented global MDR-TB cases detected (blue) and TB cases enrolled in MDR-TB treatment (red), 2009-2013. Adapted from World Health Organization report.	2
Figure 1.3. Confocal Microscopy image of <i>Mycobacterium tuberculosis</i> stained pink by the Ziehl-Neelsen technique	3
1.2 Source of a Tuberculosis infection.....	3
1.3 Detection of Tuberculosis in Resource Limited Communities.....	4
1.4 Treatment and Consequences of Not Curing TB	7
Figure 1.5. Estimated number of missed cases in millions for the top-ten countries, 2013. The range shows the lower and upper bounds of the 95% uncertainty interval. The bullet marks the best estimate.	7
Figure 1.6. Adapted image to show a representation for in cost and volume differences of medications used for treatment a drug sensitive strain of TB versus a MDR-TB infection. ¹⁶⁷ .	9
1.4 Project 1: Urine-Based Assay for the Detection of <i>Mtb</i>	10
1.5 Project 2: Oligonucleotide Aptamers for the Detection of Biomolecules	11
Figure 1.4. Aptamers conjugated to a gold surface. (A) An misfolded aptamer and (B) A refolded DNA aptamers bound to its target biomarker.	11
1.6 Project 3: Tuning the Oral Bioavailability of Gold Nanoparticles for potential <i>Mtb</i> Antimicrobials	12
1.6.1. Orally Administered Drug Route for Developing Countries	12
1.6.2 Gold Nanoparticles as Antimicrobials for Infectious Disease	12
1.7 Conclusion.....	14
Chapter 2: Surface Enhanced Raman Spectroscopy (SERS) Immunoassay for the Detection of Mannose Capped Lipoarabinomannan	16
2.1 Introduction.....	16
2.1.1 SERS immunoassay	17
2.1.2 ManLAM as Biomarker in Urine.....	19
Figure 2.2: (A) Dithiobis[succinimidyl propionate] molecule used to adsorb the antibody to the gold platform. (B) 5,5'-dithiobis(succinimidyl-2-nitrobenzoic acid) (DSNB) molecule that is	

chemisorbed to the gold nanoparticle surface and binds antibody after a reaction with the molecule's NHS ester moiety.....	19
Figure 2.3. A representation of ManLAM and all of its components from the mannose caps to its fatty acid tails. This image has been reproduced with permission of De Prithwiraj from the Chatterjee Lab at Colorado State University.	20
2.2 Results and Discussion	20
2.2.1 Assay Optimization	21
2.4 SERS immunoassay dose-response curve using non-endemic urine spiked with ManLAM without sample pretreatment.	21
Figure 2.5 The optimized pretreatment scheme for urine samples used in the SERS assay..	23
Figure 2.6 Calibration of the the SERS assay utilizing 0.1% tween-20 (orange), 0.05% (green), or 0.01% tween-20 (blue) circles.	24
2.2.2 Optimized Calibration Curve of ManLAM Standards	25
Figure 2.7. SERS immunoassay for urine spiked with ManLAM.	25
2.2.3 Comparison of SERS versus Culture Results for Patient Samples.....	26
Figure 2.8. Dose-response ($\nu_s(\text{NO}_2)$ at 1336 cm^{-1}) curves for the detection of ManLAM spiked into non-endemic urine.	26
2.3 Conclusion.....	28
2.4 Experimental Methods	28
2.4.1 Reagents	28
2.4.2. Preparation of ERLs.....	29
2.4.3 Capture substrate preparation.....	30
2.4.4 Preparation of Calibration Standards.....	31
2.4.5 Preparation of Urine Samples	31
2.4.6 Instrumentation	32
Chapter 3: Modified-Oligonucleotide Affinity Reagents for the Detection of Mycobacterium Tuberculosis Biomarkers in Urine.....	33
3.1 Introduction.....	33
3.2 TB biomarkers	34
3.3 SELEX with Modified-Nucleotides	35
Figure 3.1 A molecular representation of a modified thymidine nucleotide incorporated into aptamers in this project. R indicates the modifications: (A) tryptyl amino, (B) Naphthyl, and (C) 4-pyridyl.....	36
Figure 3.2 A SELEX for a target functionalized to bind a magnetic bead.	38
3.4 Results and Discussion	38

3.4.1 Target Preparation	39
3.4.2 Selection	40
Figure 3.3. A PCR trace from round 6 of the MT3444 selection. The maroon trace is from the target pool, and it drops low in cycle 13 after the sample was removed from the instrument. The navy trace is the negative control pool. The pink trace is pcr control to determine when or if the primers are interacting with each other.	41
3.4.3 Sequence Analysis of Evolved Pool	42
Figure 3.4 Summary of the computational analysis data from the evolved pool of a selection on MT2462. (A) The total number of sequences before and after quality filtering. (B) families on the X-axis and the size of their family on the Y-axis. (C) Conserved regions of highly populated families. Also, the mostly conserved nucleotides have the largest amplitude.	44
3.4.4 Binding Affinity and Specificity.....	45
Figure 3.5 Fluorescence polarization anisotropy assay. (A) The excited emission from a fluorophore labeled aptamer remains depolarized as it rapidly tumbles in solution, until (B) the aptamer binds the target which slows tumbling and causes the signal to remain polarized....	47
Figure 3.6. FPA assay binding curve of sequence N18 for its target MT3444 in selection buffer. The dissociation constant was determined by a non-linear regression program, Graphpad prizm, to be 34.9 ± 15.5 nM.....	51
Figure 3.7. FPA assay binding curve of sequence N18 for its target MT3444 in non-endemic urine. The binding curve for this assay has a larger dissociation constant and each point has a larger standard deviation The dissociation constant was determined to be approximately 121 nM.	52
Figure 3.8. FPA assay binding curve of sequence N18 for its target MT3444 in urine dialyzed against selection buffer for 24 hours. The dissociation constant was determined to be approximately 92 nM.	52
Figure 3.9 Tryptophan quenching affinity assay for sequence binding to the MT3444 protein. The dissociation constant for this assay was approximately $69 \text{ nM} \pm 44 \text{ nM}$	53
3.5 Conclusions and Future work	54
3.6 Methods and Materials	55
3.6.1 Polymerase Chain Reaction	55
3.6.2 Primer Extension.....	55
3.6.3 Selection Incubation and Partitioning	56
3.6.4 Cloning and Sequencing	56
3.6.5 Biotinylation of ManLAM.....	57
3.6.7 Fluorescence Polarization Anisotropy	57
3.6.8 Tryptophan Quenching Assay	58
3.6.9 Protein Expression and Purification.....	58

Chapter 4: Oral Bioavailability of 2.0 nm Diameter Gold Nanoparticles	59
4.1 Introduction.....	59
4.1.1 Potential of Gold Nanoparticle Use in Medicine.....	59
4.1.2 Oral Administration of Gold Nanoparticles	59
4.2 Oral Bioavailability Study of 2.0 nm Gold Nanoparticles	60
4.2.1 Design of Gold Nanoparticle Monolayer	60
Figure 4.1. Structural illustrations of cyclic disulfide-terminated polyethylene glycol ligands.	61
4.2.2 Stability and Characterization Studies of the Gold Conjugates.....	62
Figure 4.2. Gold nanoparticle stability assay simulating the pH and temperature of the human gastrointestinal tract. UV-Visible spectra of (A) PEG4-Acid, (B) PEG4-Neutral, (C) GSH, and (D) pMBA on ca. 2.0 nm diameter gold nanoparticles. See Experimental Methods section for further details.	63
Figure 4.3. Transmission electron micrographs and size dispersity statistics of gold nanoparticles modified with (A) pMBA, (B) GSH, (C) PEG4N/GSH, and (D) PEG24N/GSH. ..	64
Figure 4.4. ¹ H NMR spectra for a stackplot of PEG4N ligand/ PEG4N Au NP/ GSH Au NP. As the stackplot shows, there is signal from the PEG4N ligand on the gold surface and an absence of GSH signal.	65
4.2.3 <i>In Vivo</i> Oral Bioavailability and Distribution in the Mouse Model.....	66
Figure 4.5. Gold accumulation in blood and urine over a 24-hr period. Samples were collected at 1-hr, 8-hr, and 24-hrs and the gold concentrations measured at each time point summed to generate the bars shown. Gold concentrations were undetectable in all administrations except for the PEG4 ligands.	67
Figure 4.6. Gold distribution in the kidneys and liver for gold nanoparticles administered orally. Detectable concentrations of gold were noted for PEG ₄ and PEG ₁₂ modified particles, indicating absorption in the GI tract. PEG ₄ had the highest accumulation of all formulations, indicating PEG length may be responsible for gastrointestinal absorbance. No gold was detected for the other modified nanoparticles.	68
Figure 4.7. Analysis of mouse urine after oral administration of 60 μ M PEG4N gold nanoparticles. Transmission electron microscope image of the putative gold nanoparticles concentrated from urine and their size dispersity.	69
Figure 4.8. Fecal and gastrointestinal distribution of gold nanoparticles. Samples were collected at 1-hr, 8-hr, and 24-hrs and the gold concentrations measured at each time point summed to generate the bars shown. Nanoparticle concentrations were 60 μ M except where indicated.	70
4.3. Development of a Drug Conjugate with Limited Oral Bioavailability	72
4.3.1 Collaboration and Intellectual Property Protection	72
4.3.2 Limiting Oral Bioavailability of a 2.0 nm Drug Gold Nanoparticle Conjugate	72

4.3.3 Synthesis of Disulfide Drug Ligand.....	73
4.3.4 Place-Exchange of Drug Molecule onto Gold Nanoparticle Surface	73
4.3.5 Characterization and Purification of Drug Gold Conjugate.....	74
Figure 4.9. A polyacrylamide gel demonstrating the differences in migration, which is dependent on the gold nanoparticle monolayer composition. Gold nanoparticle sample in lane (A) is <i>p</i> -MBA gold nanoparticles and lane (C) are <i>p</i> -MBA gold nanoparticles with drug conjugated to their surface. Sample in lane (B) are GSH-coated gold nanoparticles and lane (D) are glutathione and drug gold conjugate. The gel is not stained in any way, the image shows actual gold nanoparticles visible as a group migrating through the gel.....	76
Figure 4.10. TEM images of gold nanoparticle conjugates. In image (A) are GSH drug gold conjugates and image (B) are <i>p</i> -MBA drug gold conjugates. Note the stock GSH and <i>p</i> -MBA utilized and their images can be referenced in Figure 3.3.....	77
4.3.6 Stability of Drug Gold Conjugates	78
Figure 4.12. GI tract simulation study UV-Vis spectrum used to determine stability of the GSH drug gold conjugate in an environment similar to the human GI tract.....	80
Figure 4.11. Cell Culture Media Assay that monitored of the absorbance at the surface plasmon resonance wavelength max at 510 nm of the 2.0 gold nanoparticles. Navy absorbance values are gold drug conjugate with a GSH base monolayer. Gold absorbance values are unconjugated stock GSH gold nanoparticles.	81
4.3.7 <i>In Vitro</i> assays with Drug Gold Conjugate	81
4.3.8 <i>In vivo</i> studies With the Drug Gold Conjugate	82
Figure 4.13. Biodistribution data of organs and excrement of three mice administered one 200 μ L dose of 60 μ M gold nanoparticle conjugate. Note the intestine samples of mouse 2 is only a fraction of the total sample due to a sample processing error.....	83
Figure 4.14. Time course of gold concentration in serum after 3 mice were treated with a single dose of the drug gold conjugate. Note the serum gold concentrations are several orders of magnitude lower than the pegylated gold conjugates of the early bioavailability study in chapter 3.	83
4.4 Conclusions and Future Directions	84
4.5 Methods and Materials	85
4.5.1 Synthesis of gold nanoparticles.....	85
4.5.2 Place-exchange of PEG onto glutathione gold nanoparticles	86
4.5.3 Place-exchange of Lilly Drug onto 2.0 gold nanoparticles	87
4.5.4 Gold Nanoparticle Stability Assay in Cell Culture Media.....	88
4.5.5 Nuclear Magnetic Resonance spectroscopy (NMR)	88
4.5.6 Transmission Electron Microscopy (TEM)	88
4.5.7 Animal Models	89

4.5.8 Sample Collection and Preparation	90
4.5.9 Inductively Coupled Plasma-Mass Spectrometry (ICP-MS) analysis	90
4.5.10 Aggregation study using relative stomach and intestinal pH.....	90
4.5.11 Polyacrylamide Gel Electrophoresis	91
Chapter 5: Toxicity and Bioavailability of Potential Gold Nanoparticle Antibiotics <i>in vivo</i>	92
5.1 Introduction.....	92
Figure 5.1. Core library of thiols used to create mixed ligand monolayers on the gold nanoparticle conjugates.....	92
5.1.1 Small Variable Ligand Display Antimicrobials.....	92
5.2 Results and Discussion	94
5.2.1 Initial <i>in vivo</i> Toxicity and Biodistribution of LAL-32	94
Figure 5.2. Ligands of LAL-32 are glutathione (5), cystamine (6), and 3-mercapto-1-propanesulfonate (8). and LAL-32EG also includes ligand EG.	95
Figure 5.3. Biodistribution data of blood, urine, and organ data. The 10 uM concentration has biodistribution data from 24 hour through 12 weeks. However, the 60 uM concentration has organ data for only the first 24 hours.....	96
Figure 5.4. Microscopy images of mouse renal samples: (A) control mouse administered 0 μ M gold nanoparticle solution of buffer only, (B) mouse administered 10 uM dose of LAL-32, (C) mouse administered 60 uM dose of LAL-32.....	97
5.2.2 Modifying LAL-32 with Polyethylene glycol.....	98
Figure 5.6 Blood half-life graph for 60 μ M injection of LAL-32EG gold conjugate.....	99
Figure 5.7. Urine and Blood clearance of LAL-32EG from mice during a 24-hour time period. Blue indicates individual data values, and square points indicate the average gold concentration per time period.	100
5.3 Conclusions & Discussion	101
Figure 5.8. Organ distribution data for a 60 uM injection of LAL-32EG from 24 hours through 12 weeks.	101
5.4 Methods and Materials	102
5.5.1 Synthesis of gold nanoparticles.....	102
5.5.2 Place exchange reactions	103
5.5.3 Animal protocols.....	104
5.5.4 Inductively Coupled Plasma Mass Spectrometry (ICP-MS)	105

Appendix

A.	Supplemental Graphs and Images.....	125
----	-------------------------------------	-----

Tables

Table 2.1 SERS Detection of ManLAM in Endemic FIND samples.	27
Table 2.2 SERS Detection of ManLAM in Endemic FIND Samples (corrected for possible extrapulmonary TB cases).	27
Table 3.1 Aptamer Dissociation Constants (nM) for Specific TB Biomarkers.	50
Table 5.1. Gold Conjugates and their MIC _{99.9} values for specific bacteria.....	96

Equations

Eq 3.1 Perrin equation.....	47
Eq 3.2 Debye Rotational Relaxation Time Constant.	47
Eq 3.2 Dissociation Constant.	49

Figures

Chapter 1

Figure 1.1. Ancient Native American mummy determined to be infected by <i>Mycobacterium tuberculosis</i>	1
Figure 1.2. (A) Estimated prevalence of TB cases (in millions per year), for 1990-2013. (B) The documented global MDR-TB cases detected (blue) and TB cases enrolled in MDR-TB treatment (red), 2009-2013. Adapted from World Health Organization report.	2
Figure 1.3. Confocal Microscopy image of <i>Mycobacterium tuberculosis</i> stained pink by the Ziehl-Neelsen technique.....	3
Figure 1.4. Aptamers conjugated to a gold surface. (A) An misfolded aptamer and (B) A refolded DNA aptamers bound to its target biomarker.	7
Figure 1.5. Estimated number of missed cases in millions for the top-ten countries, 2013. The range shows the lower and upper bounds of the 95% uncertainty interval. The bullet marks the best estimate.	9
Figure 1.6. Adapted image to show a representation for in cost and volume differences of medications used for treatment a drug sensitive strain of TB versus a MDR-TB infection.	11

Chapter 2

Figure 2.1: SERS assay scheme for the detection of ManLAM in urine	18
Figure 2.2: (A) Dithiobis[succinimidyl propionate] molecule used to adsorb the antibody to the gold platform. (B) 5,5'-dithiobis(2-nitrobenzoic acid) (DSNB) molecule that is chemisorbed to the gold nanoparticle surface and binds antibody after a react with the molecule's NHS ester moiety.	19
Figure 2.3. A representation of ManLAM and all of its components from the mannose caps to its fatty acid tails. This image has been reproduced with permission of De Prithwiraj from the Chatterjee Lab at Colorado State University. .	20
2.4 SERS immunoassay dose-response curve using non-endemic urine spiked with ManLAM without sample pretreatment.	21
Figure 2.5 The optimized pretreatment scheme for urine samples used in the SERS assay.	23
Figure 2.6 Calibration of the the SERS assay utilizing 0.1% tween-20 (orange), 0.05% (green), or 0.01% tween-20 (blue) circles.	24
Figure 2.7. SERS immunoassay for urine spiked with ManLAM.	25
Figure 2.8. Dose-response ($v_s(\text{NO}_2)$ at 1336 cm^{-1}) curves for the detection of ManLAM spiked into non-endemic urine.	26

Chapter 3

Figure 3.1 A molecular representation of a modified thymidine nucleotide incorporated into aptamers in this project. R indicates the modifications: (A) tryptyl amino, (B) Naphthyl, and (C) 4-pyridyl.....	36
Figure 3.2 A SELEX for a target functionalized to bind a magnetic bead.....	38
Figure 3.3. A PCR trace from round 6 of the MT3444 selection. The maroon trace is from the target pool, and it drops low in cycle 13 after the sample was removed from the instrument. The navy trace is the negative control pool. The pink trace is pcr control to determine when or if the primers are interacting with each other.	41
Figure 3.4 Summary of the computational analysis data from the evolved pool of a selection on MT2462. (A) The total number of sequences before and after quality filtering. (B) families on the X-axis and the size of their family on the Y-axis. (C) Templates of conserved regions of highly populated families with frequency of a specific nucleotide in a family by height. Thus the modified nucleotide will be represented by an A. Also, the mostly conserved nucleotides have the largest amplitude.	44
Figure 3.5 Fluorescence polarization anisotropy assay. (A) The excited emission from a fluorophore labeled aptamer remains depolarized as it rapidly tumbles in solution, until (B) the aptamer binds the target which slows tumbling and causes the signal to remain polarized.....	46
Figure 3.6. FPA assay binding curve of sequence N18 for its target MT3444 in selection buffer. The dissociation constant was determined by a non-linear regression program, Graphpad prizm, to be 34.9 nM.	51
Figure 3.7. FPA assay binding curve of sequence N18 for its target MT3444 in non-endemic urine. The binding curve for this assay has a larger dissociation constant and each point has a larger standard deviation The dissociation constant was determined to be approximately 121 nM.....	52
Figure 3.8. FPA assay binding curve of sequence N18 for its target MT3444 in urine dialyzed against selection buffer for 24 hours. The dissociation constant was determined to be approximately 92 nM.....	52
Figure 3.9 Tryptophan quenching affinity assay for sequence N18 binding to the MT3444 protein. The dissociation constant for this assay was approximately 69 nM \pm 44 nM.	53

Chapter 4

Figure 4.1. Structural illustrations of cyclic disulfide-terminated polyethylene glycol ligands.....	62
Figure 4.2. Gold nanoparticle stability assay simulating the pH and temperature of the human gastrointestinal tract. UV-Visible spectra of (A) PEG4-Acid, (B) PEG4-	

Neutral, (C) GSH, and (D) <i>p</i> MBA on ca. 2.0 nm diameter gold nanoparticles. See Experimental Methods section for further details.....	64
Figure 4.3. Transmission electron micrographs and size dispersity statistics of gold nanoparticles modified with (A) <i>p</i> MBA,(B) GSH, (C) PEG4N/GSH, and (D) PEG24N/GSH.....	65
Figure 4.4. ¹ H NMR spectra for a stackplot of PEG4N ligand/ PEG4N Au NP/ GSH Au NP. As the stackplot shows, there is signal from the PEG4N ligand on the gold surface and an absence of GSH signal.	66
Figure 4.5. Gold accumulation in blood and urine over a 24-hr period. Samples were collected at 1-hr, 8-hr, and 24-hrs and the gold concentrations measured at each time point summed to generate the bars shown. Gold concentrations were undetectable in all administrations except for the PEG4 ligands.....	68
Figure 4.6. Gold distribution in the kidneys and liver for gold nanoparticles administered orally. Detectable concentrations of gold were noted for PEG ₄ and PEG ₁₂ modified particles, indicating absorption in the GI tract. PEG ₄ had the highest accumulation of all formulations, indicating PEG length may be responsible for gastrointestinal absorbance. No gold was detected for the other modified nanoparticles.....	69
Figure 4.7. Analysis of mouse urine after oral administration of 60 uM PEG4N gold nanoparticles. Transmission electron microscope image of the putative gold nanoparticles concentrated from urine and their size dispersity.	70
Figure 4.8. Fecal and gastrointestinal distribution of gold nanoparticles. Samples were collected at 1-hr, 8-hr, and 24-hrs and the gold concentrations measured at each time point summed to generate the bars shown. Nanoparticle concentrations were 60 μM except where indicated.	71
Figure 4.9. A polyacrylamide gel demonstrating the differences in migration, which is dependent on the gold nanoparticle monolayer composition. Gold nanoparticle sample in lane (A) is <i>p</i> -MBA gold nanoparticles and lane (C) are <i>p</i> -MBA gold nanoparticles with drug conjugated to their surface. Sample in lane (B) are GSH-coated gold nanoparticles and lane (D) are glutathione and drug gold conjugate. The gel is not stained in any way, the image shows actual gold nanoparticles visible as a group migrating through the gel.	77
Figure 4.10. TEM images of gold nanoparticle conjugates. In image (A) are GSH drug gold conjugates and image (B) are <i>p</i> -MBA drug gold conjugates. Note the stock GSH and <i>p</i> -MBA utilized and their images can be referenced in Figure 3.3.....	78
Figure 4.12. GI tract simulation study UV-Vis spectrum used to determine stability of the GSH drug gold conjugate in an environment similar to the human GI tract. .	81
Figure 4.11. Cell Culture Media Assay that monitored of the absorbance at the surface plasmon resonance wavelength max at 510 nm of the 2.0 gold nanoparticles. Navy absorbance values are gold drug conjugate with a GSH base	

monolayer. Gold absorbance values are unconjugated stock GSH gold nanoparticles.82

Figure 4.13. Biodistribution data of organs and excrement of three mice administered one 200 μ L dose of 60 μ M gold nanoparticle conjugate. Note the intestine samples of mouse 2 is only a fraction of the total sample due to a sample processing error.....84

Figure 4.14. Time course of gold concentration in serum after 3 mice were treated with a single dose of the drug gold conjugate. Note the serum gold concentrations are several orders of magnitude lower than the pegylated gold conjugates of the early bioavailability study in chapter 3.....84

Chapter 5

Figure 5.1. Core library of thiols used to create mixed ligand monolayers on the gold nanoparticle conjugates.....93

Figure 5.2. Ligands of LAL-32 are glutathione (5), cystamine (6), and 3-mercapto-1-propanesulfonate (8). and LAL-32EG also includes ligand EG.96

Figure 5.3. Biodistribution data of blood, urine, and organ data. The 10 μ M concentration has biodistribution data from 24 hour through 12 weeks. However, the 60 μ M concentration has organ data for only the first 24 hours.97

Figure 5.4. Microscopy images of mouse renal samples: (A) control mouse administered 0 μ M gold nanoparticle solution of buffer only, (B) mouse administered 10 μ M dose of LAL-32, (C) mouse administered 60 μ M dose of LAL-32.....98

Figure 5.6 Blood half-life graph for 60 μ M injection of LAL-32EG gold conjugate. .100

Figure 5.7. Urine and Blood clearance of LAL-32EG from mice during a 24-hour time period. Blue indicates individual data values, and square points indicate the average gold concentration per time period.....101

Figure 5.8. Organ distribution data for a 60 μ M injection of LAL-32EG from 24 hours through 12 weeks.....102

LIST OF ACRONYMS

EID	Emerging Infectious Disease
CDC	Centers of Disease Control
WHO	World Health Organization
TB	Tuberculosis
<i>Mtb</i>	<i>Mycobacterium tuberculosis</i>
SERS	Surface Enhanced Raman Spectroscopy
DSNB	5,5'-dithiobis(2-nitrobenzoic acid)
CV	coefficient of variation
FDA	Food and Drug Administration
EG	ethylene glycol
PEG	polyethylene glycol
GSH	glutathione
K_d	dissociation constant
PCR	polymerase chain reaction
EID	emerging infectious disease
FPA	fluorescence polarization anisotropy
MOD	modified nucleotide
pMBA	<i>para</i> -mercaptobenzoic acid
SELEX	Systematic Evolution of Ligands by Exponential Enrichment
MDR-TB	multi-drug resistant tuberculosis
XDR-TB	extensively all drug resistant tuberculosis
TST	purified protein derived tuberculin skin test

Chapter 1: Tuberculosis Incites Call for New Diagnostics and Therapeutics

1.1. Tuberculosis a Persistent Disease

Tuberculosis (TB) is a bacterial infectious disease that has persistently burdened humans from antiquity and into the modern era despite research accomplishments made in diagnostics and treatments. Even in antiquity,

TB affected European populations and isolated peoples of the Americas alike, like the 500 year old Incan mummy in figure 1.1.^{1,2,3} Research efforts have resulted in control of other ancient infectious diseases, such as Smallpox, Cholera, Typhoid, or Malaria; However, TB remains the second deadliest infectious disease after HIV/AIDS.^{1,4,5} In 2013 alone, there were 9 million documented cases and 1.5 million people died of TB; furthermore, 95% of these new tuberculosis cases and 98% of the deaths



Figure 1.1. Ancient Native American mummy infected by *Mycobacterium tuberculosis*.¹⁶⁵

occurred in developing countries.⁴ Tuberculosis is a growing problem mainly in resource limited regions due to the development of antibiotic resistance to first line drugs, co-infection with an immune system suppressing pathogen, lack of access

to inexpensive high-quality diagnostics, and breakdowns in public health systems from influxes of populations and war in areas like the Middle East and Sub-Saharan Africa. Both drug resistance to antibiotics and the inability to correctly diagnose the disease are intimately linked issues for developing countries, and attention will be given to these specific issues and the basic knowledge of TB in the following chapter.

TB has become an emerging infectious disease (EID) again.^{6,7} EIDs are illnesses caused by pathogens that have seen an increase in incidence for the past two decades, or threaten to increase in the near future regardless of national boundaries.⁶ There are several factors that contribute to the emergence of infectious diseases: a spread to new geographical areas, evolution of resistance to medications, ecological changes, civil conflict, and other breakdowns in public health.⁶ New TB cases have begun to decrease, but antibiotic resistant TB cases are on the rise, as shown in Figure 1.2. If new infections of multi-drug resistant TB (MDR-TB) continue to increase, then overall cases of TB could also begin to

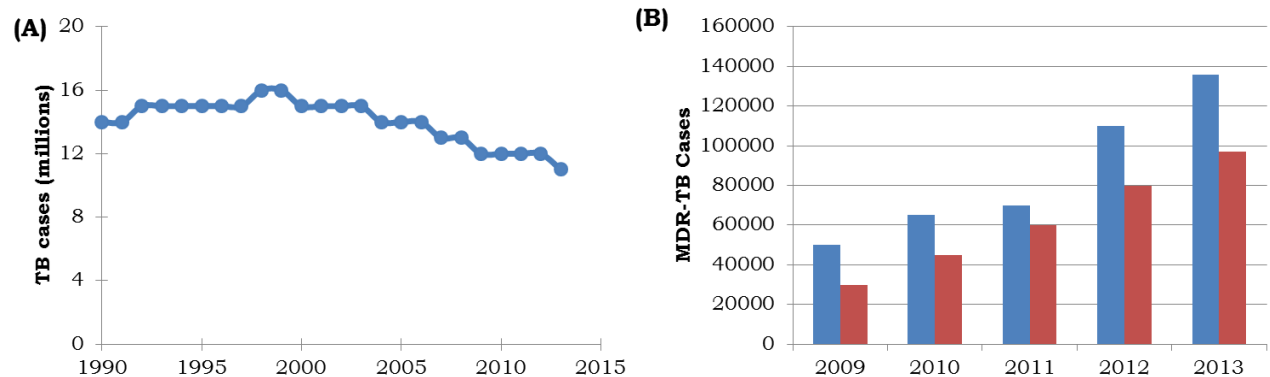


Figure 1.2. (A) Estimated prevalence of TB cases (in millions per year), for 1990-2013. (B) The documented global MDR-TB cases detected (blue) and TB cases enrolled in MDR-TB treatment (red), 2009-2013. Adapted from World Health Organization report.⁴

increase. TB as an EID is a problem of such importance that the World Health Organization (WHO) urges creation of national strategic plans and the Centers for Disease Control included it in a list of EID threat levels.^{8,9}

The WHO has been giving attention to the eradication of TB by carefully collecting data on the disease, disseminating progress reports and suggesting new objective goals. Their current goals are to reduce new tuberculosis cases by 90% and deaths by 95% worldwide by the year 2035 with 3 objectives: (1) improve and integrate patient care by diagnosing and treating all cases, (2) move forward with bold policies and support systems, and (3) intensify research and innovation.⁹ Based on the WHO's goals, it is important to intensify research in areas that benefit populations with the highest disease burden, which are marginalized communities of resource poor countries. In response, the following dissertation work has aimed to address the third WHO objective; to intensify research in order to diagnose and treat all cases. This dissertation work includes three main projects: Surface Enhanced Raman Spectroscopy assay for detection of a TB biomarker in urine, oligonucleotide affinity reagents for the detection of TB biomarkers in urine, and development of a gold nanoparticle drug platform.

1.2 Source of a Tuberculosis infection

Currently one third of the world's population is infected with

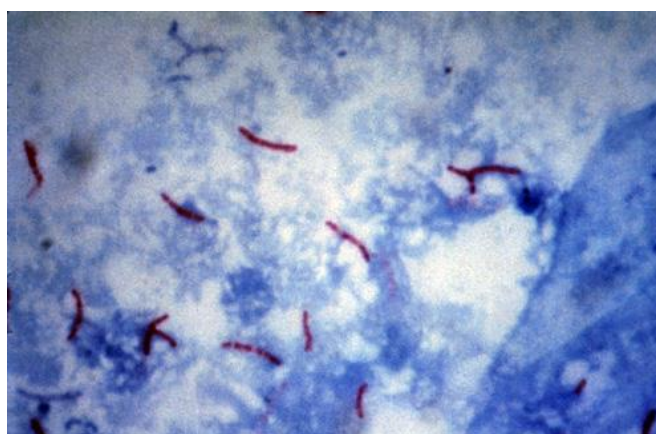


Figure 1.3. Confocal Microscopy image of Mycobacterium tuberculosis stained pink by the Ziehl-Neelsen technique.¹⁶⁶

Mycobacterium tuberculosis (*Mtb*) and up to 10% will present with TB in their lifetime.⁴ *Mtb* is the rod-shaped disease causing bacteria of TB as shown in Figure 1.3.¹⁰ Most incidences of *Mtb* infection occur in the lungs, but it may also present outside the lungs, for instance in the urinary tract or lymph nodes.¹¹ After a TB infection develops into the active disease in the lungs it can then be transmitted to other people by coughs containing droplets filled with *Mtb*.¹⁰ These droplets are part of a human lung secretion called sputum, and it could take as few as 25 bacteria to cause an infection in the non-human primates used as animal models.¹² *Mtb* infections often go undiagnosed unless a patient develops the disease TB.

1.3 Detection of Tuberculosis in Resource Limited Communities

Once *Mtb* infection is established the bacteria divide and multiply; consequently shedding biomolecules specific to *Mtb* that could be detected in order to diagnose a patient. Unfortunately in developing countries doctors must often rely on only a patient's clinical presentation or the sputum smear test.¹³ The sputum smear has been considered the gold standard TB diagnostic; even so, it achieves only 20-80% clinical sensitivity and up to 95% clinical specificity dependent on the laboratory and quality of specimen.¹⁴ Clinical sensitivity is the ability of the test to correctly identify a diseased individual; like-wise, clinical specificity is the ability for the test to correctly identify a non-diseased individual.¹⁵ The sputum smear test detects whole cell *Mtb* via staining of the bacteria from lung mucus samples, a.k.a. sputum. The sputum smear test requires a patient to provide two different sputum samples, and then wait up to 4 weeks for final interpretation of the laboratory results.¹⁶ However, some patients, such as babies

and HIV-positive patients, cannot provide high-quality sputum samples.¹⁴ If the patient has non-pulmonary TB, then the test cannot detect the pathogen. In addition, the sputum smear test is a labor intensive method and puts lab workers at risk of exposure to the pathogen.¹⁷ Ideally in resource limited regions, TB would be diagnosed via a non-invasive molecular detection method for each case, which maximizes safety and ease of sample collection while minimizing time to disease detection.

Diagnostics to detect *Mtb* biomarkers in patient fluid samples exist, but do not necessarily suited for resource poor communities. GeneXpert is a molecular-based diagnostic on the market with much higher specificity and sensitivity than sputum smear test.¹⁸ The GeneXpert actually detects *Mtb* genetic material from sputum samples in two hours by PCR amplification and without extensive sample processing compared to the sputum smear test.¹⁷ However it still requires sputum, and it is hard to collect quality samples from infants and those co-infected with HIV/AIDS. Additionally, despite price subsidies negotiated by health-care benefactors, GeneXpert is 20x higher in cost than the sputum smear test and thus too expensive for resource limited communities.^{17,19,20} Also it requires consistent electricity, security to protect patient data, and yearly calibration from a qualified technician, all of which is straining for resource-poor countries. Gene Xpert has a better clinical sensitivity and specificity than the gold standard TB diagnostic; however, it is expensive and requires a problematic fluid samples.

Other assays exist for biomarker detection of *Mtb*, such as immunoassays. These antibody based assays can be cheap, but often suffer from cross-reactivity and specificity issues.^{21,22,23} An example of poor analytical specificity is the Alere

Determine TB test. The Alere kit utilizes antibodies to detect a cellular component of TB in urine, however, the kit may give a false positive if the patient has a urinary tract infection. The sensitivity of this test is only 4% in healthy patients and up to 70% in immune suppressed individuals.²⁴ Another example, the tuberculin purified protein derivative test (TST) utilizes endogenous antibodies to detect immune responses of patients to mycobacterial antigens. In this test, TB and related mycobacterial proteins are injected under a patient's skin, if the patient has an allergic response, then the patient may be confirmed as having a TB infection; be that as it may this test can only confirm the patient has been exposed to a mycobacterial antigen.²¹ The TST may also give a false negative if the patient suffers from immune suppression.¹⁷ Other enzyme-linked sero-immunoassays detect possible endogenous antibodies of patients against Mtb. The WHO, strongly advises against use of serological assays, because they have highly variable sensitivity and specificity.^{23,25} In resource limited regions these tests are not ideal, because often reagents for antibody based assays require facilities with access to electricity for either refrigeration or to measure the results. Other prohibitive features of antibodies are their limited shelf life at ambient temperatures and can be expensive to isolate and purify in abundance. There is need for a better affinity reagent in TB diagnostics that does not suffer from the limitations of antibodies.

The best diagnostic for resource limited communities would have much greater clinical sensitivity compared to sputum smear tests, require minimal to no electricity for storage or use, provide results in less than 24 hours, be inexpensive, and require minimal expertise to operate on site.²⁶ The research in the following

chapters includes two possible sources to improve TB diagnostics. Thesis project 1 is a Surface Enhanced Raman assay developed to detect TB biomarkers in urine. Additionally, thesis project 2 proposes the use of modified oligonucleotide affinity reagents for the detection of *Mtb* biomarkers as an alternative to antibodies.

1.4 Treatment and Consequences of Not Curing TB

Unfortunately, not all new cases of TB are detected and many people go undiagnosed and untreated as Figure 1.5 displays.⁴ If these cases are not properly diagnosed, then the patient faces a high likelihood of dying from the disease. Misdiagnosed and untreated cases also increase the likelihood that *Mtb* strains can evolve resistance to the antibiotics used to treat TB. In the 1940s scientists

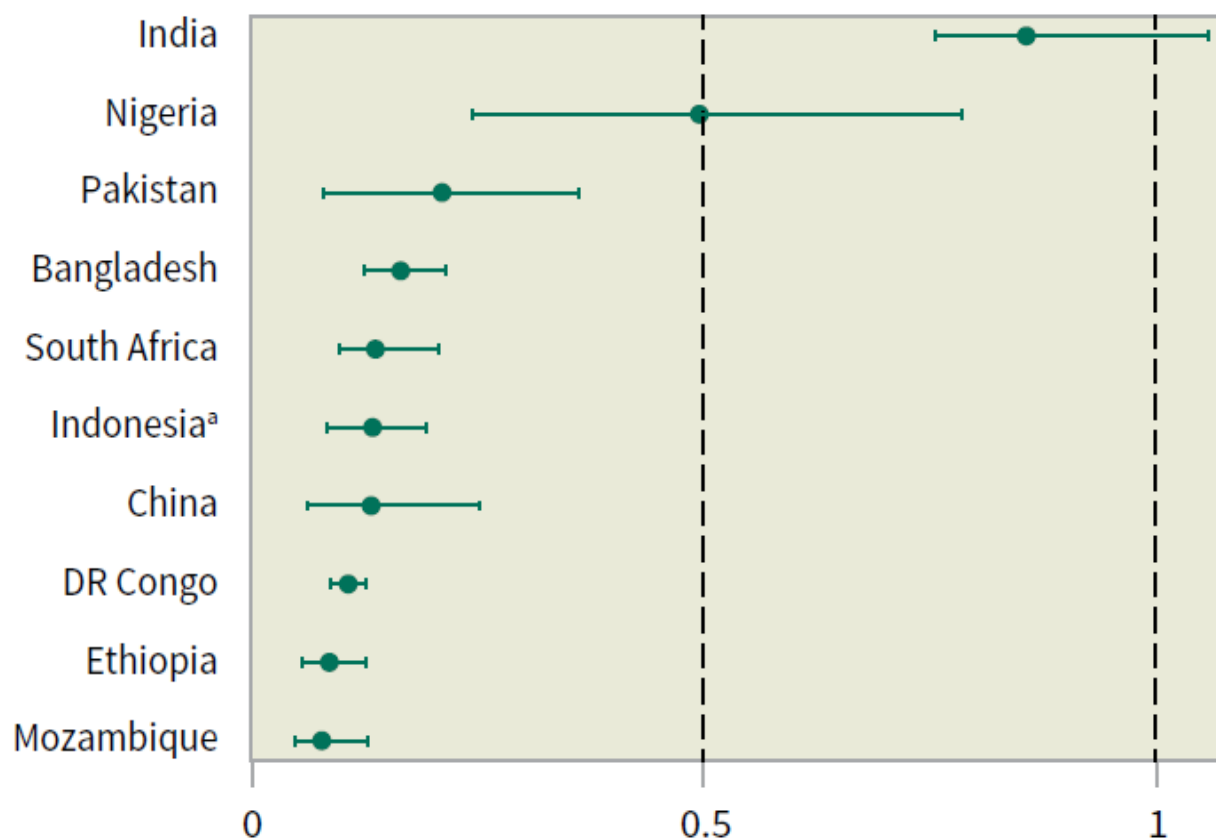


Figure 1.5. Estimated number of missed cases in millions for the top-ten countries, 2013. The range shows the lower and upper bounds of the 95% uncertainty interval. The bullet marks the best estimate.⁴

discovered Rifampicin and Isoniazid.²⁷ These drugs are the mainline antibiotics for the treatment of TB, and there has been little improvement beyond them in the past 70 years.²⁸ A patient is required to take daily doses of these medications for up to 9 months for them to eradicate most of the bacteria from the body.^{27,29} However, some patients cannot or do not follow the antibiotic regimen, or have contracted a strain of tuberculosis insensitive to the first line *Mtb* antibiotics. These strains of *Mtb* are called multi-drug resistant (MDR-TB), and treatment for these strains of *Mtb* require a minimum of 2 years of antibiotics, which often limits a patient to living near a clinic and enduring severe side effects from the drugs like vomiting, diarrhea, and permanent hearing loss.^{30,29} Some patients cannot afford financial or physical strains caused by the treatment; as a consequence, some quit treatment and return home. The burden of MDR-TB on developing countries is equally as heavy. For example, an MDR-TB patient requires more medical attention than patients with drug sensitive TB infections and just the antibiotics to treat MDR-TB are \$2000.00-3000.00 per patient, as compared to \$20 for treatment of patients with drug susceptible strains of *Mtb*.^{31,7} Figure 1.6 shows a visual representation of the differences between treating drug sensitive TB infections versus multi-drug resistant TB infections. Due to cost barriers and limited access to quality care some countries have to put these MDR-TB patients on a waitlist for treatment, a group that does not have the time to wait.


	Tuberculosis	Multidrug-resistant tuberculosis
Treatment	<p>2 months with 4 drugs</p>   <p>Followed by 4 months with 2 drugs</p> 	<p>8 months with 5 drugs and a shot</p>   <p>Followed by at least 20 months with 5 drugs</p> 
Total drugs consumed	854 pills swallowed	13,664 pills swallowed, 244 shots taken
Drug cost	\$20	\$2,500 to \$3,000
Possible side effects	Rashes, nausea, liver failure	Permanent hearing loss, permanent dizziness, kidney damage, psychosis, liver failure, nausea, rashes
Side effect rates	5 to 10 percent have mild to serious side effects	At least 33 percent of patients have serious side effects

Figure 1.6. Adapted image to show a representation for in cost and volume differences of medications used for treatment a drug sensitive strain of TB versus a MDR-TB infection.¹⁶⁷

Currently, 20% of patients with MDR-TB survive through the entire course of treatment.⁷ In addition to MDR-TB there are even strains that are resistant to essentially all antibiotics currently on the market for *Mtb* treatment and are called XDR-TB. The survival rate of patients with XDR-TB is only 2%.⁷ If antibiotics used for the treatment of *Mtb* had shorter courses of treatment and fewer side

effects, then it may decrease mortality caused by the disease and lower incidences of drug resistant tuberculosis. Now more than ever it is important to develop new therapeutics for *Mtb* that have shorter courses of treatment, are inexpensive, show lower toxicity, and allow patients to easily consume the medication orally. The third project of this dissertation is the development of an orally bioavailable gold nanoparticle platform for potential antimicrobials to *Mtb*. The description of this project will be described in section 1.5 of this chapter.

1.4 Project 1: Urine-Based Assay for the Detection of *Mtb*

Urine-based assays could be better for TB detection in resource poor communities. As a diagnostic fluid it can be collected in a non-invasive manner from universally any patient. It requires minimal equipment or expertise for collection, a sterile cup and depth perception, compared to other fluids such as blood. Urine harbors less whole *Mtb* bacteria than sputum or blood, which puts lab workers at lower risk when running urine-based diagnostic assays.³² Although there are few *Mtb* bacteria found in TB patient samples, biomolecules from *Mtb* are shed in the urine. Both cell wall components and proteins from *Mtb* have been detected in urine and could serve as potential biomarkers of TB.^{33–35} Mannose-capped Lipoarabinomannan (ManLAM) is the detectable cell wall component of *Mtb* found in urine that has been proven to be a biomarker in urine. Unfortunately, current lateral flow based assays have abysmal clinical sensitivity, often as low as 4–21%.^{35,36,24} The existing low clinical sensitivity ManLAM-based diagnostics leave a lot of room for improvement. Project 1 broaches the issue by the development of a urine-based assay for the detection of the ManLAM, which will be discussed further in chapter 2.

1.5 Project 2: Oligonucleotide Aptamers for the Detection of Biomolecules

Oligonucleotides affinity reagents could be an excellent alternative to

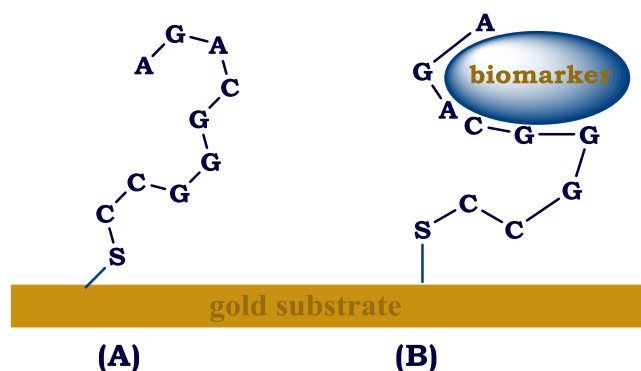


Figure 1.4. Aptamers conjugated to a gold surface. (A) An unfolded aptamer and (B) A refolded DNA aptamer bound to its target biomarker.

antibodies for TB diagnostics designed for resource limited regions.

As an alternative oligonucleotide aptamers have been found to be resilient to decomposition,

inexpensive to synthesize, and

have the ability to specifically bind a target. The aptamers are

polymers composed of either

deoxyribonucleic acids (DNA) or ribonucleic acids (RNA). They can be synthesized and purified in less than a day, in contrast to their antibody counterparts, which require weeks.^{37,38}

Additionally, chemical modifications to either the DNA or RNA sugar backbone or base may confer additional stability or more contacts between the aptamers and target.³⁷ Unlike antibodies, aptamers can be denatured and re-folded, while maintaining their capability to bind their targets, which a visualization of this is shown in Figure 1.4.³⁹ There has been evidence that aptamers also possess biomarker-binding capabilities on par or better than the corresponding antibodies. For example, an antibody for thrombin has a dissociation constant (K_d) of 56.7 nM and a DNA aptamer equivalent has a K_d of 19.8 nM.³⁹ A low K_d is a positive attribute for a diagnostic, because it means the aptamer binds tightly to its target allowing for better analytical sensitivity. Likewise, aptamers with a low K_d can withstand stringent wash steps in a

diagnostic which could improve specificity. These qualities of oligonucleotide aptamers are ideal for their utilization as a component in a potential tuberculosis diagnostic for resource limited regions. More information about the project and fundamentals of isolating modified-DNA aptamer affinity reagents to *Mtb* biomarkers will be described in chapter 3.

1.6 Project 3: Tuning the Oral Bioavailability of Gold Nanoparticles for potential *Mtb* Antimicrobials

1.6.1. Orally Administered Drug Route for Developing Countries

Developing an orally administered antibiotic therapy is of great importance for marginalized communities, because patient compliance will be higher and will not incur additional expense, like use and disposal of hypodermic needles for other common routes.⁴⁰ Another advantage is that packaging options have been developed for controlled release of pills taken by mouth, which could reduce how many pills and how often patients have to take medicine.⁴¹ One of the caveats of the oral route is permeability of the gastrointestinal tract or lack thereof. Optimization may be necessary when pursuing an oral bioavailable route for a potential drug. A good therapeutic for resource limited regions should include an option for oral administration.

1.6.2 Gold Nanoparticles as Antimicrobials for Infectious Disease

Gold nanoparticles would be a beneficial drug platform, because their use has been shown to be non-toxic depending on the ligand conjugated to its surface. Some other metal nanoparticles composed of copper or silver can have inherent antimicrobial properties.⁴² Unlike these nanoparticles, the gold nanoparticle requires a ligand capping system on its surface to provide antimicrobial properties which is important, because varying the capping ligands allows for creation of

large libraries of candidates for screening; in order to find a particle surface composition with highest gastrointestinal tract absorptivity and efficacy.

In the current literature, there are two main approaches to creating antimicrobial gold nanoparticles. One method conjugates antimicrobial small molecules to gold nanoparticles to improve their efficacy and potentially create a more potent antibiotic. The gold nanoparticles can improve efficacy of these small molecule drugs by providing a platform to improve solubility and bioactivity, like the curcumin gold nanoparticle conjugate.⁴³ Conjugation of curcumin, a hydrophobic molecule, to gold nanoparticles with a stabilizing ligand, increased its solubility in aqueous solutions to 1.4 mM.⁴³ Increasing solubility had a downstream effect of improving its ability inhibit growth of gram-negative *E. coli* ATCC 25922.⁴³ Another way gold nanoparticles can improve efficacy is by protecting the small molecule drug from enzymatic inactivation. For example, preliminary studies showed that conjugating penicillin, a beta-lactam containing antibiotic, to a 2.0 nm gold nanoparticle enabled the drug to inhibit bacterial growth of MRSA; previously, penicillin could only inhibit growth of the drug sensitive strain MSSA.⁴⁴ MRSA contains enzymes called beta-lactamases, which cleave the drug's the beta-lactam ring and renders it ineffective to treat the bacterial infection.⁴⁵ The other method, pioneered by the Feldheim lab, utilizes a combinatorial library of short chain thiols that lack intrinsic antimicrobial properties when free in solution, but show antimicrobial properties when conjugated to gold nanoparticles in specific ratios.⁴⁶

In work on bacterial disease, the Feldheim lab has developed a new gold nanoparticle drug discovery method that utilizes a concept called Small Molecule

Variable Ligand Display.⁴⁷ In this platform, small thiolated molecules that vary in terms of length and charge are conjugated to the surface of 2.0 nm gold nanoparticles. Amazingly, these small molecules do not have antimicrobial properties free in solution but can be potent bacterial growth inhibitors or even bactericidal in culture when conjugated to the gold surface in specific ratios.^{47,46} Another surprising property of these antimicrobials is that by tuning the surface composition the particle can then become active against different species of bacteria.⁴⁷ Currently the SMVLD gold nanoparticle platform has been used to isolate antimicrobials to *S. Aureus*, *K. pneumoniae*, *E. coli*, and *M. smegmatis*. *Mycobacterium smegmatis* is considered a non-pathogenic relative of Mtb and is often utilized as a surrogate when research on Mtb is prohibitive due to its biosafety level.^{47,48,49} The Feldheim gold nanoparticle antimicrobial to *M. smegmatis* has been undergoing testing to determine its efficacy against *Mtb* itself.⁴⁹ In addition, all of these gold nanoparticles have been tested in vitro to determine their toxicity to mammalian cells. In the chapter 5, an example of a gold nanoparticle antimicrobial will be further described and work shown for the effort to determine the drug's bioavailability, toxicity, and improvement thereof *in vivo*.

The promise of gold antimicrobials makes it important to investigate their use by oral administration for resource limited regions. Chapter 4 describes work aimed at creating a gold nanoparticle platform with tunable oral bioavailability.

1.7 Conclusion

Tuberculosis is not just a re-emerging infectious disease, but a persistent scourge that world health leaders are working to completely eradicate from the

human population. TB most stubbornly has been spreading in resource limited regions. People in these regions need diagnostics and therapeutics tailored to their available resources. Developing countries would best benefit from a diagnostic that is robust, gives quick results, and requires minimal electricity or materials. Likewise, a high impact therapeutic for these communities would promote patient compliance through oral administration and low toxicity, and utilize minimal energy for storage. In the following dissertation, these challenges are confronted by development of an orally bioavailable gold nanoparticle platform, a SERS assay for the detection of a TB biomarker in urine, and isolating modified-aptamers for the detection of *Mtb* biomarkers in urine.

Chapter 2: Surface Enhanced Raman Spectroscopy (SERS) Immunoassay for the Detection of Mannose Capped Lipoarabinomannan

2.1 Introduction

There is an urgent need for a TB diagnostic that correctly identifies TB cases. To address this need a surface enhanced Raman spectroscopy (SERS) immunoassay has been developed that pulls a TB biomarker out of urine with polyclonal antibody and then uses SERS as the readout method. The project has two main components: adaptation of the assay to a urine matrix and test clinical samples to determine efficacy. The first project component required incorporation of a sample pretreatment procedure and optimization of signal. The second component determined the SERS assay's clinical sensitivity and specificity against blinded clinical samples from the Foundation for Innovative New Diagnostics (FIND). After testing, the results were unblinded and compared to the known *Mtb* sputum bacteria culture results. Current urine-based ManLAM assays have sensitivities of 60-70% for HIV co-infected samples and results are as low as 4% for patients without HIV co-infections.^{50,35} Patients with HIV co-infection present with higher LAM urine levels, because they lack strong immune systems to keep bacterial burdens low.³⁵ FIND clinical sample results indicate the SERS assay has a clinical sensitivity of 85% and specificity of 75% for patients with HIV co-infection, and clinical sensitivity of 63% and specificity of 70% for patients without HIV co-infection. The SERS assay results are promising when compared to current urine-based ManLAM immunoassays.

2.1.1 SERS immunoassay

Recent research has shown the promise of achieving low limits of detection, high versatility, and portability with SERS immunoassays.⁵¹⁻⁶¹ As part of research in the area, the Porter group has been developing serum-based SERS assays for the detection of cancer biomarkers at picogram per milliliter levels.^{56,61} The SERS assays have also been designed to be chip-based and have great potential for development into lateral flow tests.^{58,62} Lateral flow assays are portable and minimize exposure to pathogens. Multiplex testing for multiple biomarkers is another possibility for the SERS assay, as shown by proof of concept tests for cancer biomarkers.⁶¹ The flexibility of the SERS immunoassay to have high sensitivity, ability to detect multiple biomarkers, and portability makes the method an excellent candidate for a TB diagnostic in resource limited regions.

This chip-based SERS assay is designed to capture the TB biomarker ManLAM from urine after a pretreatment step, explained later, with an anti-LAM antibody. The overall assay scheme is shown in figure 2.1 below. ManLAM is captured by antibody that is absorbed to monolayer of Dithiobis[succinimidyl propionate] (DSP) on the gold surface.⁶³ Next an extrinsic Raman label (ERL) is brought in to bind the ManLAM for quantification.⁶⁴ The ERL is comprised of a 60 nm gold nanoparticle with both Raman reporter molecules and anti-LAM antibodies adsorbed to it. The 60 nm gold nanoparticle confers signal enhancement of the Raman reporter adlayer on its surface. The antibody should be covalently bound to the gold nanoparticle via an amide linkage on the aromatic ring of the reporter molecule, but more often hydrolysis of the NHS ester occurs before covalent crosslinking can occur.⁵¹

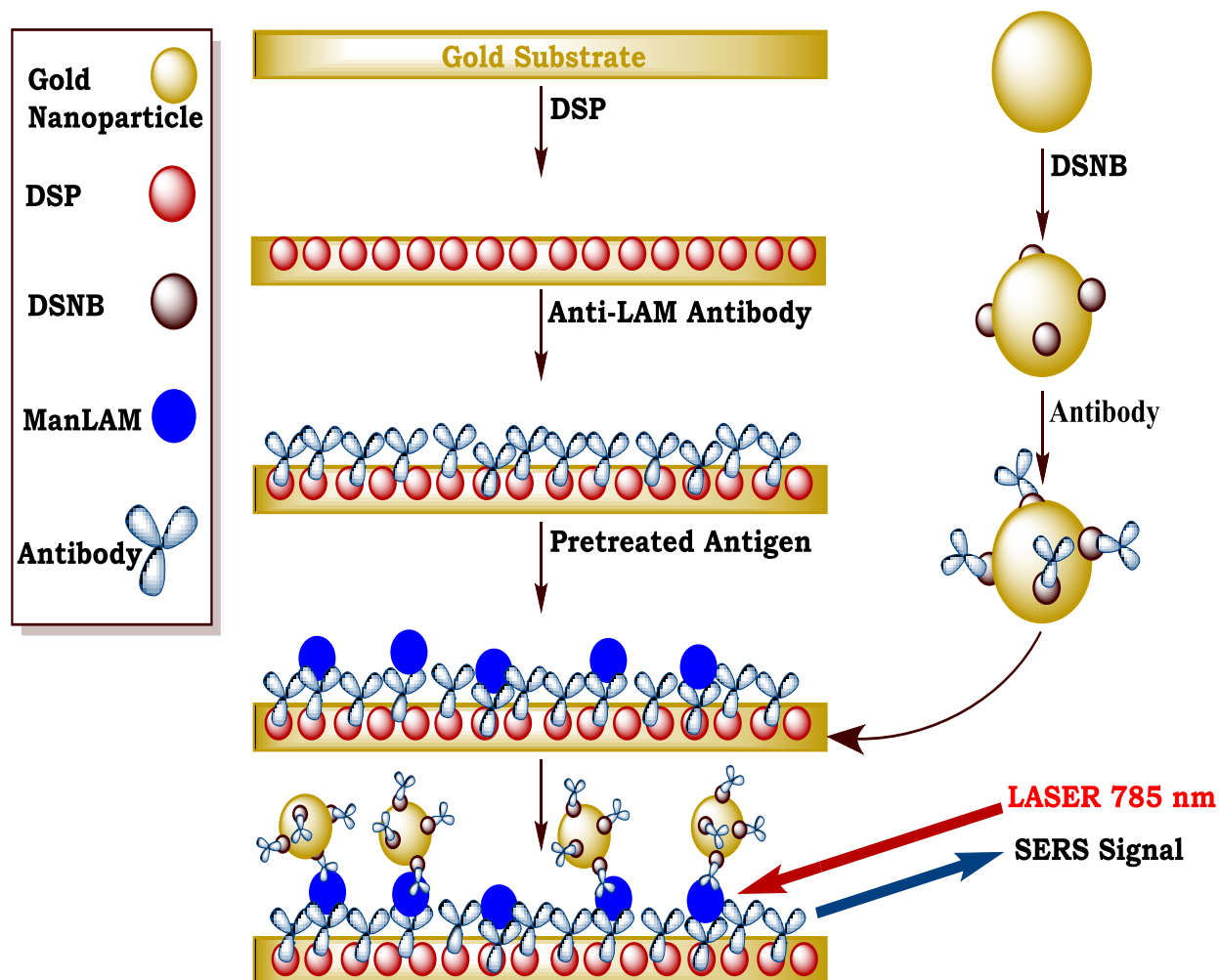


Figure 2.1: SERS assay scheme for the detection of ManLAM in urine.

The ERL allows for not only quantification of the ManLAM, but also confers selectivity for it too. The signal is created when a LASER at 785 nm excites the local surface plasmon on the gold nanoparticle, which in turn enhances the Raman scattering signal from the DSNB molecule, shown in figure 2.2. The Raman shift measured in this assay is at 1336 cm^{-1} and it is created from symmetric stretching of the nitro group on DSNB. The signal is measured by a spectrograph and CCD array detector.

2.1.2 ManLAM as Biomarker in Urine

ManLAM is a biomarker excreted in urine of individuals with active TB. The glycolipid called ManLAM is a highly expressed cell wall component of *Mtb* and one of the most thoroughly characterized TB biomarkers.⁶⁵ ManLAM comprises 15% of a *Mtb* cell by dry weight.⁶⁶ It is an approximately 17.4 kDa molecule composed mannose and arabinose chains with a fatty acid tail, full structure shown in Figure 2.3.^{67–69} When an *Mtb* cell decomposes the ManLAM is shed and released into host. ManLAM has been found in many different fluid samples of *Mtb* infected individuals; such as serum, urine, and sputum.^{14,35,36} A urine-based assay would advantageous, because it could be safe for benchtop work.⁷⁰ In addition, urine samples can be collected in volumes greater than 10 mL and concentrated if necessary to improve detection. The ManLAM present in urine from active mycobacterial infection makes it an excellent candidate for a TB diagnostic.

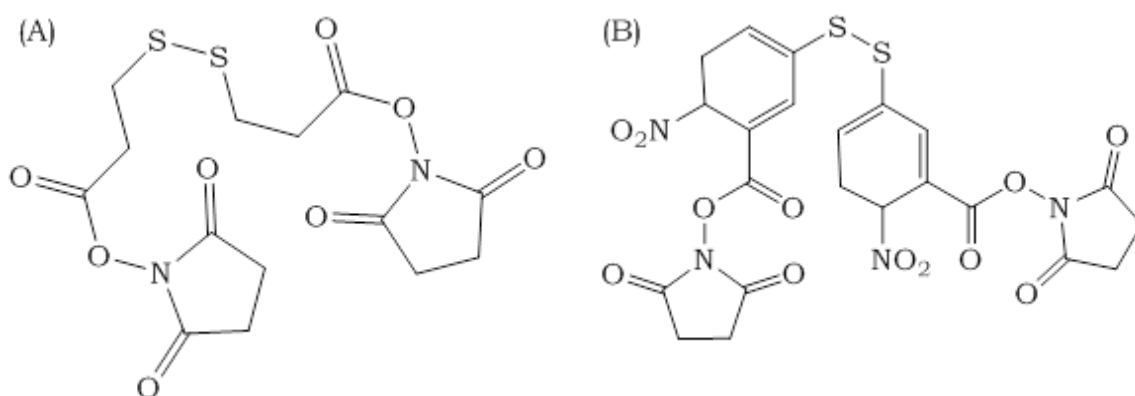


Figure 2.2: (A) Dithiobis[succinimidyl propionate] molecule used to adsorb the antibody to the gold platform. (B) 5,5'-dithiobis(succinimidyl-2-nitrobenzoic acid) (DSNB) molecule that is chemisorbed to the gold nanoparticle surface and binds antibody after a reaction with the molecule's NHS ester moiety.

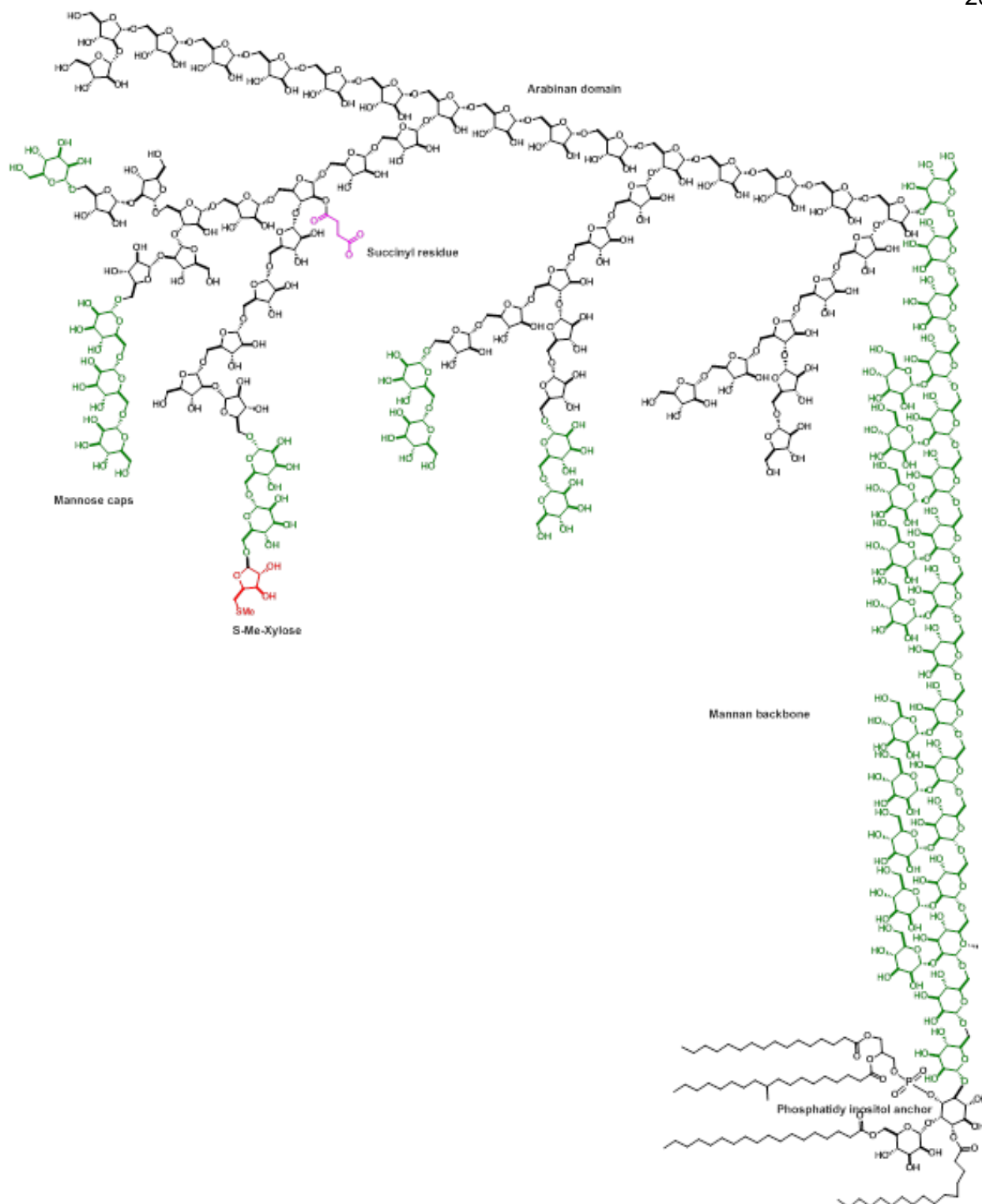
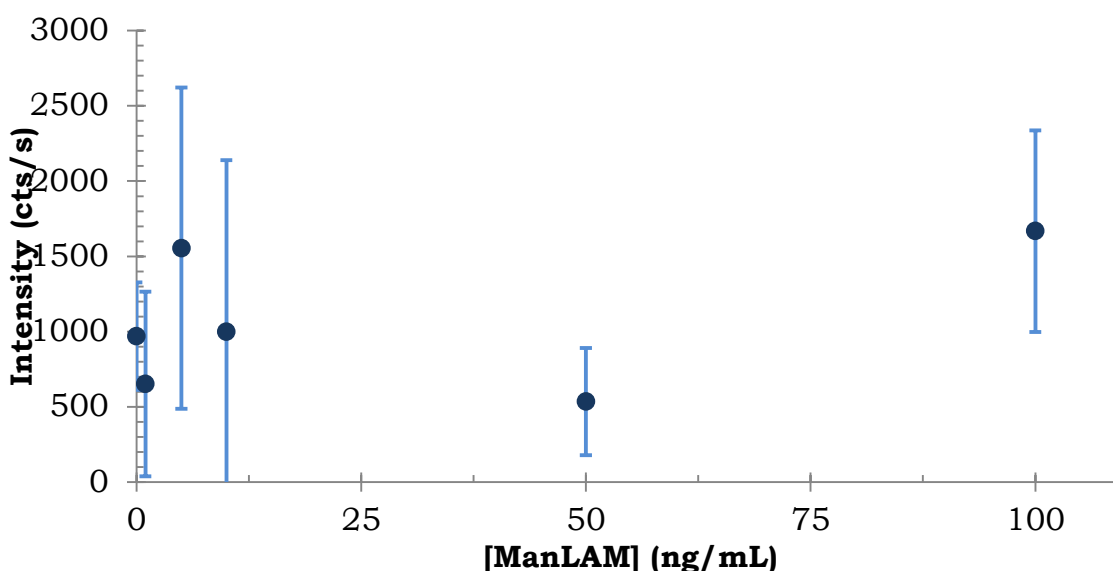


Figure 2.3. A representation of ManLAM and all of its components from the mannose caps to its fatty acid tails. This image has been reproduced with permission of De Prithwiraj from the Chatterjee Lab at Colorado State University.

2.2 Results and Discussion

2.2.1 Assay Optimization

The SERS immunoassay for this project has been adapted from serum-based protocols.^{56,61,63,64} Preliminary results for the urine-based SERS assay were marginally successful without a urine pretreatment protocol. The SERS assay dose-response curve in untreated urine (see figure 2.4), had signal intermittently



2.4 SERS immunoassay dose-response curve using non-endemic urine spiked with ManLAM without sample pretreatment.

above background, and failed to respond in a linear fashion with increasing antigen levels. The lack of dose-response could be due to matrix effects from urinary proteins. Data unpublished from our collaborators indicate that ManLAM forms a complex with urinary proteins, which interferes with it binding to the LAM antibody. It was deemed necessary to incorporate a pretreatment step to free ManLAM from the complex and improve signal.

The first approach was to use proteinase K to degrade proteins present in the urine to release ManLAM from a protein complex. Proteinase K is a commonly used protease, which degrades proteins by cleaving amide bonds after aliphatic

and aromatic amino acids.⁷¹ A titration was performed to determine the minimum protease concentration and incubation time necessary to significantly degrade urinary proteins, data shown in appendix A1. The minimum concentration was determined to be 0.1 mg/mL with 30 minute incubation. During the assay, after proteinase K treatment, the protease had to be inhibited before it degraded antibodies in the later steps, to do so a protease inhibitor, proteinase K, was added at a molar ratio of 10:1 inhibitor to protease for effective inhibition.⁷² The proteinase K assay was imperceptibly better (see appendix A2). The signal was higher, but the standard deviations were also tremendously larger. In conclusion, the increase in standard deviation suggests the presence of additional protein may be the source of erratic signal.

The erratic nature of the signal of previous assays suggested that there was something in the urine matrix, possibly protein, contributing to non-specific signal. Two methods could reduce non-specific binding; either change stringency of the washes or employ a pretreatment step to remove urine proteins. The serum protocols utilize a harsh acid pretreatment to precipitate protein that interferes with signal. Initially, this step seemed unnecessary for urine, because the protein content of urine is 0-0.07% (w/v) whereas serum composition is approximately 10% (6.4-8.3 g/dL) protein.^{73,74} If protein contributed to non-specific binding, then the acid-based precipitation would improve the assay. The acid pretreatment is capable of defatting proteins in urine that bind fatty acids.^{61,75,76} If the urinary protein binds ManLAM fatty acids acid tails, then the acid pretreatment could break apart the complex. Alternatively, the acid pretreatment could precipitate ManLAM bound to protein. The acid pretreatment improved the signal, but the

standard deviations were still large, see calibration curve in appendix A3. The proteinase K was incorporated into the assay before the acid precipitation step, as shown in figure 2.5. Additionally, when proteinase K precedes the acid treatment, the standard deviations are minimized further, which is evident when comparing appendix A3 to A5. Additional tests were completed to determine if varying the proteinase K concentration from 0-2.0mg/mL could further enhance signal (see appendix A4). Increasing the concentration of proteinase K fails to dramatically increase signal; however a comparison of the dose-response curves indicate the coefficient of variation (CV) decrease from 40% to 10% with increasing amounts of

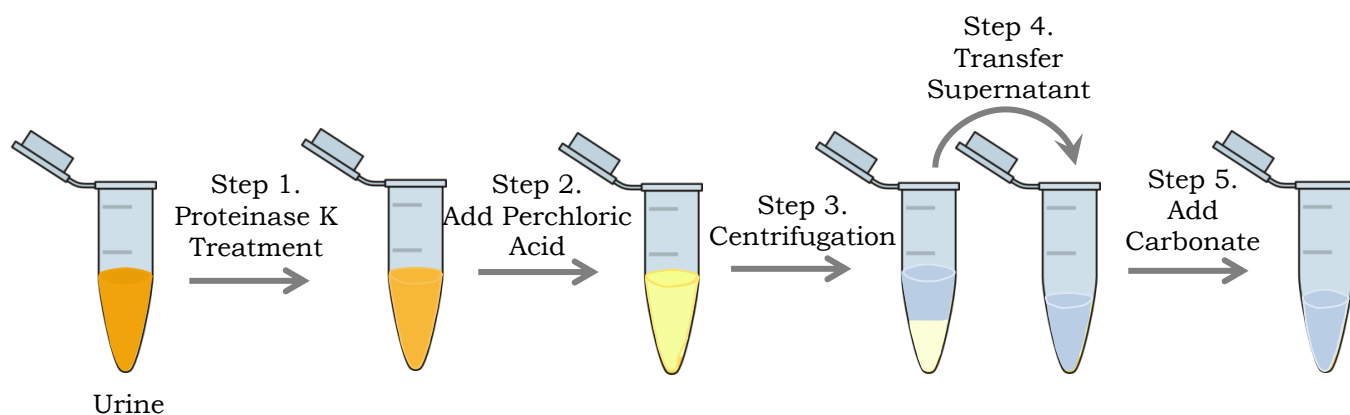


Figure 2.5 The optimized pretreatment scheme for urine samples used in the SERS assay.

protease. This means use of 2.0 mg/mL proteinase K produces results with the least variability relative to the mean of data.

To improve signal to noise the percentage of Tween-20 in the wash buffer was altered in order to significantly enhance the stringency of a wash steps. Tween-20, a non-ionic polysorbate composed of a fatty acid ester moiety and polyoxyethylene chain. It is considered a gentle surfactant that is commonly used in assays, because it promotes solubility. Three commonly used concentrations of tween-20 were tested in wash steps of the assay to determine a concentration with best signal to noise. Figure 2.6 displays three calibration curves with 0.01%, 0.05%, or 0.1% tween-20 used in the buffered washes of the SERS assay. The assay incorporating 0.1% tween-20 washes had the lowest CV of 13%; although, the assay with 0.01% tween-20 washes attained a higher CV of 21% it had the best analytical sensitivity.

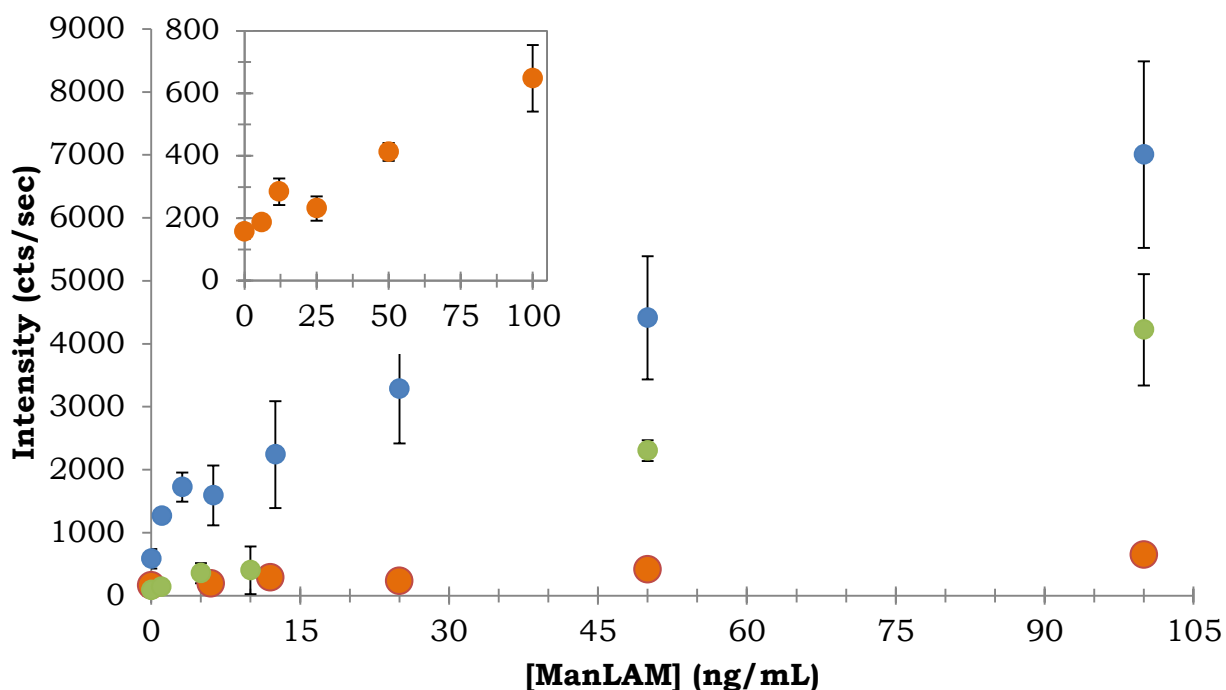


Figure 2.6 Calibration of the the SERS assay utilizing 0.1% tween-20 (orange), 0.05% (green), or 0.01% tween-20 (blue) circles.

2.2.2 Optimized Calibration Curve of ManLAM Standards

The optimized calibration curve used 2.0 mg/mL proteinase K in the pretreatment, the acid treatment, and 0.01% tween-20 in the buffered washes. Other details regarding the assay can be found in the experimental methods. To make a calibration curve, each concentration had 3 replicates. The Raman shift of interest at 1336 cm^{-1} occurs from the symmetric stretch of the aromatic nitro group of DSNB, shown in figure 2.2. The raw SERS spectra are shown in figure 2.7. The intensity data per concentration at 1336 cm^{-1} were averaged and used to make the dose response curve, see figure 2.8.

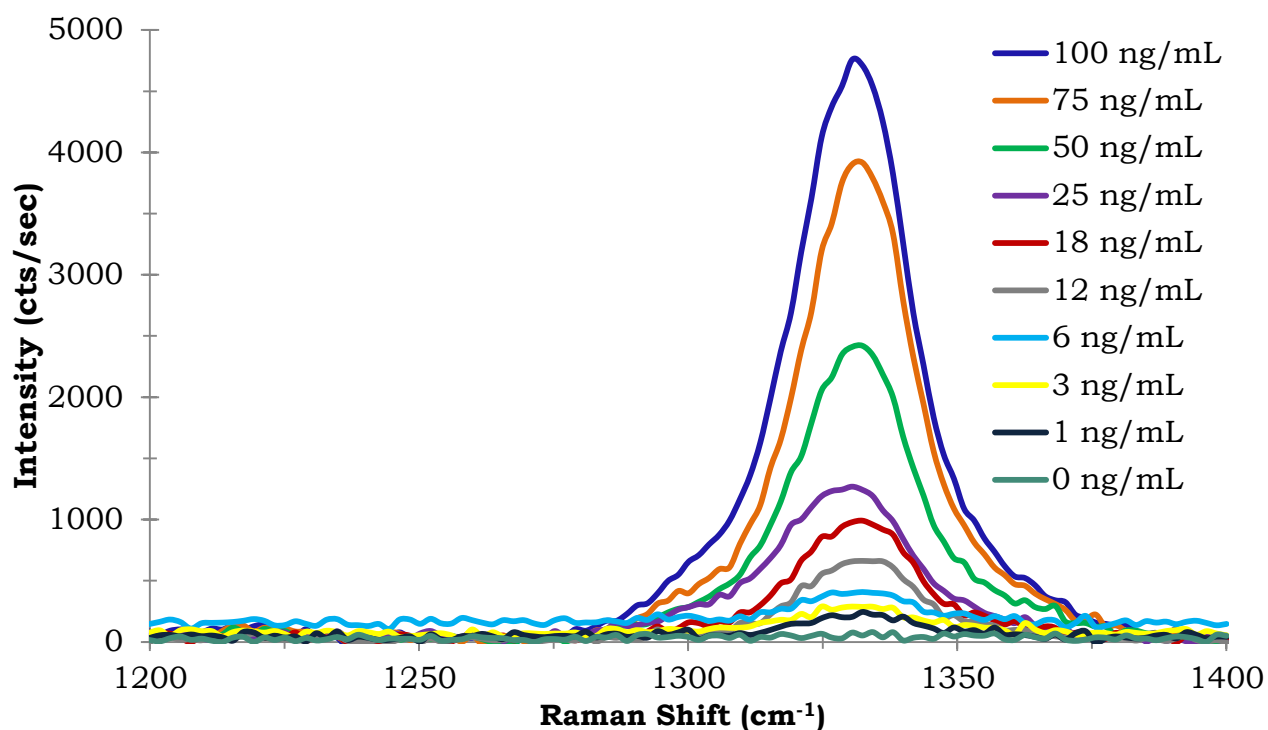


Figure 2.7. SERS immunoassay for urine spiked with ManLAM.

Each point on the curve represents the average of three readings taken per replicate. The resulting dose response curve for each concentration was plotted versus the SERS intensity. The standards range from 0 ng/mL to 100 ng/mL ManLAM. The theoretical limit of detection (LOD) was calculated based off of the

signal intensity of the blank sample plus three times the standard deviation. The average LOD for the optimized SERS immunoassay varied from 5-10 ng/mL. The limit of quantification (LOQ) for the assay is considered to be 10x the LOD, which would be approximately 50-100 ng/mL.

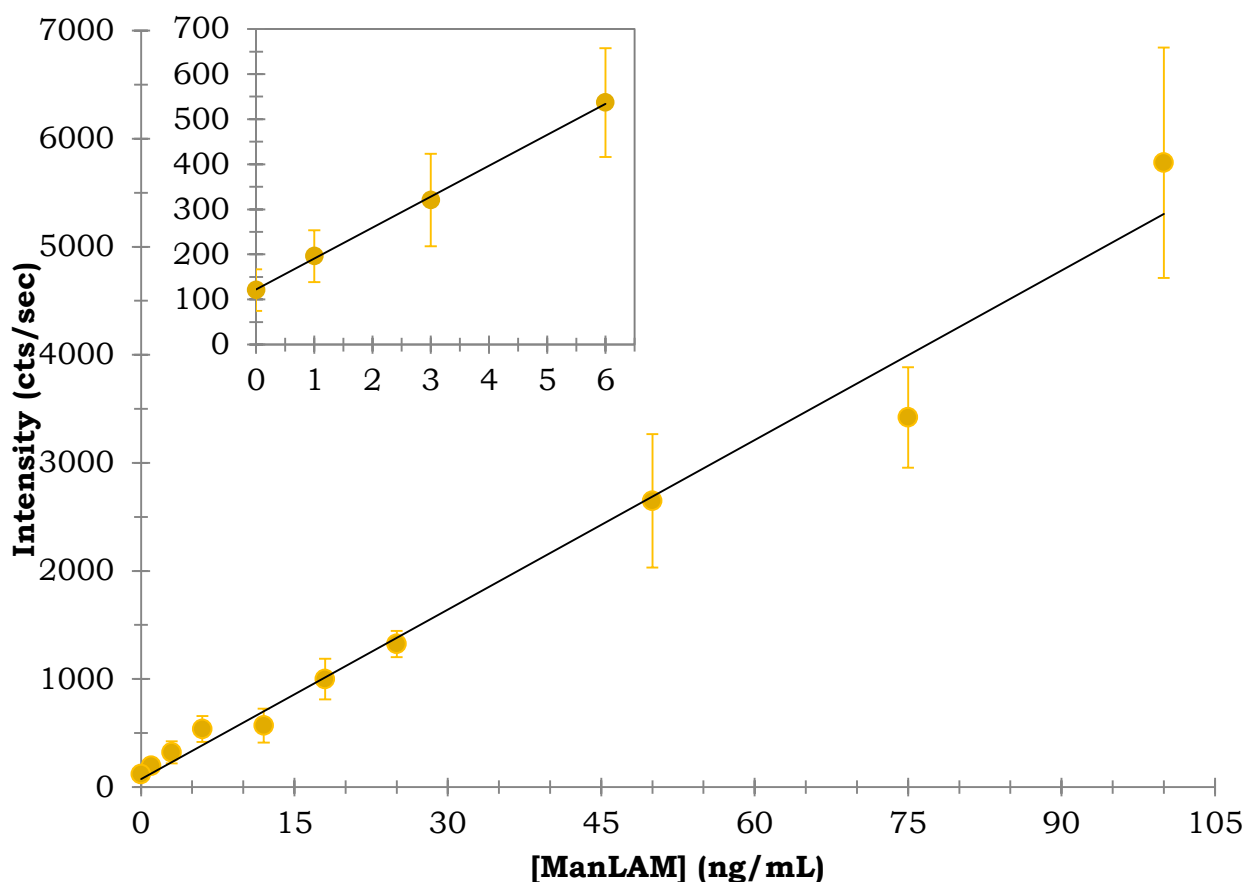


Figure 2.8. Dose-response ($\nu_s(\text{NO}_2)$ at 1336 cm^{-1}) curves for the detection of ManLAM spiked into non-endemic urine.

2.2.3 Comparison of SERS versus Culture Results for Patient Samples

After SERS assay optimization, blinded clinical samples were tested and determined to be ManLAM positive or negative. Presence of ManLAM was based off of the LOD of calibration curves assayed concurrently with clinical sample sets. The results were then unblinded, compared to FIND sputum *Mtb* cell culture results, and listed in table 2.1. During testing it was discovered that some of the

Table 2.1 SERS Detection of ManLAM in Endemic FIND samples

	Patients Correctly Identified (Percentage)
Sensitivity	31/45 (68.9%)
Specificity	11/13 (84.6%)*
	25/35 (71.4%)
	9/12 (75%)*

* Represents a subset of samples in which HIV co-infection was present. culture negative samples tested positive for LAM in three separate methods SERS assay, GC-MS, and a modified ALERE assay (GC-MS and ALERE data unpublished from CSU collaborator). The possibility exists that these patients may had a urogenital (extrapulmonary) form of TB, and if this is true then 8 of the samples

Table 2.2 SERS Detection of ManLAM in Endemic FIND Samples (corrected for possible extrapulmonary TB cases)

	Patients Correctly Identified (Percentage)
Sensitivity	39/53 (73.6%)
Specificity	13/15 (86.7%)*
	25/27 (92.6%)
	9/10 (90%)*

* Represents a subset of samples in which HIV co-infection was present.

were not false positives. Table 2.2 takes into account the possible extrapulmonary TB cases and shows their impact on SERS clinical sensitivity and specificity. Based on the data from table 2.1, the SERS assay performed better on TB positive samples with HIV co-infection. Also, the SERS assay had better sensitivity than the current Alere TB LAM diagnostic. The clinical samples results show that the SERS immunoassay could hold promise as a TB diagnostic.

2.3 Conclusion

In this project a SERS immunoassay for the detection ManLAM has been adapted to urine, and its efficacy as a detection method has been investigated by FIND clinical samples. The assay was able to positively detect presence of ManLAM in 69% of TB infected individuals. Although the results are better than the status quo, the assay could benefit from further improvements. Such as, Normalization of urine salt concentrations and pH of to improve binding conditions for the antibody. Substitution of antibodies with DNA aptamers could improve the selectivity for TB ManLAM. Development of possible aptamer affinity reagents are shown in chapter 3. Conversion of the SERS ManLAM assay into a multiplex format could improve selectivity for type of *Mtb* strain. The SERS_{sk} assay to detect ManLAM has been developed and further tweaks to the assay could make it a viable TB diagnostic.

2.4 Experimental Methods

2.4.1 Reagents

Gold nanoparticles (60 nm 2.6×10^{10} particles per milliliter) were purchased from TED Pella. Dithiobis(succinimidyl propionate) (DSP), bovine serum albumin (BSA) fatty acid free, Tween-20, and NaCl were from Sigma Aldrich. Phosphate

buffered saline (10 mM phosphate, 150 mM NaCl; pH 7.4) and borate buffer packs (50 mM borate; pH 8.5) were acquired from Thermoscientific Pierce. 5,5'-dithiobis(succinimidyl-2-nitrobenzoate) (DSNB) was synthesized by the Porter Lab at the University of Utah. The antibody used for in the assay comes from a Monoclonal Anti-*Mycobacterium leprae* LAM, Clone 906.7 (produced in vitro). The same antibody was employed to coat the capture substrate and ERLS, along with ManLAM from the CDC 1551 strain of *Mtb* (17.4 kDa) as the antigen; non-endemic urine; these reagents were obtained from the Chatterjee Lab at Colorado State University. Blinded patient urine samples, designated as a letter and number were collected from endemic populations that were TB suspects by the Foundation for Innovative Diagnostics. Glass slides with 24 gold addresses per slide were manufactured by a collaborator at the University of Utah. The 96-well microplate array was obtained from Arrayit Corporation.

2.4.2. Preparation of ERLs

The pH was adjusted for each 1.0 mL aliquot of 60 nm gold to pH 8.5 by the addition of 40 μ L of 50 mM borate buffer pH 8.5 and then the surface functionalized by the addition of 13.6 μ L of 1.0 mM DSNB in acetonitrile, and incubated for 1.5 hours. ERLs were further functionalized by adding 13.7 μ L of 5.0 μ g/mL of the antibody and allowed to incubate another 1 hour. To stabilize the ERLs, 100 μ L of 10% BSA in 2 mM borate buffer was added to each aliquot and incubated another 1 hour. Finally, the aliquot was centrifuged at 2000 \times g for 10 min. Only the pellet is retained, the ERL pellet was resuspended in 1.0 mL of 2

mM borate buffer containing 1% BSA. This procedure was repeated twice and then the suspension was modified with 1 milliliter of 150mM NaCl and 1% BSA.

2.4.3 Capture substrate preparation

The arrays were made by the Porter Lab at the University of Utah. To carry out assays, 1×3 inch glass slides were used as the base platform. These slides were ultrasonically bathed in 10% Contrad 70 solution (Micro, Cole Parmer), deionized water, and ethanol, sequentially for 30 min. The slides were then restively coated with chromium (~15 nm) and ~300 nm of gold (99.999% purity) at a rate of 0.1 nm/s. Prior to use, these substrates were cleaned in a 270 mTorr argon plasma (Harrick) at medium power for 15 min. The following steps were used to form the addressed array. First, a Parafilm mask with a 3×8 array of 3 mm holes was thermally sealed to the gold-coated glass slide for 1 min at 70 °C. This created an array of exposed gold “wells,” each serving as an individual capture address.

Further preparation was completed by the Feldheim lab. This assembly was then immersed in a solution of 10 mM DSP in 100% ethanol for 1.0 h, rinsed with ethanol and dried under a stream of nitrogen. Anti-ManLAM (13.7 μ L, 100 μ g/mL), diluted in 1x phosphate buffered saline (pH 7.4), was applied to the eight sample areas in rows 1-3 and allowed to incubate for an hour. In this step the antibody capture layer is formed by either coupling with the succinimidyl ester of the DSP derived monolayer with exposed lysine, or electrostatic interactions. The antibody solution was then removed from each well by a micropipette and followed by three washes with 150 μ L of 1x PBS with either 0.01% or 0.1% tween-20,

depending on the assay. Next, 100 μL of a Startingblock blocking buffer was added per well and incubated for an hour. Afterwards, the sample areas were washed 3 times with 150 μL of 1x PBS and reverse pipetting 5 times each. Once the capture layer was prepared, each well was exposed to 100 μL aliquots of ManLAM spiked urine in triplicate (0-100 ng/mL ManLAM, plate 1) or any remaining plates were either clinical samples or other test assays. The samples were incubated for 1.0 hour at room temperature on a belly dancer mixer. After the 1 hour incubation, each sample area was washed 3x with 1x PBS containing tween-20. The captured ManLAM was then exposed to a 100 μL ERL solution overnight at room temperature in a humidity chamber. The next day the plates were washed 3 times with 150 μL of 2 mM Borate Buffer, 10 mM NaCl, and Tween 20 and allowed to air dry in a dark drawer before measuring the SERS intensity.

2.4.4 Preparation of Calibration Standards

ManLAM was diluted with urine to produce a stock solution of 1000.0 ng/mL, from a stock solution of 1.0 mg/mL in water. This solution was then used to prepare standards for the calibration curve by further diluting in urine in a range of 0 ng/mL through 100 ng/mL at a maximum volume of 400 μL .

2.4.5 Preparation of Urine Samples

The urine samples were thawed to room temperature on ice. A 400 μL aliquot of each sample is transferred to a centrifuge tube, and then 2.00 μL of proteinase K (stock 20 mg/mL, ThermoFisher Scientific Cat #AM2548) was also added to the tube. Incubation was allowed to proceed for 1.0 hour at room temperature. Next, 16 μL of 70% perchloric acid (double distilled, Sigma Aldrich

cat #A2296-1LB) is added to the tube, the tube is vortexed 10 seconds, and then centrifuged at 12,000 x RCF for 5 minutes. After centrifugation, 350 μL of the supernatant is transferred to another tube containing 48.0 μL of 2.0 M K_2CO_3 (Stock 25 grams, Sigma Aldrich cat #590681). The neutralized sample is allowed to rest at room temperature for another hour before further testing.

2.4.6 Instrumentation

The Raman spectra were collected with a portable iRaman Plus fiber optic Raman probe from B&W Tek. The light source was a 350 mW, 785-nm diode laser. The spectrograph was BWS465-785S spectrometer (4.5 cm^{-1} resolution @ 912 nm) and a high quantum efficiency CCD array. The incident laser light was focused to a 5- μm spot size on the substrate at normal incidence; the power at the sample was 10% or ~37 mW. Each spectrum was acquired with a 30 second integration time. For each address a spectra was measured three times, and measurements for all the replicates were averaged. For the clinical samples, the signal was recorded and sent to a collaborator to be unblinded and compared to FIND results regarding the samples.

Chapter 3: Modified-Oligonucleotide Affinity Reagents for the Detection of Mycobacterium Tuberculosis Biomarkers in Urine

3.1 Introduction

Aptamers are an excellent alternative to antibodies for capture reagents in biomolecule detection assays. Antibodies suffer from non-specific binding to molecules in the urine matrix, whereas aptamers can be selected for in a manner that minimizes non-specific binding.⁷⁷ The selection conditions for aptamers can be performed in the sample matrix, unlike antibodies which must be isolated from animal tissue.⁷⁸ Isolating an aptamer in the sample matrix helps remove those prone to non-specific binding.^{79–81} Additional benefits of aptamers are their low cost and speed of synthesis, and they are easily functionalized in order to be anchored to a substrate or as a signal source.^{79,80} Aptamers could potentially be substituted for antibodies in diagnostics in order to achieve more accurate results.

This project used *in vitro* selection to isolate modified DNA aptamers to TB biomarkers in urine, and later investigated their promise for use in a TB biomarker detection assay. Oligonucleotide affinity reagents, a.k.a aptamers, are isolated by the *in vitro* selection technique called systematic evolution of ligands exponential enrichment (SELEX). SELEX can be combined with chemical modification of the nucleic acid monomers to expand molecular diversity, which could increase points of contact and improve binding affinity. This project isolated modified DNA aptamers to possible *Mtb* biomarkers in urine: 3 proteins with gene designations MT1721, MT3444, MT2462, and ManLAM. Representative aptamers from distinct conserved families were tested to verify binding to their respective targets. Equilibrium dissociation constants for the interaction of aptamers isolated with their specific target ranged from 9 to 80 nM. Additionally, preliminary tests

determined experimental conditions that could help tailor an assay to the aptamers.

3.2 TB biomarkers

Direct detection of *Mtb* components makes it clear that the bacteria currently infect the host, and possibly the bacterial burden of the patient. *Mtb* biomarkers have been found in several types of fluid samples; such as sputum, serum, cerebral spinal fluid, and urine.⁵⁰ The current gold standard for TB diagnostics, the sputum smear test, directly detects whole cell *Mycobacterium* in sputum, but it is not specific to only *Mtb*. Additionally, some patients cannot provide sputum samples.¹³ TB diagnostics could be further improved upon if the gold standard diagnostic for resource limited regions directly detected *Mtb* biomarkers in a fluid sample all patients could provide for testing.

Creating affinity reagents for *Mtb* biomarkers in urine is advantageous. Urine is a less complex sample matrix than other fluid samples such as serum or sputum, because urine is processed by organs that filter out most proteins leaving a sample of only 5% solute.^{13,82} Universally any patient can provide a urine sample and in large volumes, up to 100-200 mL, that can be concentrated if necessary.⁷³ Concentrating the sample can help improve LOD of the assay. The only hindrance to using urine for TB diagnostics has been that until recently, ManLAM, the only validated TB biomarker in urine, could not be detected reliably. The results from the SERS immunoassay from Chapter 2 demonstrates that ManLAM assays in urine can be improved further by DNA aptamer affinity reagents.

Campos-Neto published the discovery of 4 new potential protein TB biomarkers found in urine of patients with active pulmonary TB: MoaA-related protein (MT 1721), Ornithine Carbamoyltransferase (MT 1694), Homoserine O-acetyltransferase (MT 3444), and Phosphoadenosine Phosphosulphate Reductase (MT 2462). These proteins could be ideal candidates because their gene sequences had high sequence homology to only other strains of TB and select mycobacteria. Additionally, Campos-Neto found that the recombinant versions of these proteins were recognized by IgG antibodies found in patients with active pulmonary TB, but not patients without an *Mtb* infection. The TB proteins found in urine by Campos-neto were targets for modified-oligonucleotide selections completed in this assay.

3.3 SELEX with Modified-Nucleotides

Choice of modified nucleotide is vital to a successful selection for biomolecules. Modification of the nucleotide can improve an aptamer by adding nuclease resistance, binding contacts, and covalent activity.⁸³ Historically, aptamers with natural nucleotides interact with a target via shape complementarity, hydrogen bonding, polar contacts, and ion-pairing.⁸³ For this project, both the naphthyl and tryptl-amino modification were used to exploit binding contacts on the TB protein biomarkers; alternatively, the pyridyl modification was utilized in the ManLAM selections because pyridine has been shown to bind to hydroxyl groups on monosaccharides.⁸⁴ These modifications should assist in finding high affinity aptamers to their respective targets. Figure 3.1 displays a modified DNA nucleotide and the specific modifications used in this project.

SELEX with modified nucleotides begins with a large combinatorial library of sequences, up to 10^{14} per 1 nmol of library. The creation of a modified aptamer library starts with a template library consisting of only natural nucleotides. The template sequence is flanked by two fixed regions at its 5' and 3' ends for the purpose of amplification by polymerase chain reaction (PCR) and primer extension. Between the constant regions is a 40 nucleotide random region. The random region is synthesized to have 25% of each nucleotide to create an unbiased initial pool. Equal distribution of nucleotide composition in the initial template ensures that enrichment of any nucleotide seen in sequencing is solely due to evolution in the pool of sequences. During the final step in the library synthesis a copy of the template is created in a

process called primer extension. The primer extension step requires a special polymerase to incorporate modified nucleotides wherever there is an adenosine in the template. This polymerase must lack 3'→5' proof-reading ability. A high fidelity polymerase would excise out modified

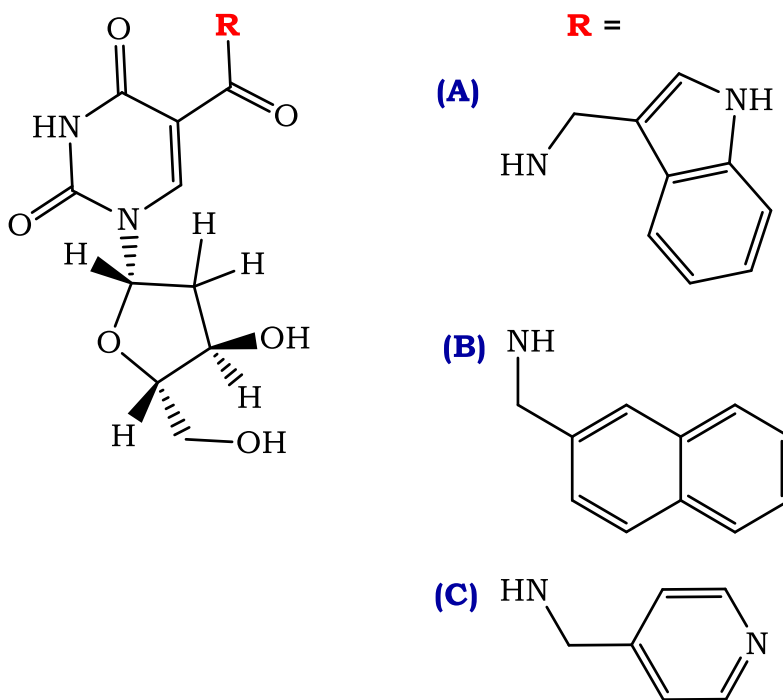


Figure 3.1 A molecular representation of a modified thymidine nucleotide incorporated into aptamers in this project. R indicates the modifications: (A) tryptyl amino, (B) Naphthyl, and (C) 4-pyridyl.

nucleotides, which it perceives as a contaminant. The library is ready for SELEX.

The library is then put through multiple rounds, which add pressure to the sequence pool. The pressure narrows the aptamer pool diversity through the removal of sequences with non-specific or low affinity to the target. Figure 3.2 illustrates a selection scheme for use with magnetic beads as a partitioning platform. Once the modified-oligonucleotide pool has been sufficiently narrowed, then the evolved pool is cloned and sequenced. From this point individual sequences can be tested to determine their selectivity for the target and binding capacity.

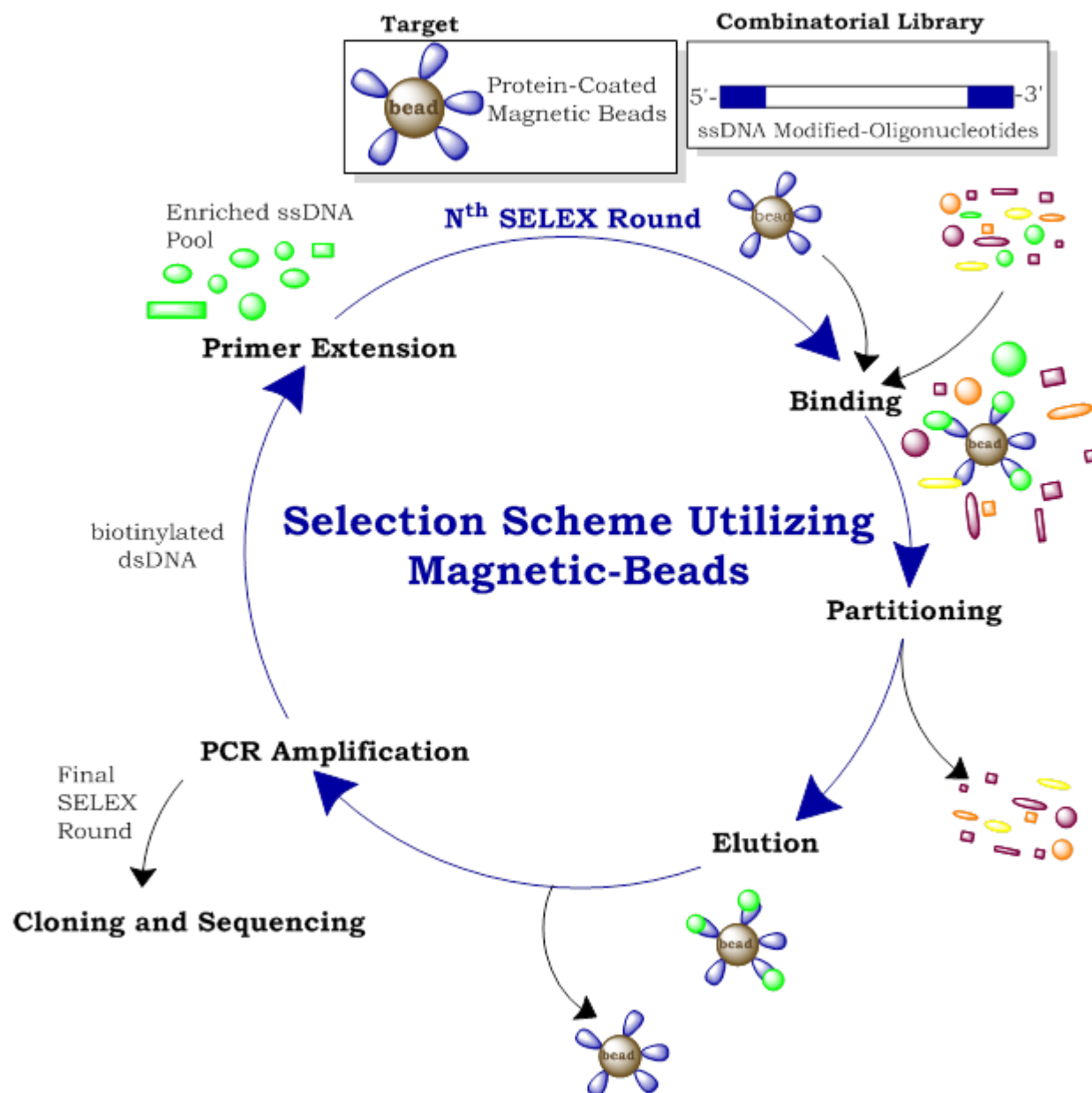


Figure 3.2 A SELEX for a target functionalized to bind a magnetic bead.

3.4 Results and Discussion

The following details the steps required to isolate and characterize modified-DNA aptamers to TB biomarkers in urine. Three of the targets were proteins identified by the research of Campos-Neto, and the other the glycolipid cell wall

component described in chapter 2. Aptamers were isolated for each of the targets and evaluated for their capability to be used in a TB diagnostic, like the SERS assay mentioned in chapter 2.

3.4.1 Target Preparation

3.4.1.1 Protein Biomarkers

The protein biomarkers were expressed recombinantly in *E.coli*. Recombinant proteins are created by cloning a plasmid that codes for the protein into host bacteria, and amplified by exploiting bacterial protein synthesis processes. The plasmid for the experiment was PET15B and the sequence also included code for a bioaffinity tags at the N-terminus and C-terminus of the expressed protein, a His-tag and Strep-tag. If the entire protein is expressed, then the affinity tags at either end can be used to determine if the protein of interest was synthesized in entirety. The strep-tag was exploited for the purification of the protein with a streptactin affinity column. A subsequent western blot of the His-tag confirmed that the entire protein was expressed via the recombinant method, data shown in the appendix A30. For addition confirmation, protein samples were sent to MS-Bioworks to be characterized by mass spectrometry and sequence alignment. The MS-Bioworks report supported the presence of the protein biomarkers by high sequence identity, report in appendix A30.

3.4.1.2 ManLAM

The ManLAM from *Mtb* strain CDC 1551 was purified from the bacterial extract, characterized, and quantified by Colorado State University. Purification was completed with an octyl sepharose column and eluted with 1-propanol. The molecule is approximately 17.4 kDa and its structure can be reference in Figure

2.3. The solution of ManLAM was later lyophilized to remove the volatile solvent and shipped to CU-Boulder in 500 µg aliquots.

3.4.2 Selection

Both the ManLAM and protein biomarker selections were completed in a similar matter, specific details in the experimental methods. It was hypothesized that the pyridyl modification would produce the best aptamers to ManLAM and that the tryptyl amino modified nucleotide would likely produce the best protein aptamers, based off of prior research in carbohydrate and protein SELEX.^{79–81,84–88} A selection was performed for each biomarker using each modified-nucleotide available, at least 3 unique selections were performed for each biomarker. The selections with prospects of containing aptamers were further sequenced and investigated by characterization techniques.

Prospect for success and progress of a selection was monitored using a quantitative PCR method. qPCR is a sensitive method that both amplifies DNA sequences and quantifies them by use of fluorescent molecules that intercalate into dsDNA. For each selection round, the evolved pool is split and half is exposed to a target coated magnetic beads and the other half exposed to bare magnetic beads, as a negative control. If the evolved pool is being enriched during the selection, then the pool exposed to the target will amplify before the negative control. Figure 3.3 shows an example of a PCR trace from the MT3444 selection in round 6 that utilized the tryptl amino modified nucleotide. The qPCR trace indicates that the aptamer sequences in the evolved pool have a higher affinity for target coated magnetic beads and lower affinity to only the magnetic bead platform.

In each selection round pressures are added to the evolved pool in order to eliminate non-specific or low affinity binders. The first step is called counter-selection; the evolved pool is exposed to bare magnetic beads and a protein competitor buffer. Afterwards the bare beads are removed and the evolved pool is incubated with biomarker coated magnetic beads and then the beads are washed to remove loosely bound aptamers. Further pressure is added from round to round by decreasing the moles of biomarker bound to the magnetic beads and increasing the stringency of the washes. The selection rounds are continued until either the PCR traces indicate a 12 cycle separation between the target and

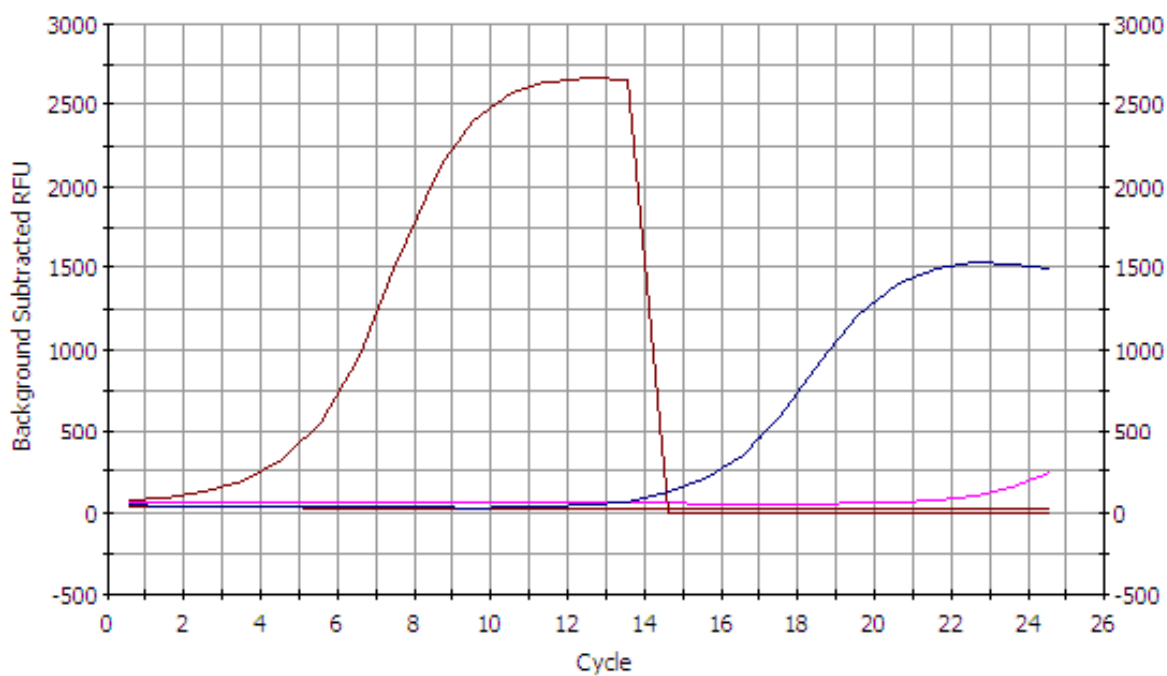


Figure 3.3. A PCR trace from round 6 of the MT3444 selection. The maroon trace is from the target pool, and it drops low in cycle 13 after the sample was removed from the instrument. The navy trace is the negative control pool. The pink trace is pcr control to determine when or if the primers are interacting with each other.

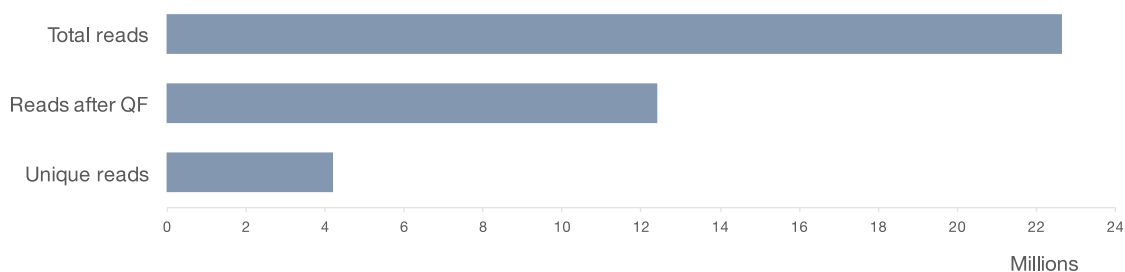
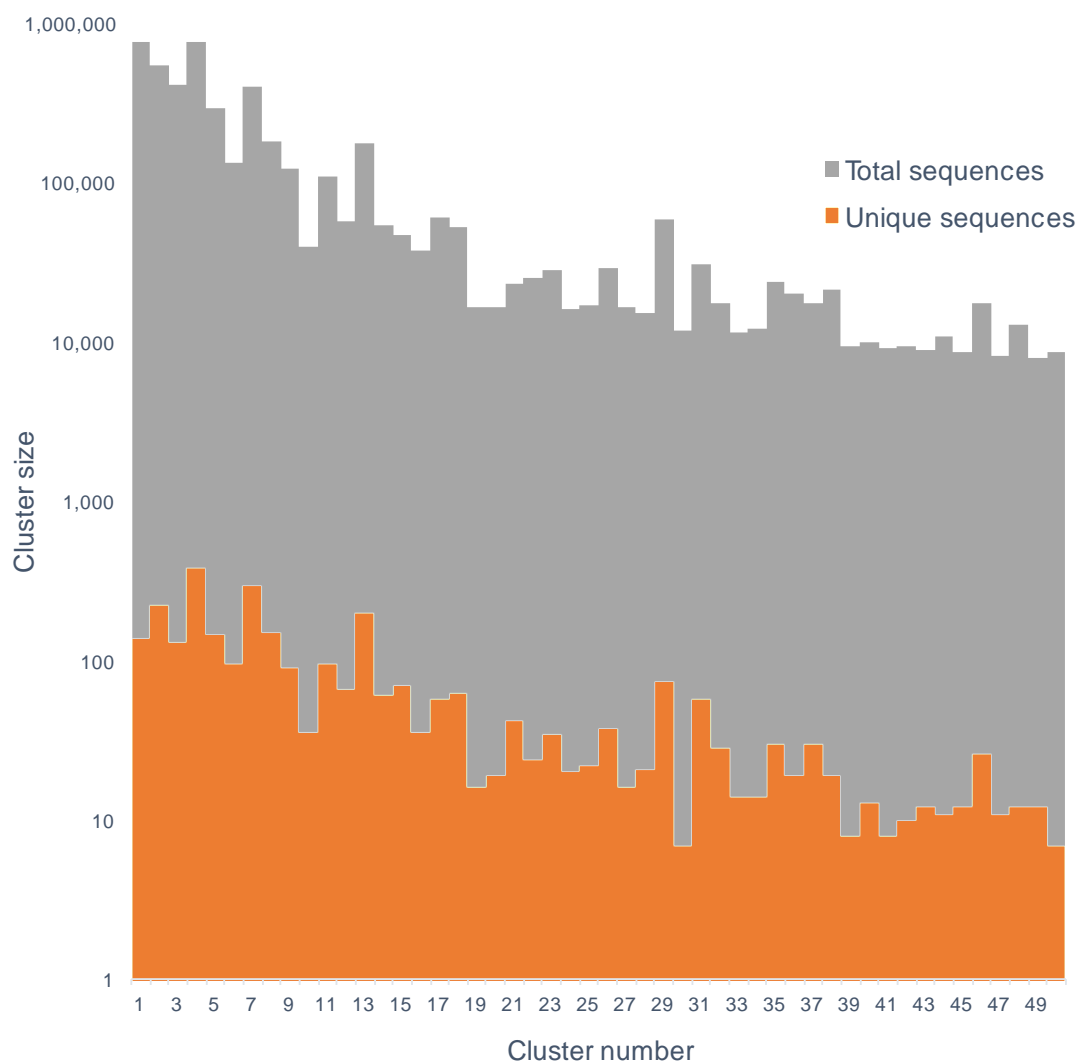
negative control traces, or the PCR traces show no indication of separation between the target and negative control. If a selection is successful there should be many cycles of separation between the target and negative control PCR traces. Separation is determined by the cycle difference from inflection points of two PCR traces.

If the selection is deemed successful, then the evolved pool of aptamers will be sequenced by either high throughput method, or by cloning and Sanger sequencing. Both methods were employed to sequence evolved pools. The ManLAM, MT3444, and MT1721 selections occurred early in the project, so they were cloned into plasmid and Sanger sequenced. Whereas, the MT2462 selection was recently completed so the evolved pool was sequenced via high throughput sequencing. After sequencing, results are first analyzed to isolate individual candidate sequences, and then by characterization methods such as fluorescence anisotropy.

3.4.3 Sequence Analysis of Evolved Pool

Sequencing results can be overwhelming when it becomes necessary to choose an individual sequence to test from data containing 100-4,000,000 unique sequences. Computational analysis is employed to group sequences according to sequence similarities. Two programs were employed to group the sequences, Daughter of Sequence Alignment and FASTAptamer.⁸⁹ These programs determine conserved regions, when in multiple sequence alignments there are sets of nucleotides with matching nucleotides that do not contain gaps. The conserved regions are then used to create groups of common aptamers, a.k.a 'families' or clusters. The summary of data from the sequencing of the MT2462 selection's

evolved pool of figure 4.3B and 4.3C exhibits family groups and also conserved regions of families with a large amount of members. An individual sequence can then be chosen from each family

A**B**

C



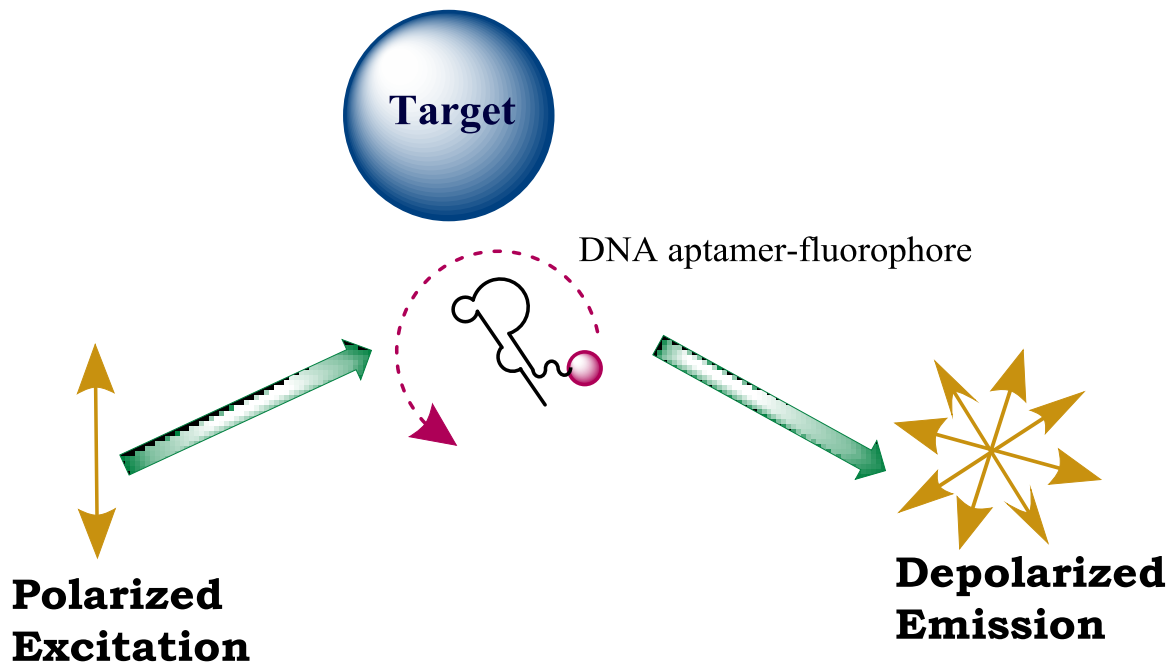
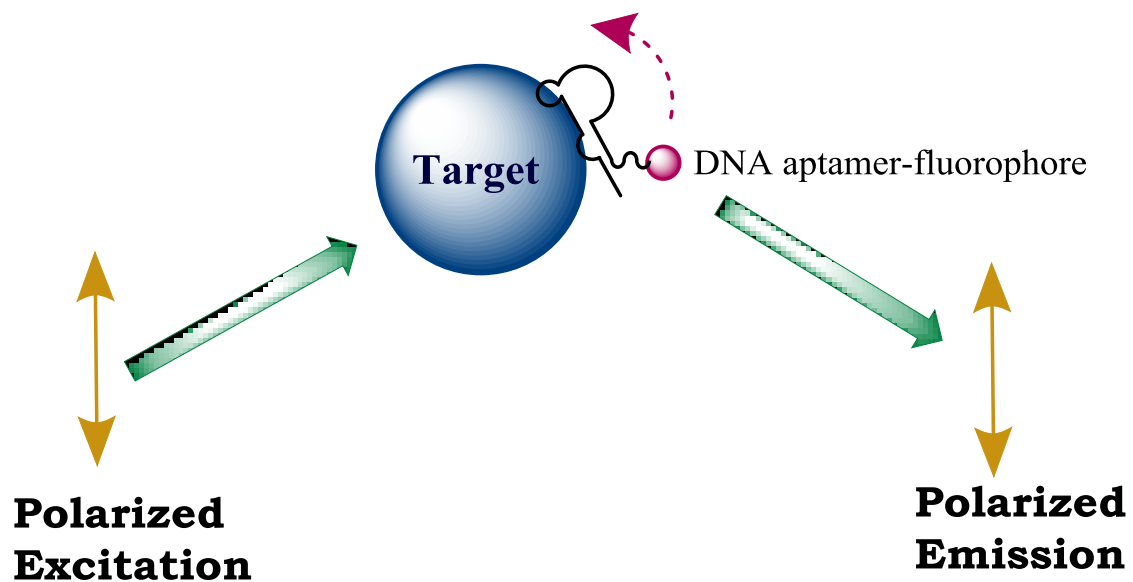
Figure 3.4 Summary of the computational analysis data from the evolved pool of a selection on MT2462. (A) The total number of sequences before and after quality filtering. (B) families on the X-axis and the size of their family on the Y-axis. (C) Conserved regions of highly populated families. Also, the mostly conserved nucleotides have the largest amplitude.

to be investigated for its binding affinity and specificity.

There are several factors in choosing an individual sequence from a family that could be an aptamer, as it is not possible to test them all due to funding and time constraints. A family with a high frequency of reads and a corresponding large conserved region could be an indication of directed evolution, because the initial combinatorial library had a pool of random individual sequences. If the selection failed, then there should hypothetically many unique sequences that do not fit into families and have low frequency of reads in the evolved pool. Aptamers are often rich in purines and containing guanidine quartets; a sign of significant secondary structure.^{90–92} Polymerases do not incorporate modified-nucleotides as efficiently as natural nucleotides, thus if the sequence has high content of them it could be possible it could be an aptamer to the target; as the modified nucleotides are specifically chosen to expand binding opportunities with the target.^{83,93,94} Albeit there are many factors to consider when choosing a sequence to test, to determine if the aptamer binds the target it is necessary to employ binding affinity assays.

3.4.4 Binding Affinity and Specificity

When determining the binding affinity of a molecule to a ligand it is vital that the system reach equilibrium. Some methods are better for achieving true equilibrium; such as fluorescence polarization anisotropy (FPA). FPA is a technique that offers the ability to probe binding affinity at true thermodynamic equilibrium in real-time with sample in solution free from complications caused by non-specific binding.^{95–99} In this assay, FPA tracks the local motion of a fluorophore labeled aptamer as it interacts with a polarized excitation source.^{100–104} In a

(A) No Binding**Rapid Tumbling****(B) Target Binding****Slower Tumbling**

conventional FPA assay, as depicted in figure 3.5, the rapidly tumbling fluorescent molecules in solution cause the dipoles of the excited molecules to rotate out of alignment relative to the dipole of incoming polarized light. When a fluorescent molecule binds a larger molecule it causes the tumbling to slow and the incident light to maintain polarization. The extent of polarization of a fluorescent molecule is calculated by its anisotropy (r). Perrin equation, equation 1, mathematically relates anisotropy to fluorescence lifetime (τ) and the Debye rotational relaxation time constant (θ).¹⁰⁵ θ is dependent on the local solution environment like the temperature (T) and viscosity (η); in addition to the volume of the rotating molecule (V).¹⁰⁵ Therefore, if the temperature and viscosity are constant, then the change in anisotropy is due the change in size of the fluorescent molecule. In the case of a fluorescent aptamer, the θ will increase with binding to a target.

$$\text{Eq.3.1} \quad \frac{r_0}{r} = 1 + \frac{3\tau}{\theta} \quad \text{Eq.3.2} \quad \theta = \frac{3\eta V}{RT}$$

Equation 3.1 The fundamental equations for FPA.

Unlike conventional FPA binding assays, the fluorescent aptamer sequences for the proteins biomarkers assayed demonstrated a negative change in anisotropy when bound to the target. This phenomenon has been seen previously in aptamer-based FPA assays.^{100,106} It is possible that the anisotropy decreases upon binding the biomarker target when certain types fluorophores are on the 5' end of

Figure 3.5 Fluorescence polarization anisotropy assay. (A) The excited emission from a fluorophore labeled aptamer remains depolarized as it rapidly tumbles in solution, until (B) the aptamer binds the target which slows tumbling and causes the signal to remain polarized.

the aptamer primer, such as CalFluor610. A fluorophore's local motion can be restricted due to interactions with the nucleotide bases of the aptamer, and then an induced fit change, from binding the target, releases the fluorophore allowing for greater motion. In this case the anisotropy change will decrease due to the fluorescent molecule obtaining more rotational freedom. The data has been displayed as the overall change in anisotropy ($\text{Anisotropy}_{\text{initial}} - \text{Anisotropy}_{\text{final}}$).

3.4.4.1 FPA assays of Fluorescent Aptamer sequences to Biomarkers

The FPA assays were designed to minimize variables that could cause non-specific changes in anisotropy and minimize background. Calfluor 610 excites at 590 nm and emits at 610 nm, wavelengths outside the range of intrinsic protein fluorescence, from urine proteins which would interfere with the urine assays. Volume was not increased by more than 8% of the initial assay volume of 180 μL . This control was meant to minimize noise and keep the fluorescent signal in the linear range, and was determined by assaying buffer into a cuvette of fluorescent aptamers, data shown in appendix A14. Assays were initially conducted to determine the minimum time necessary for the binding to achieve equilibrium. The solution is considered equilibrated when the anisotropy stabilizes to one value. Subsequently after each addition of protein to the cuvette, the solution was allowed to incubate until the equilibration time was met. Protein was added until the anisotropy plateaued, or if there was no statistically relevant change after adding protein up to a concentration of 100 nM. Controls have been included in the appendix A13-14, which show that any significant change in anisotropy is due to only specific binding of an evolved aptamer to its target. FPA control assays

included: a buffer only control, a scrambled aptamer sequence, random library, and a positive control with the VEGF aptamer.

The data gathered from the binding assays are used to determine the aptamer's affinity for its target. The data is inputted into a program, Graphpad Prism, which uses non-linear regression calculation with specifically single site binding. Post analysis, the program provides a value for the dissociation constant and the standard deviation at 95% confidence level. All dissociation constants reported here were analyzed by this method. The dissociation constant, K_d , is the propensity for a bound ligand to dissociate into its components, as shown in equation 3.3. K_d relates to affinity inversely, thus the best aptamers will have the smallest K_d .

Eq. 3.3 **Aptamer · Biomarker \leftrightarrow Aptamer + Biomarker**

$$K_{\text{dissociation}} = \frac{[\text{Aptamer}][\text{Biomarker}]}{[\text{Aptamer} \cdot \text{Biomarker}]} = \frac{1}{K_{\text{affinity}}}$$

Equation 3.3. The formula for determining the K_d .

Figures 3.6-3.8 were FPA assays from the characterization of aptamer sequence N18, which has affinity for protein biomarker MT3444. The first FPA investigation was done in selection buffer; the optimal binding conditions for the aptamer to bind its target. This data shows true binding without matrix effects, see figure 3.6. As a cut off, If the candidate aptamer had a K_d greater than 100 nM including standard deviation in buffer, then it was considered a poor affinity reagent and had no further testing. The investigation continued in urine to determine if the aptamer still had affinity despite exposure to urinary proteins. It was evident the aptamer suffered from matrix effects; figure 3.7, the dissociation

constant increased 4 fold compared to buffer. It was possible that the variable salt and protein content in the urine was either causing non-specific binding, degrading the aptamer, or denaturing the aptamer. Degradation could be possible if nucleases were present in the urine. To determine if degradation occurred aliquots of aptamer were incubated in urine for up to an hour, the amount of time to run the FPA assay. Gel electrophoresis was then performed on the samples, gel image in appendix A12, and no apparent degradation was visible. If degradation occurred there would be a light colored smear in the gel below the prominent aptamer band at ~92 base pairs. If the urine matrix was denaturing the aptamer, then performing the FPA assay in urine dialyzed against selection buffer should show a decrease in the K_d , results in figure 3.8. The results indicate an improvement in binding, but equivalent to the original K_d in buffer. The binding curves responsible for the dissociation constants in table 3.1 can be found in the appendices A9-A11 and figures 3.6-3.8.

Table 3.1 Aptamer Dissociation Constants (nM) for Specific TB Biomarkers

Aptamer ID	Target	Buffer	Urine	Urine Dialyzed Against Selection Buffer
18	MT3444	34.9 ± 15.5	121 ± 25.2	92.1 ± 10.4
01	MT3444	27.3 ± 8.8	78.9 ± 10.4	48.2 ± 5.1
24	MT3444	8.93 ± 3.89	N/A	
9	MT1721	80.0 ± 39.0	N/A	
CS09	ManLAM	14.6 ± 9.14	N/A	

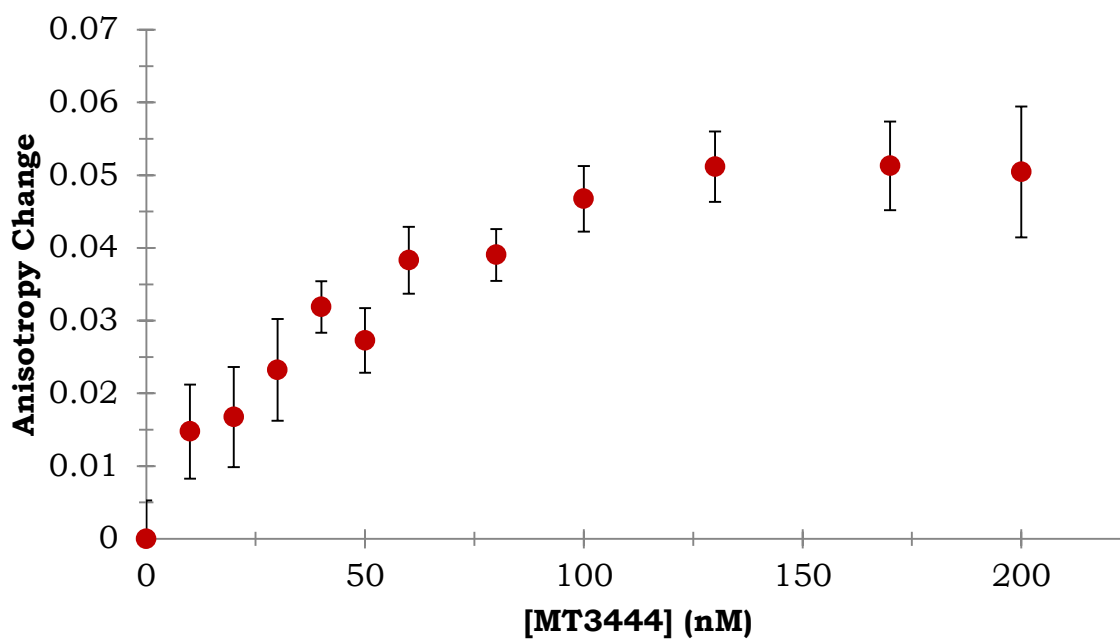


Figure 3.6. FPA assay binding curve of sequence N18 for its target MT3444 in selection buffer. The dissociation constant was determined by a non-linear regression program, Graphpad prizm, to be 34.9 ± 15.5 nM.

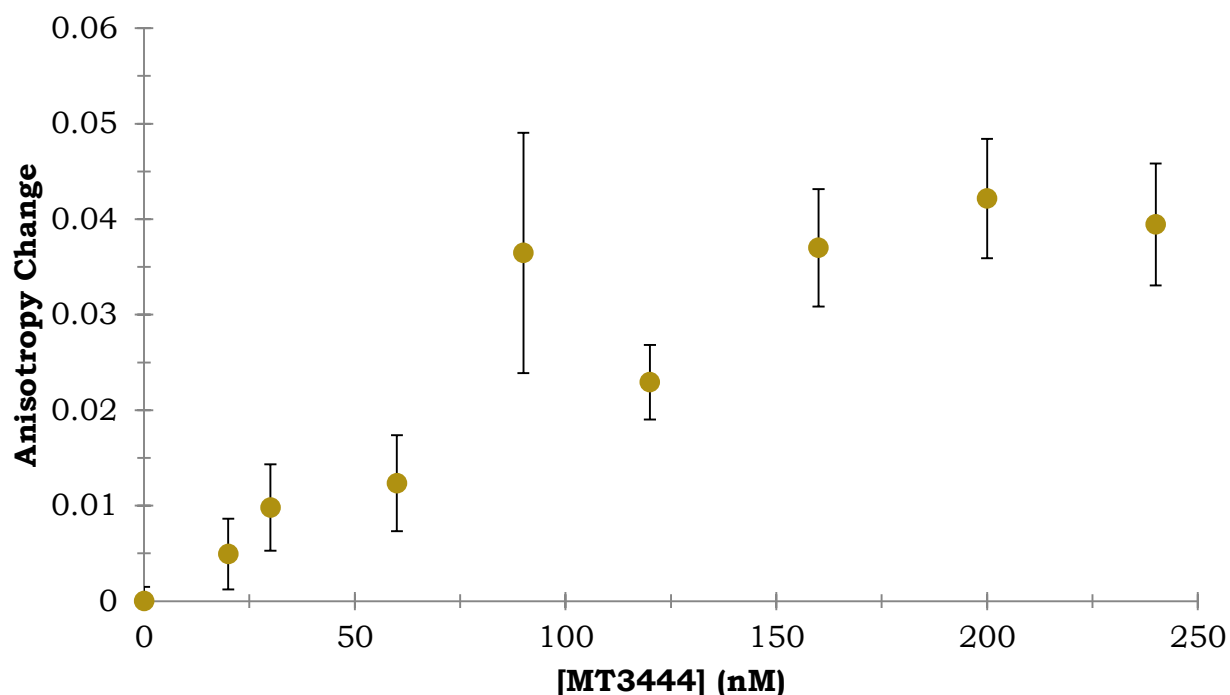


Figure 3.7. FPA assay binding curve of sequence N18 for its target MT3444 in non-endemic urine. The binding curve for this assay has a larger dissociation constant and each point has a larger standard deviation. The dissociation constant was determined to be approximately 121 nM.

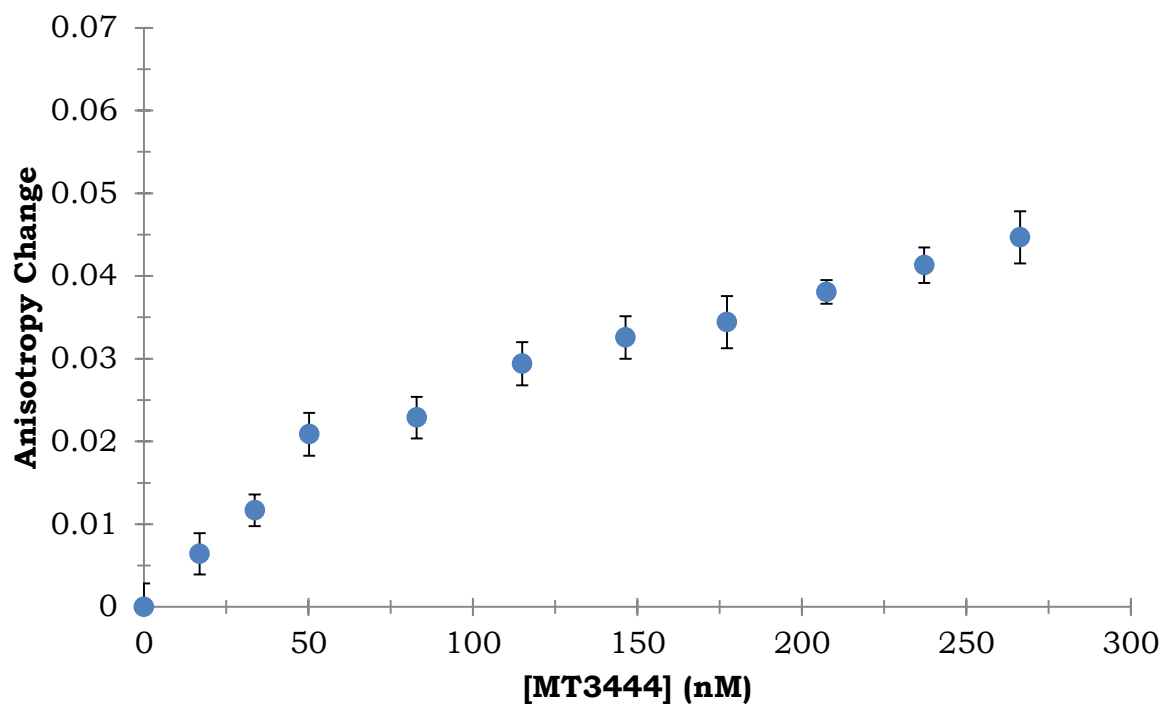


Figure 3.8. FPA assay binding curve of sequence N18 for its target MT3444 in urine dialyzed against selection buffer for 24 hours. The dissociation constant was determined to be approximately 92 nM.

3.5.4.2 Tryptophan Quenching Assay for a Naphthyl Modified Aptamer to MT3444 Protein

A tryptophan quenching assay was also used to determine the binding of the aptamer to the protein.¹⁰⁷ It has been designed so that no modification of the protein or aptamer was necessary. The objective of this assay was to exploit the intrinsic fluorescence of the MT3444 protein's 7 tryptophan amino acids. So that when an aptamer binds the protein the DNA bases quench the fluorescence of the tryptophan. If the aptamer did not cause quenching or was not present there would be a linear increase in signal as more protein was added, shown in appendix A15. Typically, tryptophan is excited at wavelengths between 285-300 nm and emits at 310-350 nm depending on local environment. The minimal interference by the naphthyl groups from the aptamer sequence occurs when the protein was excited at 295 nm and emission intensity at 340 nm was recorded. Note, this

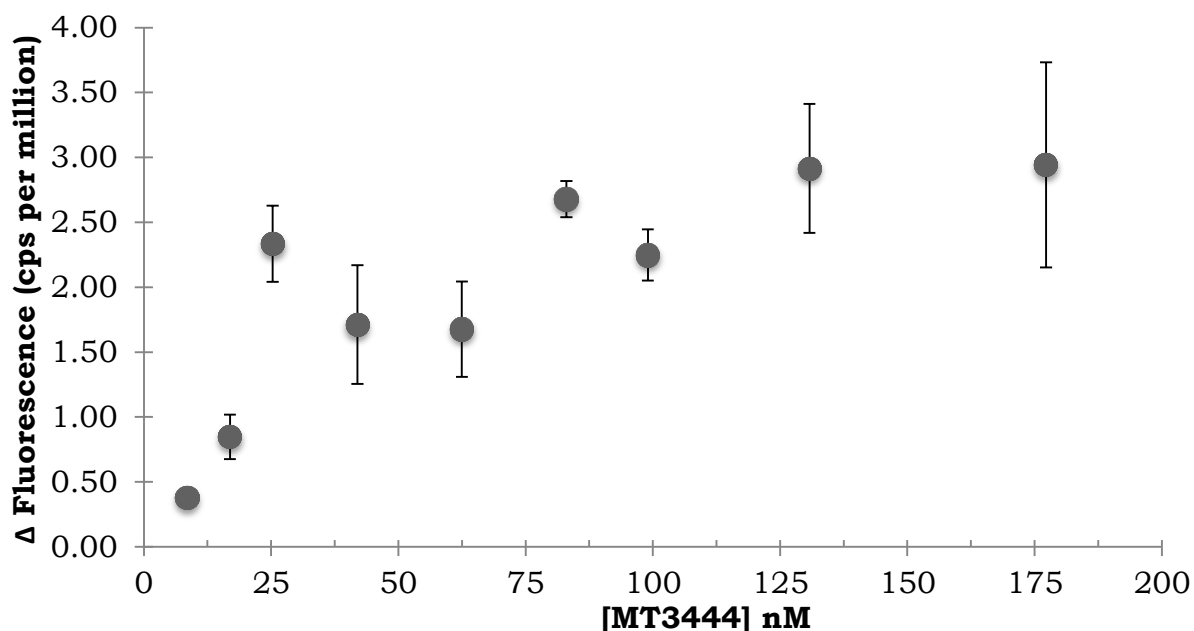


Figure 3.9 Tryptophan quenching affinity assay for sequence binding to the MT3444 protein. The dissociation constant for this assay was approximately 69 nM \pm 44 nM.

assay could not be used on aptamers with the tryptl amino modified nucleotides, because the modified nucleotide mimics the tryptophan amino acid side chain and would cause signal interference. Figure 3.9 below shows the quenching caused by the binding of aptamer N18 to the MT3444 protein. The K_d for N18 was determined to be $69 \text{ nM} \pm 44 \text{ nM}$, which is within the standard deviation of the FPA binding data for N18 in selection buffer.

3.5 Conclusions and Future work

The following project used *in vitro* selection to isolate modified DNA aptamers to TB biomarkers in urine and investigated the subsequent sequences for their capability for use in a TB biomarker detection assay. Here modified DNA aptamers have been isolated to molecules implicated as possible *Mtb* biomarkers in urine: 3 proteins with gene designations MT1721, MT3444, MT2462 and a glycolipid called Mannose capped Lipoarabinomannan (ManLAM). Representative aptamers from distinct conserved families were tested to verify binding to their respective targets. Dissociation constants for the aptamers ranged from 9 to 80 nM. If these aptamers were to be incorporated into a urine-based assay, then it would be advisable to buffer exchange the sample with selection buffer for optimal binding. A next step would be to determine if the aptamers could still bind their target when tethered to a substrate surface, like the gold substrate in the SERS assay. Alternatively, it could be possible to develop an assay that could accommodate the aptamer. The aptamers from this project show promise, because they have dissociation constants in the nanomolar range and specific to their target, even in a human urine sample with sample matrices that can vary widely from pH 6-9 and variable salt concentrations^{108,109}

3.6 Methods and Materials

3.6.1 Polymerase Chain Reaction

PCR reactions were performed using a 5X master mix: 10 μ M each forward and reverse primers, 25 mM magnesium chloride, 5X as-purchased KOD XL buffer, 1X [Sybr Green I], 1.25 mM each dNTP, and 0.075 U/ μ l KOD XL polymerase. To 40 μ l of sample were added 10 μ l of 5X PCR Mix, and the reaction was cycled as follows; cycle 1: 96 °C for 2.5 minutes, 55 °C for 45 seconds, 71 °C for 30 minutes; cycle 2-25: 96 °C for 15 seconds, 71 °C for 1.5 minutes. The PCR reaction was monitored in real time and the traces were stored in a text file.

3.6.2 Primer Extension

Primer extension reactions were performed with the following 1X Primer Extension Mix: 15.0 μ M forward primer, 120 mM Tris-HCl at pH 7.8, 10 mM potassium chloride, 6 mM ammonium sulfate, 7 mM magnesium sulfate, 0.1% Triton X-100, 0.1 mg/mL bovine serum albumin, 0.5 mM each dNTP, and 0.025 U/ μ l KOD XL polymerase. Biotinylated PCR product or single-stranded synthetic, biotinylated DNA was incubated with an appropriate quantity of streptavidin coated, magnetic MyOne C1 Dynabeads with shaking at 1000 rpm for 15 minutes. The beads were washed 3X with 20 mM NaCl and if double-stranded PCR product was used, 20 mM sodium hydroxide was applied for 45 seconds. The beads were washed again 3X with 20 mM NaCl and the Primer Extension Mix was added. The reaction was shaken at 1000 rpm at 71 °C for 45 minutes. After incubation, the beads were again washed 3X with 20 mM NaCl and 85 μ l of 20 mM sodium hydroxide was added. After 45 seconds, 80 μ l of the sodium hydroxide is removed and neutralized with 20 μ l of 80 mM hydrochloric acid and 10 mM Tris-HCl.

3.6.3 Selection Incubation and Partitioning

Approximately 10 pmol of modified primer extension product was buffered in 50 mM HEPES, 100 mM sodium chloride, 5 mM potassium chloride, 5 mM magnesium chloride, and 0.01% Tween 20 at pH 7.4. The modified DNA was folded by heating to 96 °C for 2.5 minutes and then decreasing the temperature by 1 °C per 10 seconds, until a final temperature of 22 °C. The pool was then incubated for 30 minutes with 10 µl of magnetic beads on a rotisserie, as a counter-selection step, and the supernatant was removed and used for the selection round. The biotinylated selection target is then incubated with the pool and later in the round partitioned with MyOne C1 Dynabeads to the sample according to the manufacturer's instructions. The complex, aptamer-target-beads, were washed to remove loosely bound aptamers. The aptamer sequences were then eluted by increasing the pH for 5 minutes with 2 mM NaOH, and then neutralized with 8 mM sodium hydroxide HCl.

3.6.4 Cloning and Sequencing

For Sanger sequencing, cloning of sequences was accomplished by inserting dsDNA PCR product of the evolved selection pool into a plasmid containing the inserted DNA pool as a vector, created according to the manufacturer's instructions. The plasmids were transformed into bacteria. Transformations were followed by blue/white screening and growing of overnight cultures. The plasmids were then extracted using a mini-prep kit and sanger sequencing by Genewhiz. Plasmids were subjected to PCR and primer extension to create a matrix of modified DNA aptamer isolated sequences. For Next Generation sequencing, bar

codes were incorporated into each DNA pool through modified PCR primers and sent to the company.

3.6.5 Biotinylation of ManLAM

ManLAM (6 nmol) was dissolved in 250 μ l of 100 mM sodium acetate, pH 5.5, and chilled on ice. Sodium periodate was added to a concentration of 1 mM, and the reaction was incubated on ice for 5 minutes in the dark. After incubation, sodium sulfite (90 mM) was added and the reaction was incubated at room temperature for 10 minutes. The reaction was buffer exchanged into PBS, pH 7.4, using 10,000 MWCO Amicons. Biotin-PEG-Hydrazide was dissolved into DMSO at a concentration of 50 μ M and the stock was added to the LAM sample to a concentration of 15 μ M. The reaction was incubated at room temperature for 3 hours, and then dialyzed into dH₂O for 2 days. Quantitation of biotinylation was accomplished by the HABA-avidin fluorescence assay via the manufacturer's instructions and was found to be 80.5%.

3.6.7 Fluorescence Polarization Anisotropy

FPA experiments were performed with aptamers folded and tagged as described above. Reactamers were filled into a quartz cuvette at a concentration of 10 nM and a volume of 250 μ l in selection buffer. ManLAM was gradually added to the cuvette and pipette-mixed. After each addition, the sample was incubated for 15 minutes at room temperature, and the anisotropy value was recorded.

3.6.8 Tryptophan Quenching Assay

The protocol for this experiment was followed as described in chapter 33 of Methods in Molecular Biology, volume 148, “DNA-Protein Interactions: Principles and protocols.”¹⁰⁷

3.6.9 Protein Expression and Purification

The the plasmid for the proteins were transformed and protein expressed in BL21-Gold(DE3) Competent Cells as prescribed in its manual without exception.¹¹⁰ Following expression, the bacteria were lysed with a B-per kit and applied to the streptactin affinity column according to the manuals instructions. The samples were then characterized by PAGE, MS, Bradford assay, and western blot. Their final concentration was approximately 6 μ M in 100 mM Tris (pH 8) and 150 mM NaCl.

Chapter 4: Oral Bioavailability of 2.0 nm Diameter Gold Nanoparticles

4.1 Introduction

4.1.1 Potential of Gold Nanoparticle Use in Medicine

Nanometer-sized gold particles, including nanoclusters, nanorods, and nanoshells, are quickly becoming valuable tools to study, diagnose, and treat disease. With light extinctions that are remarkably large (10^6 - 10^9 M⁻¹ cm⁻¹) and tunable across the visible-near infrared spectrum, gold nanoparticles are being used to detect nucleic acids and proteins inside of live cells and from blood plasma with unprecedented limits of detection.^{111,112} In addition to treating a variety of cancers via mechanisms such as laser-induced thermal ablation.¹¹³⁻¹¹⁸ The ease with which gold nanoparticles can be functionalized with a mixed monolayer of small molecules, polymers, proteins, and DNA has also made them attractive platforms for the assembly of multifunctional drug delivery systems that are capable of specific cell and nuclear targeting and even transdermal delivery.¹¹⁹⁻¹²³ The potential for use of gold nanoparticles as imaging agents and therapeutic delivery systems is growing rapidly.

4.1.2 Oral Administration of Gold Nanoparticles

The promise of gold antimicrobials is the key motivation to explore the potential for developing gold nanoparticle antibiotics that are administered orally. The oral bioavailability of gold nanoparticles has been examined only to a limited extent previously. Albrecht added citrate-coated gold nanoparticles with diameters of 4 nm, 10 nm, 28 nm, and 58 nm to drinking water for administration to mice *ad libitum*.¹²⁴ With the exception of the largest nanoparticles, all particles were found

in the major organs at levels on the order of ones to tens of nanograms of gold per gram of tissue. The bioavailability of the nanoparticles as a percentage of the dose administered could not be calculated because the amount ingested was unknown. Schleh administered sulfonated triphenylphosphine- and thiol-modified gold nanoparticles from 1.8 nm to 200 nm in diameter to rats via oral gavage.¹²⁵ Positively and negatively charged thiols were examined, and >99.63% of the particles administered were found either in the gastrointestinal (GI) tract or feces regardless of size and charge. The conclusion from these studies is that gold nanoparticles are not absorbed in the GI tract to a large extent in both an absolute sense and relative to most small-molecule antibiotics.

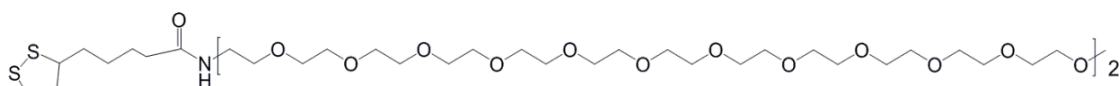
4.2 Oral Bioavailability Study of 2.0 nm Gold Nanoparticles

4.2.1 Design of Gold Nanoparticle Monolayer

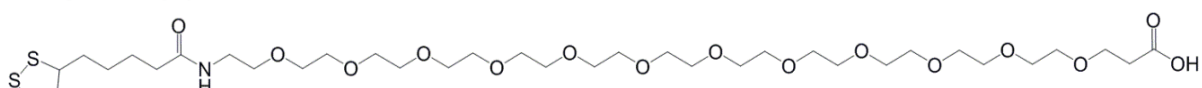
A significant limitation of gold nanoparticles currently is their low absorption efficiencies in the gastrointestinal (GI) tract following oral administration. This is likely to do natural defenses created by the body, like Peyer Patches and gastrointestinal mucosal barriers. Peyer patches, defend the body by endocytosing molecules from the intestines through microfold cells, then they are presented to macrophages that determine pathogenicity and possibly trigger the immune system to act.^{126–128} Mucosal barriers protect the body simply by preventing molecules from diffusing into the body by their size and charge.¹²⁹ In an attempt to identify ligands that facilitate gold nanoparticle absorption in the GI tract, the following study was executed to determine the oral bioavailability of 2.0 nm diameter gold nanoparticles modified with the small molecules p-mercaptobenzoic acid (*p*MBA) and glutathione (GSH), in addition to polyethylene

glycols (PEG) of different lengths and charge (neutral and anionic). The structures of the PEG ligands used in the study are displayed below in figure 4.1. PEGs were chosen because they have been shown to be absorbed in large quantities, up to 60% for PEG4.¹³⁰ They have also been found to diffuse through mucosal barriers better than many other molecules.¹³¹ It was decided to not use cationic ligands due to published data regarding their toxicity and high likelihood that they non-specifically bind proteins from bodily fluid.¹³² Here we show that GI absorption of gold nanoparticles modified with the small molecules tested was undetectable.

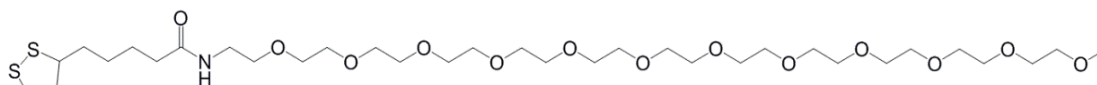
PEG24-Neutral



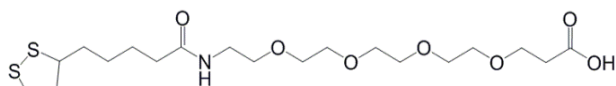
PEG12-Acid



PEG12-Neutral



PEG4-Acid



PEG4-Neutral

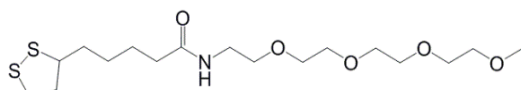


Figure 4.1. Structural illustrations of cyclic disulfide-terminated polyethylene glycol ligands.

However, the absorption of PEGs depended upon PEG length, with the smallest PEG studied yielding gold nanoparticle absorptions that are orders-of-magnitude larger than observed previously. As the oral route offers highest patient compliance for administering drugs and diagnostic reagents, these results suggest

that short-chain PEGs may be useful in the design of a platform for oral administration of gold nanoparticles.

4.2.2 Stability and Characterization Studies of the Gold Conjugates

In order to be absorbed in the GI tract and circulate systemically a nanoparticle must be able to avoid aggregation and chemical degradation as it travels through the stomach and into the intestines. Perhaps the most formidable challenge to nanoparticle stability along this route is pH. The pH in the mouse GI tract can be as low as 3 in the stomach and as high as 5 in the intestines.^{133,134} In humans the pH in the stomach and intestines is approximately 2 and 8, respectively.^{124,135} The changing conditions of different sections of the GI tract could alter ligand charge or cause ligand displacement that changes the physicochemical properties of the nanoparticle or leads to particle aggregation. To measure the stability of the nanoparticles in solutions with pH of 2 and 8, GSH-coated gold nanoparticles were synthesized and subjected to ligand exchange reactions to generate PEG-modified gold nanoparticle conjugates.

The nanoparticle solutions were then adjusted to pH 2 and warmed to 37 °C for two hrs. During this time, the plasmon extinction band of the gold nanoparticles was monitored by UV-visible spectroscopy to assess the stability of the nanoparticle conjugates, figure 4.2. After two hours, the pH was adjusted to 8 and the solutions were monitored for an additional six hours. No significant spectral changes were observed for the PEG conjugates over the entire pH and time range studied. A slight drop in the plasmon absorption band was observed for the *p*MBA-modified gold nanoparticles at pH 2 over the course of 2 hours, which likely indicates partial precipitation due to *p*MBA protonation. In contrast,

the plasmon band of GSH-modified gold nanoparticles appeared to sharpen over time at pH 2, which suggests that some size focusing (Ostwald ripening) may

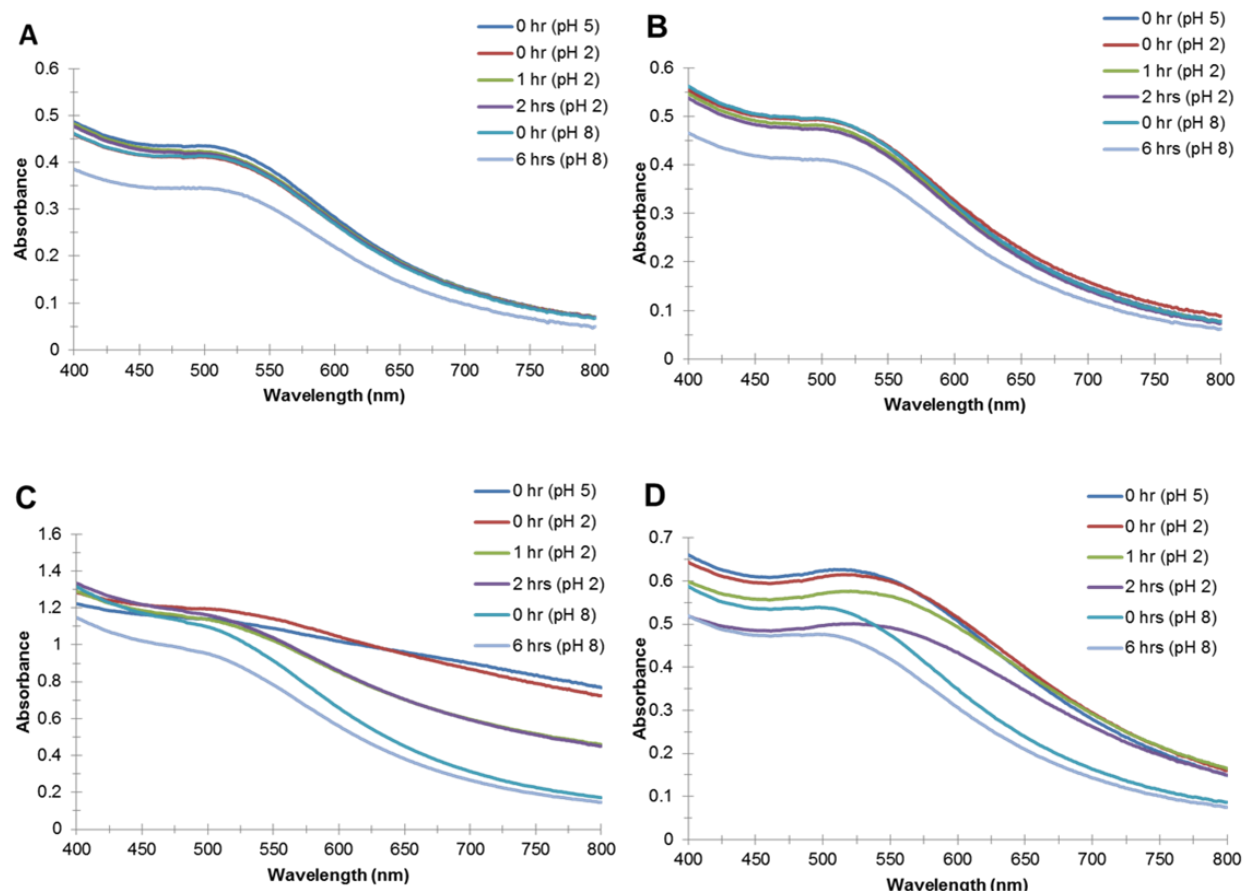


Figure 4.2. Gold nanoparticle stability assay simulating the pH and temperature of the human gastrointestinal tract. UV-Visible spectra of (A) PEG4-Acid, (B) PEG4-Neutral, (C) GSH, and (D) pMBA on ca. 2.0 nm diameter gold nanoparticles. See Experimental Methods section for further details.

occur.

Prior to determining pH stability, the gold nanoparticle conjugates were analyzed by NMR to qualitatively confirm ligand exchange, and by transmission electron microscopy (TEM) to measure particle diameter. Figures 4.3-4.4 below display the TEM images and the PEG4N NMR spectra,

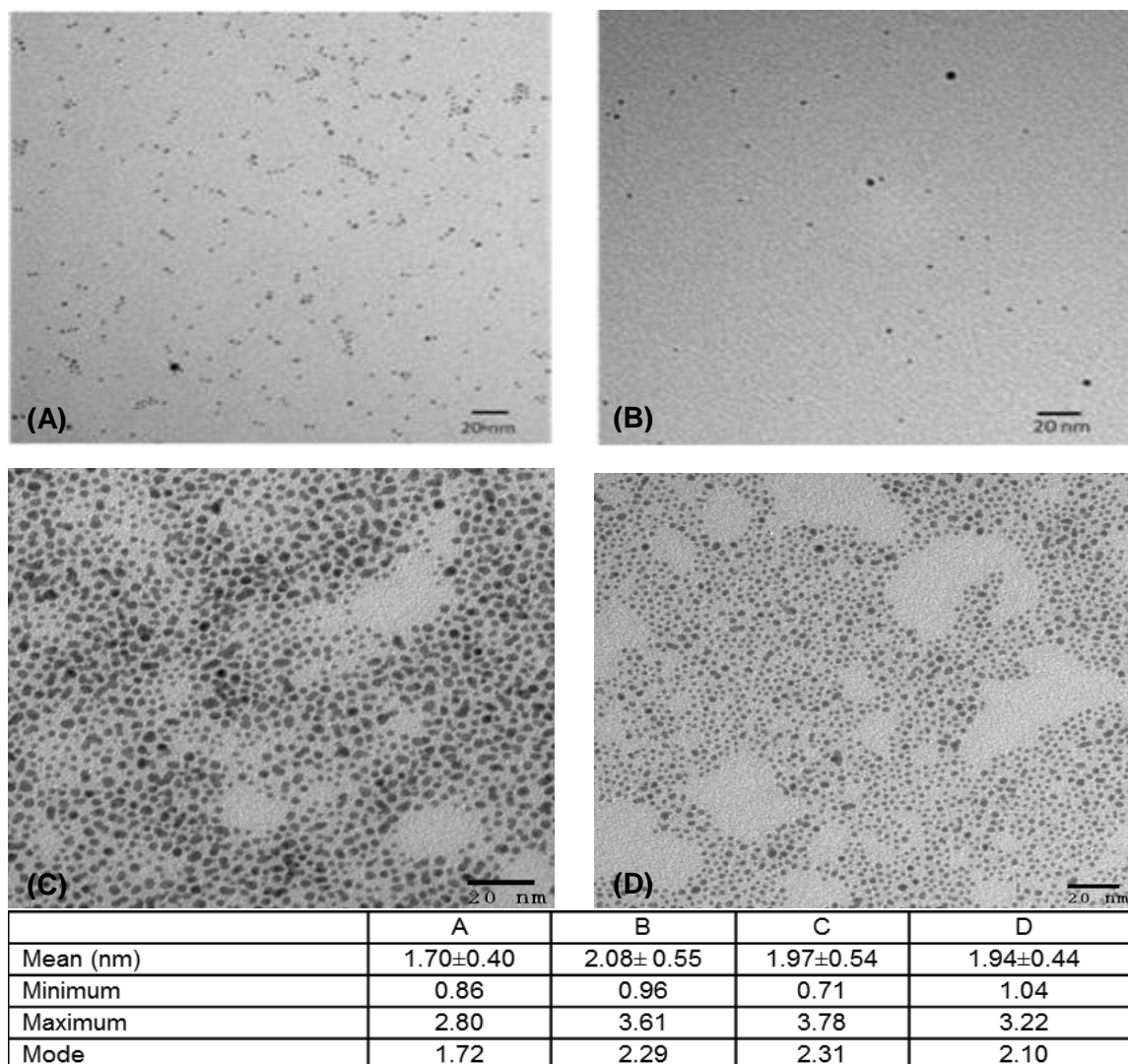


Figure 4.3. Transmission electron micrographs and size dispersity statistics of gold nanoparticles modified with (A) *p*MBA, (B) GSH, (C) PEG4N/GSH, and (D) PEG24N/GSH.

remaining NMR spectra can be seen in the appendices A16-A23. NMR showed that each PEG studied was able to displace GSH and bind the nanoparticle surface. NMR also suggested that the exchange yield was high, as GSH was not detected following ligand exchange and nanoparticle purification.

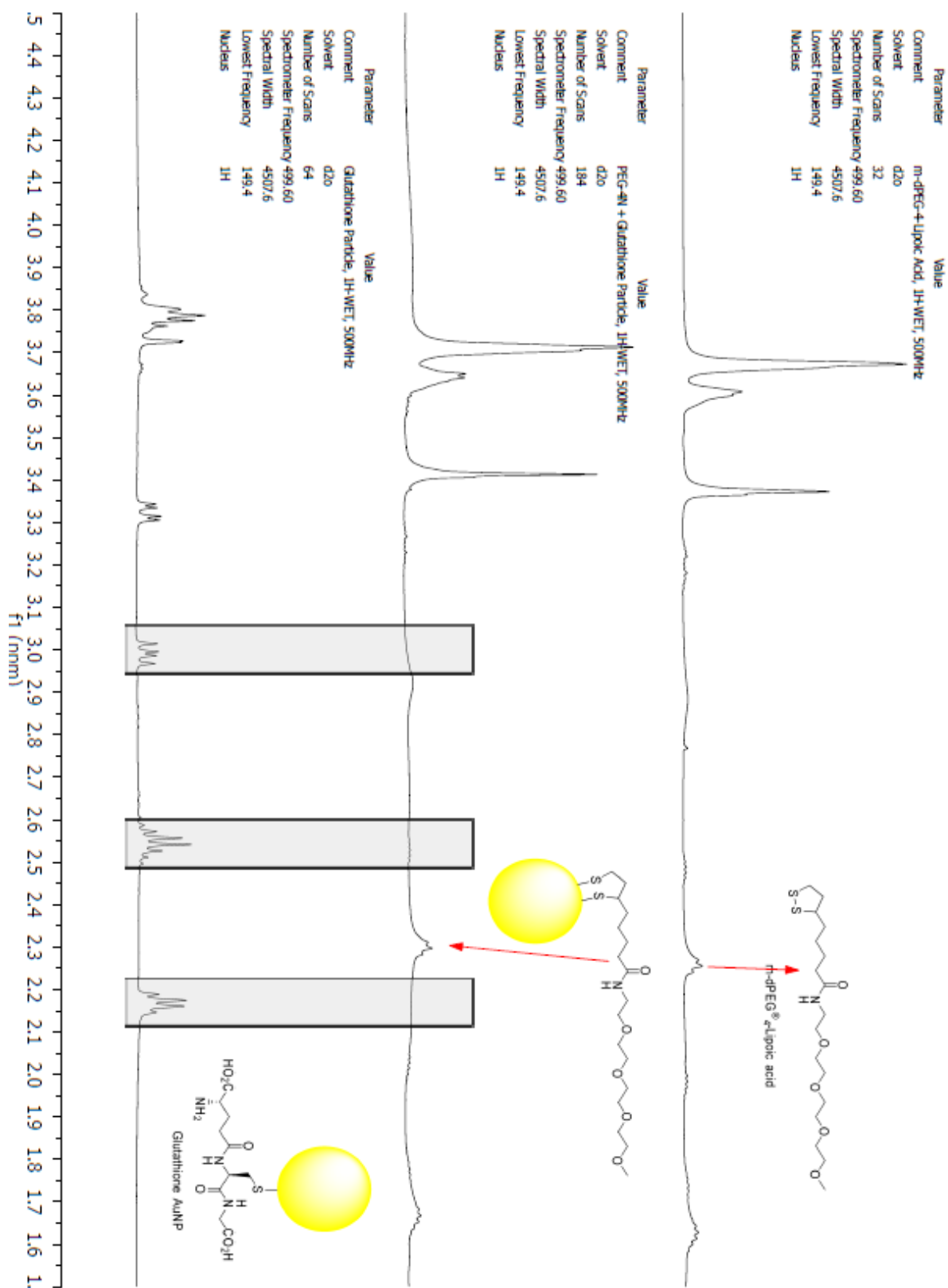


Figure 4.4. ¹H NMR spectra for a stackplot of PEG4N ligand/ PEG4N Au NP/ GSH Au NP. As the stackplot shows, there is signal from the PEG4N ligand on the gold surface and an absence of GSH signal.

4.2.3 *In Vivo* Oral Bioavailability and Distribution in the Mouse Model

Given their stability under conditions of pH that includes those found in the mouse GI tract, *p*MBA-Au, GSH-Au, and all PEG conjugates were advanced to oral bioavailability studies. GSH-coated gold nanoparticles have been shown to be non-toxic by subcutaneous injection up to and including 60 μ M.¹³⁶ Given this prior observation, 60 μ M concentrations were used for all initial gavage experiments (200 μ L administrations). An additional experiment was conducted on GSH particles at 120 μ M. Blood, urine, organs (heart, liver, lungs, spleen, kidney, stomach, and intestines), and feces were examined for gold content using ICP-MS. Urine was collected at 3 time-points, 1 hr, 8 hrs, and 24 hrs, as described previously. These values were then added (error propagated) to produce a renal output value over the entire 24-hr period, to represent the minimum gold excreted on average.

For the small-molecule adsorbates GSH and *p*MBA, no gold was detected in the urine, blood, or any of the organs tested, figures 4.5 and 4.6. Doubling the concentration of GSH-coated gold nanoparticles did not result in a detectable amount of gold in the blood or urine. This is not surprising, as large quantities of GSH alone (up to 3 grams) administered orally do not cross the GI tract in appreciable amounts.¹³⁷

The addition of PEG to the nanoparticles had a profound effect on GI absorption. The most surprising discovery was the high concentrations of gold detected in the blood and urine following oral administration of both the acid and neutral forms of the PEG4-modified nanoparticles, figures 4.5 and 4.6. Detectable levels of gold were also discovered in the primary filtration organs, liver and

kidneys; confirming gold absorption followed by systemic circulation and organ targeting. In contrast to the PEG4-modified nanoparticles, gold was not detected in the blood, urine, or tissues for nanoparticles modified with either the neutral or carboxylate forms of PEG12. Gold was also undetectable in the blood and urine for the PEG24 conjugate. However, a relatively small quantity of gold was found in the liver and kidneys for PEG12 gold conjugates, which suggests that they were absorbed in the GI tract, circulated systemically, and were concentrated in the filter organs. Thus, while there was no noticeable dependence of GI absorption upon PEG charge, there appears to be a dependence upon PEG length, with shorter chain PEGs providing increased GI absorption.

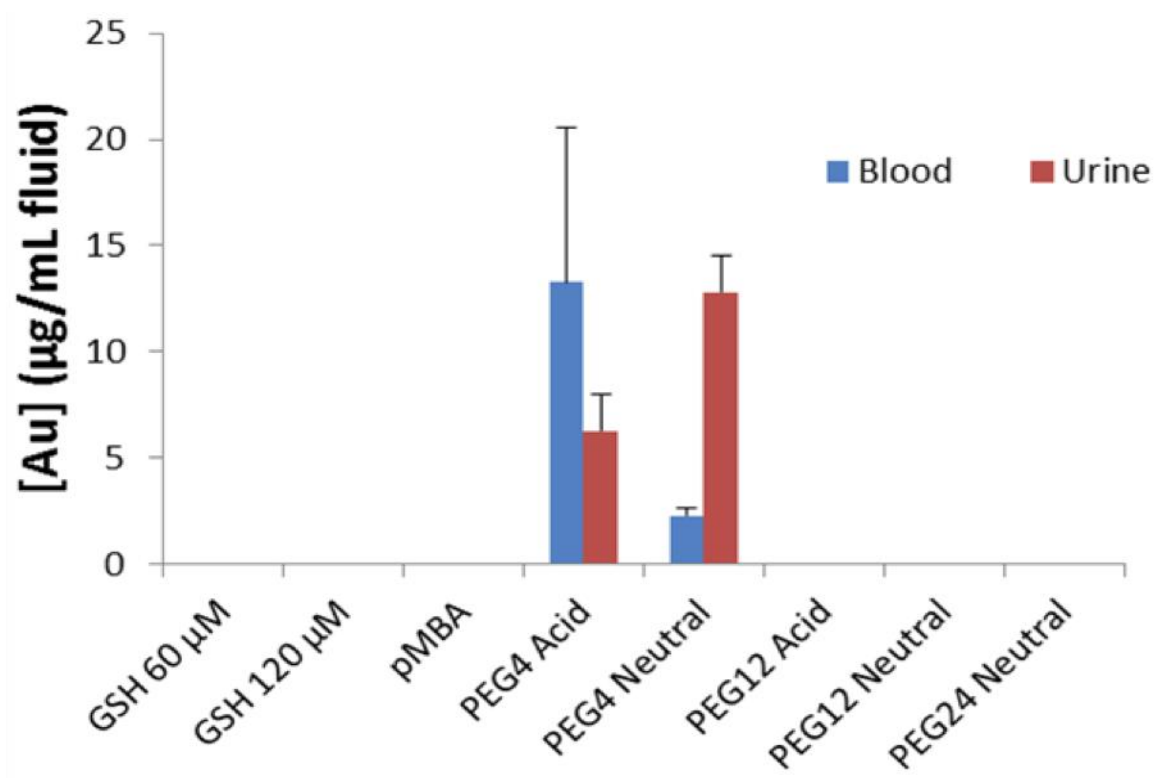


Figure 4.5. Gold accumulation in blood and urine over a 24-hr period. Samples were collected at 1-hr, 8-hr, and 24-hrs and the gold concentrations measured at each time point summed to generate the bars shown. Gold concentrations were undetectable in all administrations except for the PEG4 ligands.

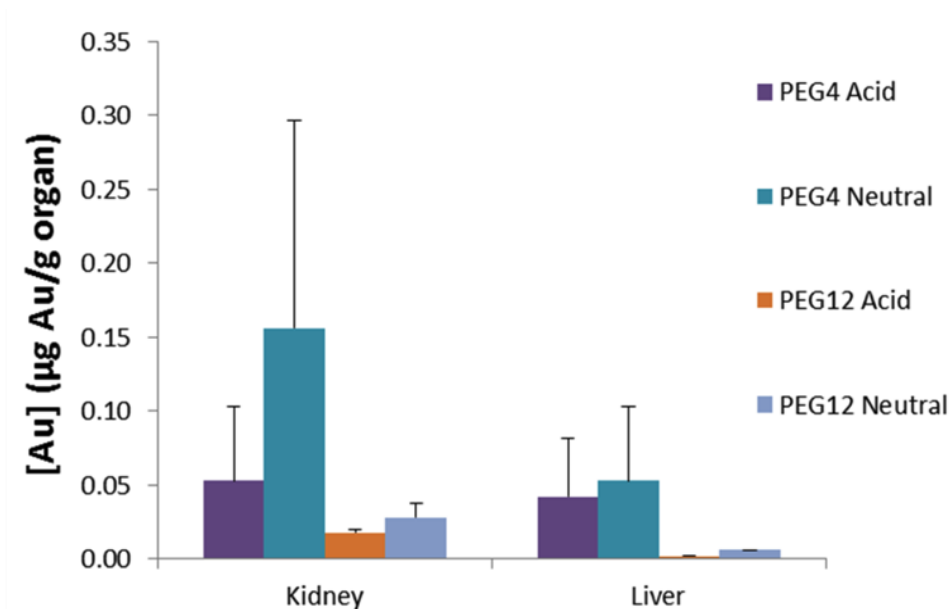


Figure 4.6. Gold distribution in the kidneys and liver for gold nanoparticles administered orally. Detectable concentrations of gold were noted for PEG₄ and PEG₁₂ modified particles, indicating absorption in the GI tract. PEG₄ had the highest accumulation of all formulations, indicating PEG length may be responsible for gastrointestinal absorbance. No gold was detected for the other modified nanoparticles.

TEM of urine samples collected following oral administration of the neutral PEG₄-modified nanoparticles revealed particles with average diameters of $2.03 \text{ nm} \pm 0.7 \text{ nm}$, figure 4.6. As these nanoparticles are similar in size to PEG₄-Au nanoparticles prior to administration $1.9 \text{ nm} \pm 0.4 \text{ nm}$, figure 4.3, we presume that the source of gold in the blood, urine, and organs was gold nanoparticles that traveled through the GI tract and circulatory system intact. Together the ICP-MS and TEM data suggest that PEG₄ dramatically increased the oral bioavailability of gold nanoparticles compared to what is afforded by small-molecule ligands such as *p*MBA, GSH, or citrate.

Final consideration of the fate of these gold nanoparticles following oral administration was focused on the components of the GI tract itself—the stomach, intestines, and excreted feces, figure 4.8. Feces were collected in the same manner and at the same time points as blood and urine and their values summed for comprehensive analysis over a 24-hr period. Stomach and intestines were removed at the same time as the other organs, 24-hrs post administration. The data show that gold was present in the GI tract and excreted feces following administration of all of the nanoparticles. An increase in fecal gold mass with an increase in the concentration of GSH-Au nanoparticles administered was noted, indicating that input and output are correlative. In addition, the mass of gold

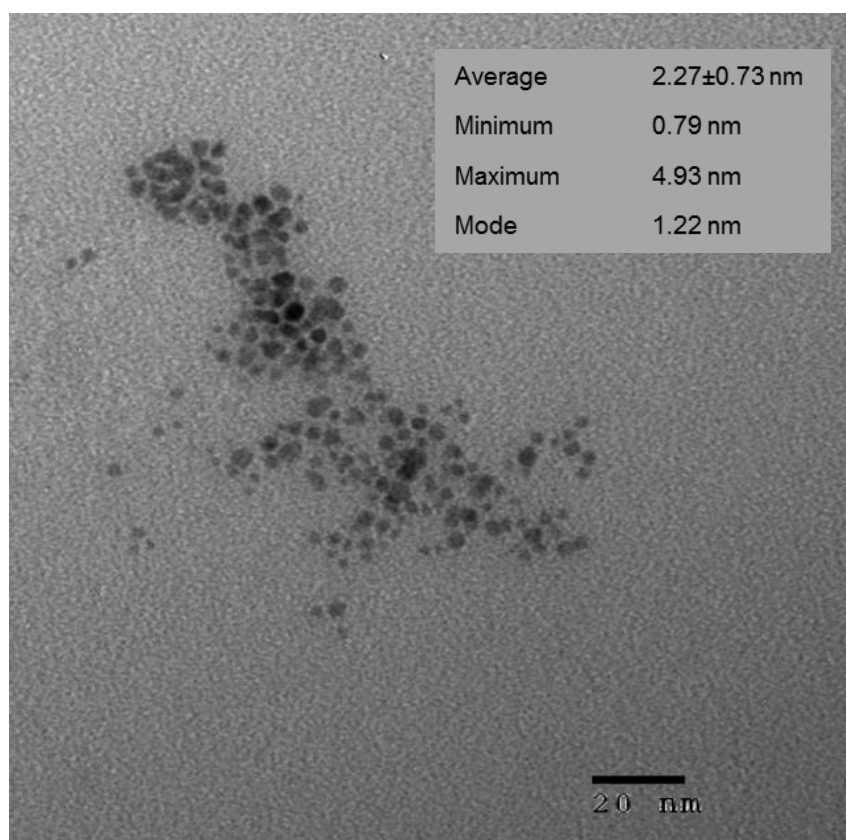


Figure 4.7. Analysis of mouse urine after oral administration of 60 uM PEG4N gold nanoparticles. Transmission electron microscope image of the putative gold nanoparticles concentrated from urine and their size dispersity.

detected in feces for nanoparticles modified with PEG24 was higher than its PEG4 counterparts (Student's T-test, 95% confidence interval), which is consistent with their relative absorption efficiencies. No statistical difference was noted between the acid and neutral end groups with regard to excretion in fecal material.

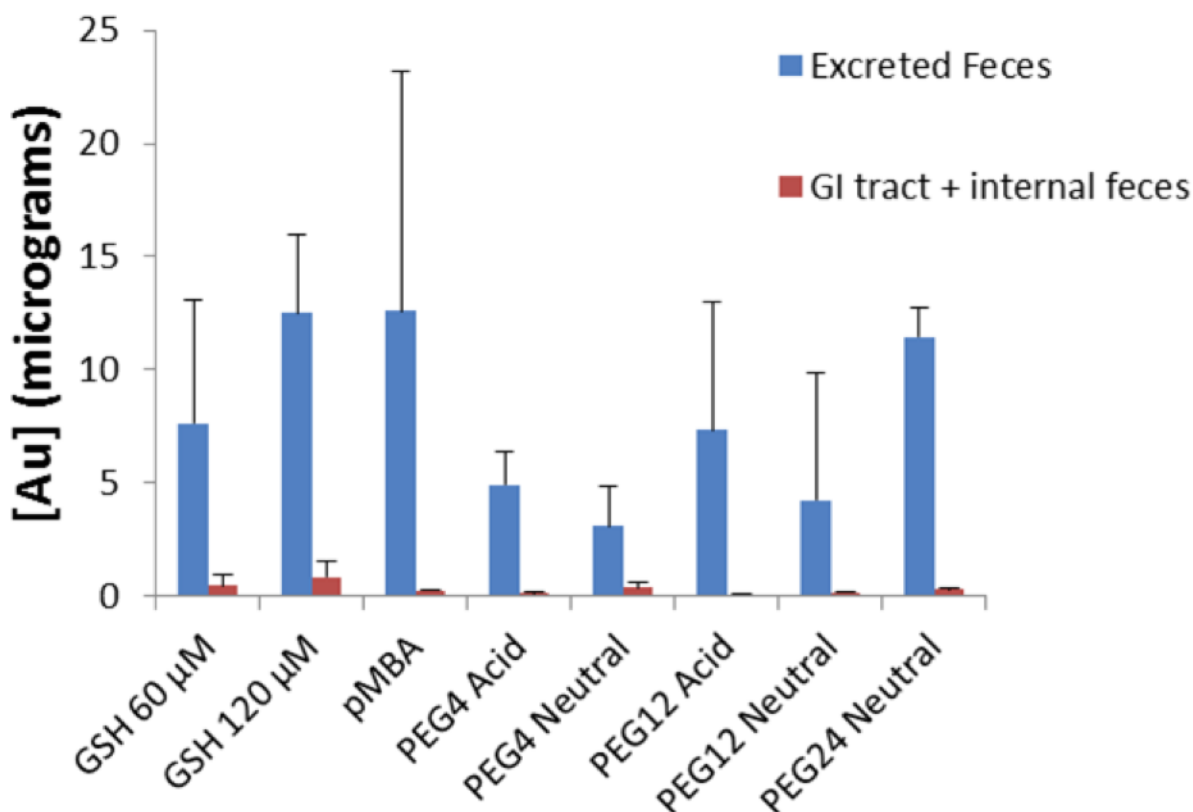


Figure 4.8. Fecal and gastrointestinal distribution of gold nanoparticles. Samples were collected at 1-hr, 8-hr, and 24-hrs and the gold concentrations measured at each time point summed to generate the bars shown. Nanoparticle concentrations were 60 μ M except where indicated.

The goal of this study was to begin to elucidate some basic design principles for the assembly of 2.0 nm diameter ligand-modified gold nanoparticles with increased oral bioavailability. Two small molecules were examined as ligands, the zwitterionic GSH and the anionic pMBA. Gold conjugates modified with these

ligands were not detected in blood, urine, or any of the organs examined. Monolayers containing PEG, however, increased nanoparticle absorption in the GI tract dramatically, with the shorter PEGs providing increased absorption efficiencies. This trend could be a function of hydrodynamic radius as larger particles have been shown repeatedly to hinder the absorption process.^{124,125} However, this same trend has been noted even for free PEGs;¹³⁰ an increase in PEG molecular weight from 600 to 1,000 Daltons produced a decrease in absorption from 60% to 9%. The PEG4 ligands used in our study have molecular weights of 395 or 454 Daltons, relatively close to the free PEG with the best absorption efficiency.

Although the mass of gold detected in the blood and urine following administration of PEG4-Au nanoparticles was similar for the neutral and carboxylic acid PEGs, there was a difference in how the two types of nanoparticles were distributed. The PEG4-neutral nanoparticles appeared to be cleared via the renal system more rapidly, as they were found predominantly in the urine vs. the blood after 24 hrs. In contrast, the PEG4-acid particles were found in a larger proportion in the blood vs. the urine in 24 hrs. This is consistent with previous reports on gold nanoparticles modified with carboxylic acid and neutral PEGs, which showed longer circulation lifetimes for acid-terminated PEG-modified gold nanoparticles administered via subcutaneous injection.¹³⁸

Finally, although we cannot accurately calculate the percentage of gold nanoparticles that were absorbed in the GI tract because we did not collect all of the urine excreted over the entire 24-hr time course, we can place a lower limit on the absorption efficiency. For the PEG4-Acid, the mass of gold detected in the

urine, blood, and organs was on average 18 μg and the total mass administered was 360 μg . The minimum average amount absorbed into the systemic circulation was thus $\sim 5\%$. This is several orders-of-magnitude larger than reported in previous studies.

4.3. Development of a Drug Conjugate with Limited Oral Bioavailability

4.3.1 Collaboration and Intellectual Property Protection

This project has been conducted in collaboration with Eli Lilly and Company pharmaceuticals. It involves a small drug molecule that is owned by Eli Lilly and Company. Experiments in this project were conducted and analyzed critically by myself at the Feldheim lab and Eli Lilly scientists. Some potentially innovative ideas for this drug have been developed during this research; which have been patented or could be in the future. Due to the intellectual property rights at stake, the data for this chapter will be presented in a manner that protects said rights, yet provides an adequate understanding of the project objectives and achievements.

4.3.2 Limiting Oral Bioavailability of a 2.0 nm Drug Gold Nanoparticle Conjugate

In this project, the 2.0 nm gold nanoparticles synthesized would be utilized as a drug delivery platform for an Eli Lilly drug molecule. The main objective is to develop a gold nanoparticle platform that will direct the Eli Lilly drug molecule to its target in the intestines, yet inhibit its distribution into other parts of the body. Administered orally as a free molecule this drug has been shown to be taken up by the body through the gastrointestinal tract lining. Limiting this drug to the just the GI tract is vital, because non-specific absorption of it can cause deleterious effects to the gall bladder. Developing a gold nanoparticle platform for the Eli Lilly

ligand could improve its efficacy and increase a patient's margin of safety. This project will take the prior research and use it to develop a conjugate with minimalized gastrointestinal tract permeability.

4.3.3 Synthesis of Disulfide Drug Ligand

The first objective of the project was to modify the drug molecule so that it could be conjugated to a gold surface. One of the strongest interactions with gold involves thiolates, which is considered semi-covalent.¹³⁹ The strength of the sulfur-gold interaction is approximately 45 kcal/mol; in comparison, a covalent C-S bond has strength of 65 kcal/mol.¹⁴⁰ It has also been shown that a disulfide molecule could be more stable than a mono-thiol on the gold surface, because it could provide up to two sulfur gold bonds.^{141,142} For this reason, we chose to modify the Lilly drug with a disulfide linker. For stability and improved efficacy it occurred to us that using a spacer between the disulfide and the Lilly drug molecule could be beneficial. For this reason a specific length PEG was chosen as the spacer, because it would not increase hydrophobicity of the drug molecule like an alkane chain spacer. It is possible that the linker length would have to be optimized for maximum drug efficacy and minimization of absorption into other organ systems of the body. The organic chemistry challenges of this task were performed by our resident organic chemist, Dr. Ganghyeok Kim. The modification of the drug did not inhibit the drug's ability to bind to its extracellular protein target *in vitro* as determined by Eli Lilly.

4.3.4 Place-Exchange of Drug Molecule onto Gold Nanoparticle Surface

The next objective of the project was to conjugate the drug molecule to the surface of the gold nanoparticle. Two different base monolayers were chosen for

the 2.0 nm gold nanoparticles either GSH or *pMBA*, as their biodistribution was limited to the gastrointestinal tract. In previous Feldheim lab studies, most gold nanoparticle exchange reactions occurred in ultra-pure water. However, these exchange conditions did not work for the hydrophobic Eli Lilly drug, which required an organic solvent to be soluble. To conserve reagent, the Lilly drug was dissolved in the dimethyl sulfoxide (DMSO). A new exchange solution had to be developed to optimize gold surface coverage. A systematic approach was taken to find an optimum DMSO concentration, exchange ratio of drug to gold, pH, and other solution. Ultimately an exchange solution of 10% DMSO and 90% ultra-pure water adjusted to pH 10 gave optimum results. Optimum results are determined by the highest coverage of drug on particle (mole drug/mole nanoparticle), which required the least quantity of drug for the ligand place exchange reaction. Post-exchange, the gold drug conjugates were concentrated on 10 kDa molecular weight cut-off filters and then dialyzed for 48 hours into a 1x phosphate-buffered saline solution at pH 7.4. A table displaying the gold nanoparticle exchange conditions and results are in appendix A28.

4.3.5 Characterization and Purification of Drug Gold Conjugate

Characterization of the gold-drug conjugates were performed via UV-Vis spectroscopy, transmission electron microscopy (TEM), nuclear magnetic resonance (NMR), polyacrylamide gel electrophoresis (PAGE), high performance liquid chromatography (HPLC), and high performance liquid chromatography in tandem with either mass spectrometry (LC-MS) or a UV-Vis detector. Coverages of drug on particle were determined by UV-Vis spectroscopy data (see appendix A27 for drug spectra and calibration curve). The drug molecule (268 nm) and gold

nanoparticle (510 nm) absorbed light at specific wavelengths in the visible range. From this observation, calibration curves were plotted taking into consideration the limits set by the Beer-Lambert law and limit of detection for the spectrophotometer. NMR was used on samples to confirm ligand attachment to the gold nanoparticle. When the ligand is attached to the gold nanoparticle its proton signal broadens and proton signals close to the gold-sulfur bond shift slightly downfield.¹⁴³ The signal broadening and ppm shift is due to the close proximity of the ligand to a diamagnetic layer at the surface of the gold nanoparticle.¹⁴⁴ If the ligands were in solution with the gold nanoparticle but not adsorbed, then the spectral peaks would be sharp and have no shift. Examples of this phenomenon are shown in NMR spectra of figure 4.4, but the actual spectra of the Lilly drug conjugates cannot be displayed as they may reveal relevant structural information about the drug.

PAGE is another qualitative approach to determine if drug has exchanged onto the gold nanoparticle. PAGE separates molecules based on charge and size. This separation occurs when an electric field is applied to the samples and the negatively charged particles move through a matrix of polymerized acrylamide. Large particles travel slower through the gel than small particles. Additionally, a highly negative particle travels fastest through the gel, so a decrease in negative charge would slow the migration of a particle. The Lilly drug as a positive charge, so gold nanoparticles travel slower through the gel when drug ligands are attached to it. If the drug was in solution and not attached to the gold nanoparticle there would not be a significant gel shift, because the drug alone and would not migrate into the gel due to its positive charge. The drug molecule (740 g/mole) is larger

than molecules that comprise the base monolayer, GSH (307 g/mole) or *p*MBA (154 g/mole); so attached Lilly drug ligands may increase the hydrodynamic radius of the gold drug conjugate and slow migration in the gel. A caveat of this characterization method is that the particles may have aggregated or etched during the exchange; thus, it is imperative to follow PAGE with TEM analysis of the particles. TEM will confirm that the diameter of the gold nanoparticle has not changed in diameter post-exchange. Figure 4.9 exhibits the gel shift created when the drug is exchanged onto the surface of the gold nanoparticle. PAGE was

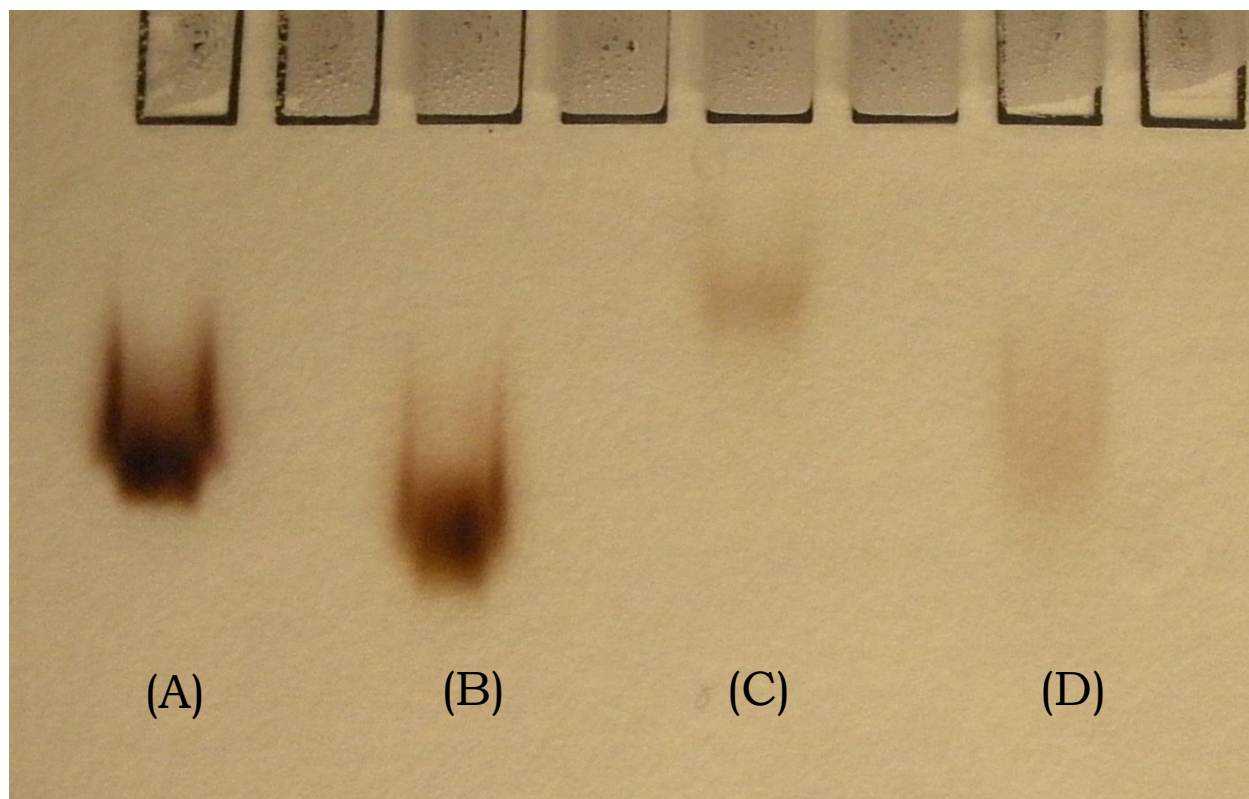


Figure 4.9. A polyacrylamide gel demonstrating the differences in migration, which is dependent on the gold nanoparticle monolayer composition. Gold nanoparticle sample in lane (A) is *p*-MBA gold nanoparticles and lane (C) are *p*-MBA gold nanoparticles with drug conjugated to their surface. Sample in lane (B) are GSH-coated gold nanoparticles and lane (D) are glutathione and drug gold conjugate. The gel is not stained in any way, the image shows actual gold nanoparticles visible as a group migrating through the gel.

followed by TEM of the nanoparticles shown in figure 4.10. Comparison of the exchange particles in the TEM images of figure 4.10 to the stock particles in figure 4.3 confirms that the diameter of the gold drug conjugate did not change due to the exchange.

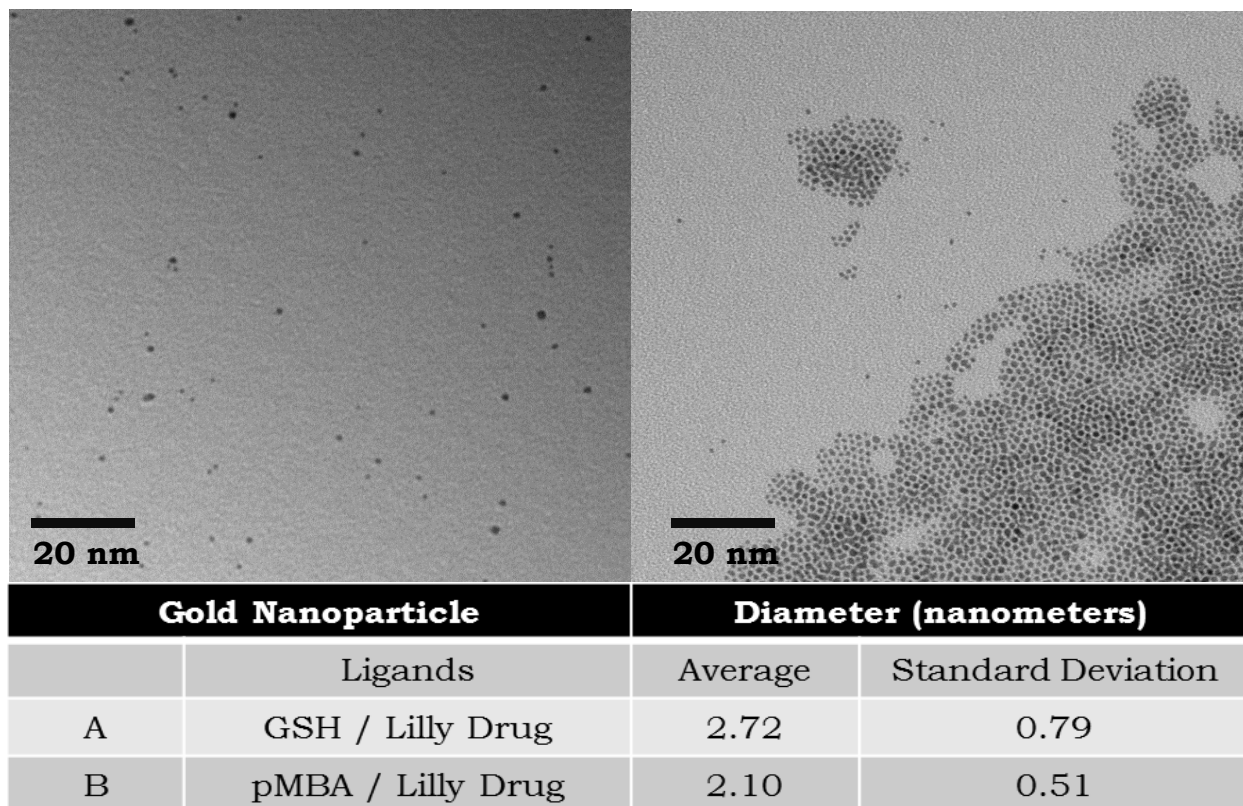


Figure 4.10. TEM images of gold nanoparticle conjugates. In image (A) are GSH drug gold conjugates and image (B) are *p*-MBA drug gold conjugates. Note the stock GSH and *p*-MBA utilized and their images can be referenced in Figure 3.3.

PAGE combined with TEM analysis confirms presence of drug on the gold nanoparticle surface.

The Lilly drug ligand remained intact after conjugation to the gold nanoparticle. The ligand was characterized after being etched from the gold drug

conjugate and then remaining ligands tested by HPLC and LC-MS. The particle was completely etched away by molar excess of small thiol, 200,000:1 *p*-MBA to one gold nanoparticle. Next, the *p*-MBA is selectively precipitated from the mixture by reducing the pH of the mixture to pH 3 with hydrochloric acid, and centrifugation at 1,000x RCF for 60 seconds. The supernatant containing the drug ligand was removed and neutralized to pH 7.0 with sodium hydroxide. The supernatant was then tested by LC-MS and by HPLC via a UV-Vis detector. The chromatograms and mass spectra are shown in appendices, A24-A26. The LC-MS results confirmed presence of a molecule at 740 g/mole. Unfortunately, the LC-MS experiment was run without a set of standards, so the results were solely qualitative. It was evident that whole drug molecule persisted through an exchange onto the gold nanoparticle, but it could not determine how much drug degraded or if any. To determine the possible degradation the etched particle drug solution was compared to the stock drug in an HPLC experiment. The drug was detected by a UV-Vis detector and the wavelengths were set at 268 nm, where the drug absorbs strongly. The chromatograms of the drug stock, and the etched gold drug conjugates displayed only one strong peak at approximately 6 minutes. If the drug had decomposed it would have appeared on the chromatogram at a time shorter than the 6 minutes, because the HPLC experiment separated molecules in solution by size and small molecules eluted from the column more quickly than large molecules.

4.3.6 Stability of Drug Gold Conjugates

Determination of the drug-gold conjugates stability in cell culture media and in simulated gastrointestinal conditions had to be completed before *in vitro* or *in*

in vivo testing. If the gold drug conjugates were unstable, then they would likely have little or highly variable efficacy. Eli Lilly researchers were performing *in vitro* assays and the gold nanoparticles needed to show stability in their mammalian cell growth media. The cell culture media assay was completed in 96-well plates with a minimum of 3 replicates and monitored by UV-Vis at 510 nm, where the 2.0 nm gold nanoparticles absorb light the most. Each well contained cell culture media at pH 7.4 with gold nanoparticles spiked into the solution. A change in absorbance indicates a change to the size of the gold nanoparticle, because the particles absorbance wavelength is related to surface plasmon resonance which is dependent on gold nanoparticle size and shape. Ideally, the absorbance of the gold nanoparticles at 510 nm would not change, which would indicate that the nanoparticles remain suspended in solution. If the nanoparticles aggregate the solution becomes clear and the absorbance decreases. The *p*-MBA based drug-gold nanoparticle conjugates had solubility issues in the cell growth media at a pH less than 10.0 and completely aggregated immediately when added to the wells. Since physiological conditions at a pH of 7.4 are required for this cell culture assay, the *p*-MBA particles were not analyzed further. Drug-gold conjugate with a base GSH monolayer demonstrated higher stability than the unconjugated gold nanoparticle, as shown in figure 4.11.

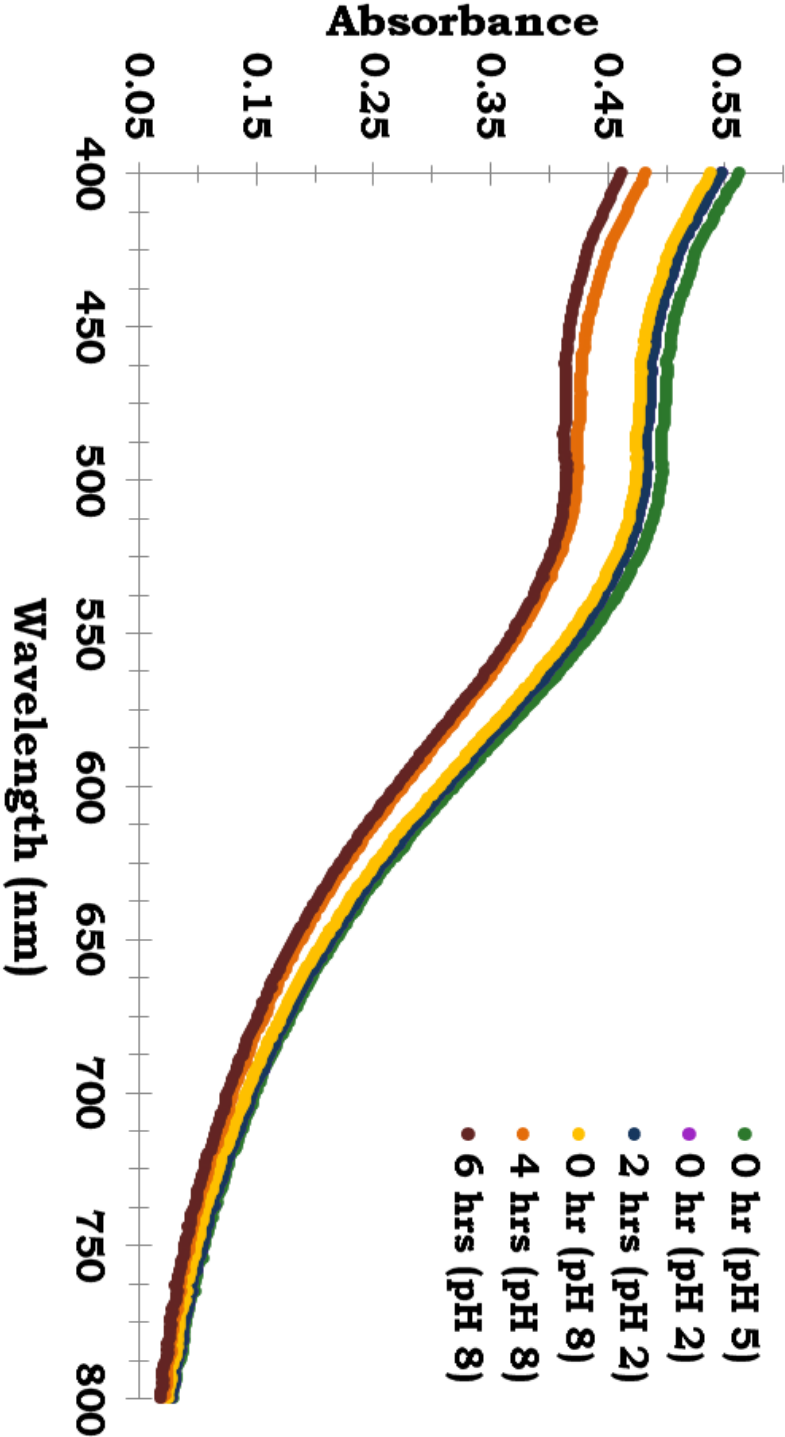


Figure 4.12. GI tract simulation study UV-Vis spectrum used to determine stability of the GSH drug gold conjugate in an environment similar to the human GI tract.

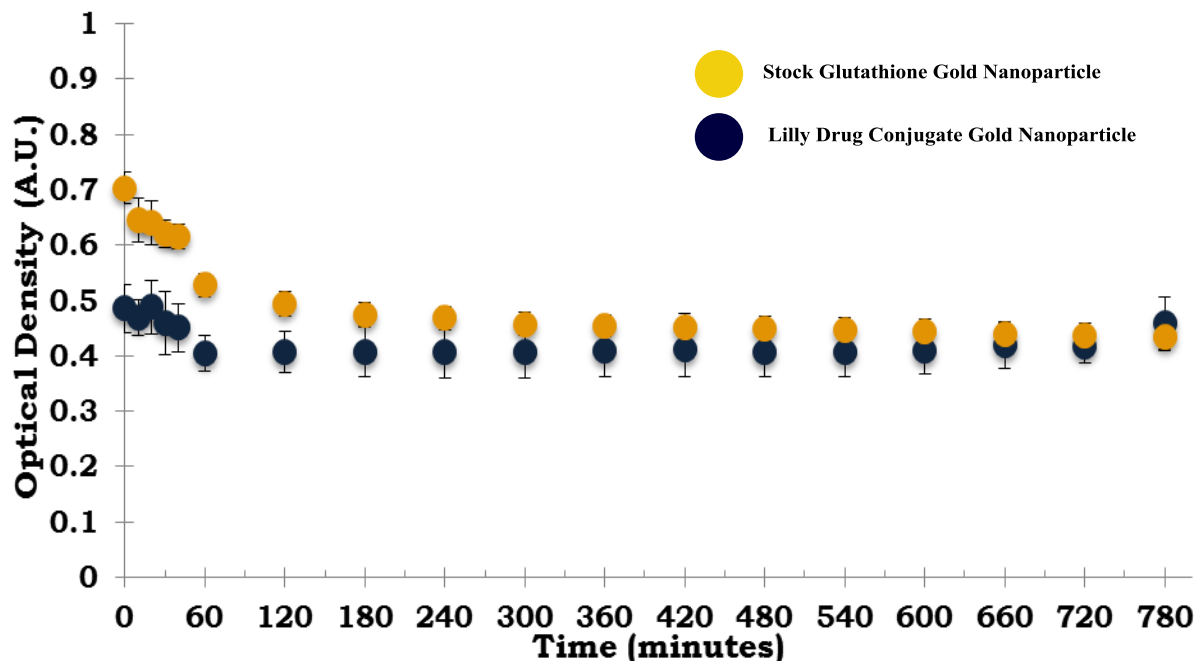


Figure 4.11. Cell Culture Media Assay that monitored of the absorbance at the surface plasmon resonance wavelength max at 510 nm of the 2.0 gold nanoparticles. Navy absorbance values are gold drug conjugate with a GSH base monolayer. Gold absorbance values are unconjugated stock GSH gold nanoparticles.

Similarly, the gastrointestinal tract stability assay displays stability of the drug-gold conjugate in comparison to the GSH base nanoparticle platform. The gastrointestinal stability assay varied the pH, length of time the nanoparticles reside at a specific pH, and consistent orbital shaking to simulate conditions of a human GI tract. Considering the possible variability of stomach and intestine transit time it was decided to go by 50% emptying time. To empty by 50%, the human stomach requires approximately 2.0 hours and the small intestines 3 hours.^{135,145} Overall, the Lilly drug-gold conjugates were robust despite facing harsh simulated conditions of the gastrointestinal tract or complex matrix of the cell growth media.

4.3.7 *In Vitro* assays with Drug Gold Conjugate

Proprietary *in vitro* mammalian cell assays were run using the Lilly drug-gold conjugates. Results from these assays revealed a specific GSH based drug-gold conjugate that had a promising EC₅₀, but the value was not equivalent to the free drug molecule. If possible, to improve the sensitivity to the drug the PEG linker length could have been increased in length. There could have been the possibility that greater distance between the drug and the gold nanoparticle would allow the drug more mobility to reach its target. Despite a literature search, it seemed uncertain whether a GSH based nanoparticles itself could lower the drug's effectiveness *in vitro*. Albeit the drug-gold nanoparticle lacked the same effectiveness to the parent drug molecule, the results were promising enough for the team to move forward with initial animal studies.

4.3.8 *In vivo* studies With the Drug Gold Conjugate

Animal studies were conducted on mice in triplicate by Eli Lilly researchers, then serum and organ samples were collected and sent to me the University of Colorado. The organ samples were digested in nitric acid, boiled down, and resuspended in 5.0 mL of ultra-pure water. The serum samples were diluted by 1:1000 in water. Then, both the prepped serum and organ samples were submitted for elemental gold analysis by ICP-MS and analyzed samples are

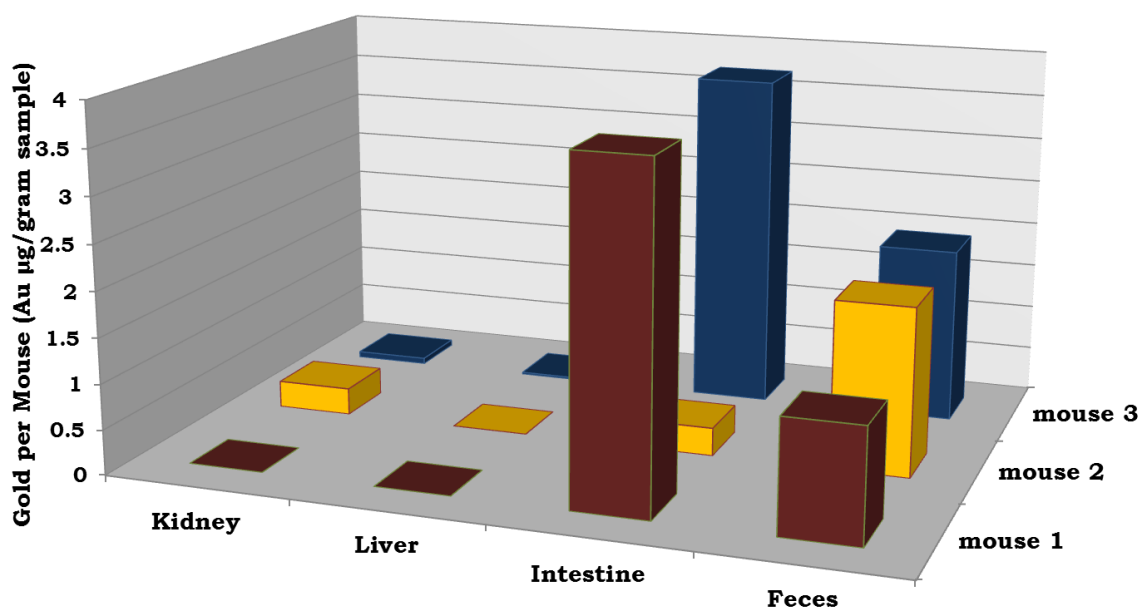


Figure 4.13. Biodistribution data of organs and excrement of three mice administered one 200 μL dose of 60 μM gold nanoparticle conjugate. Note the intestine samples of mouse 2 is only a fraction of the total sample due

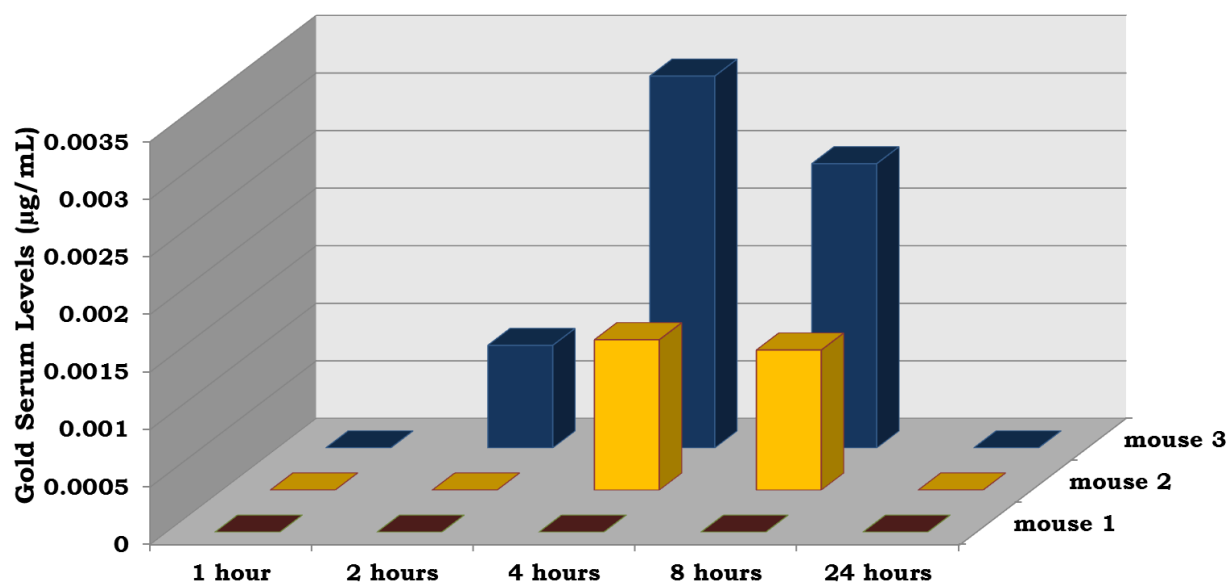


Figure 4.14. Time course of gold concentration in serum after 3 mice were treated with a single dose of the drug gold conjugate. Note the serum gold concentrations are several orders of magnitude lower than the pegylated gold conjugates of the early bioavailability study in chapter 3.

displayed in figures 4.13 and 4.14. Unlike the GSH base nanoparticles, the drug-gold conjugates were absorbed by through the GI tract; however, the drug-gold conjugates were absorbed far less than free parent drug. Levels of gold in the intestine were much higher than samples collected and measured for the gold nanoparticles tested in the above bioavailability study, which means the drug was in the region that it targets. Note, due to a processing issue the intestine in mouse 2 is representative of approximately 10% of the total sample. The marginal absorption of the drug conjugates may be due to the PEG linker of the modified Lilly drug molecule. Based on the bioavailability data shown above, absorption of the drug-gold nanoparticle could be further minimized by increasing the PEG spacer length of the modified drug.

4.4 Conclusions and Future Directions

The ease with which gold nanoparticles may be synthesized and modified with a plurality of ligands makes them attractive candidates as imaging agents, therapeutics, and therapeutic delivery systems. The most attractive route for administering drugs and diagnostic agents is orally. The ability to modify gold nanoparticles to facilitate their gastrointestinal absorption could create new opportunities in medicine, particularly for diseases that require frequent administrations and prolonged treatments, and in regions of the world where other forms of administration are impractical and engender a significant health risk (*e.g.*, intravenous injection). The gold nanoparticle antibiotics discovered in our lab are one example where oral bioavailability will be important if a translation to the clinic is to be made. It is interesting to consider further the possibility that therapeutically viable drugs that have been shelved due to poor oral bioavailability

might be rescued via conjugation to PEG4-modified gold nanoparticles. It is equally important to not overlook the observation that certain PEGs and small molecules can prevent nanoparticle absorption in the GI tract. Many important disease targets exist in the small and large intestines, and confining a drug to the GI tract can lower the therapeutic drug dose required and prevent side effects that occur upon systemic circulation. Although we have yet to investigate whether PEG4 can be combined onto gold with other small molecules without compromising GI absorption efficiency, the results presented here suggest that 2.0 nm diameter gold nanoparticles containing PEG4 may be a useful platform for the synthesis of orally bioavailable nanoparticle therapeutics, while nanoparticles modified with *p*MBA, GSH, or PEG24 may be suitable for therapeutics designed for intestinal targets. From the results of these studies, we approached an antimicrobial gold nanoparticle developed in the Feldheim lab to create an *in vivo* model for it.

4.5 Methods and Materials

4.5.1 Synthesis of gold nanoparticles

GSH-coated gold nanoparticles and *p*MBA-coated gold nanoparticles were synthesized according to our previous publications.^{16, 20} A solution of 20 mM HAuCl₄ (Strem, Newburyport, Massachusetts) dissolved in 20 mL of methanol was combined with either 16 mL of 85.0 mM GSH in ultrapure water (Sigma Aldrich, St. Louis, Missouri), or 85.0 mM *p*MBA dissolved in pH 12 ultrapure water. Gold mixtures were allowed to equilibrate for 15 minutes while stirring. The solutions (0.40 mmoles of Au³⁺) were diluted to a final Au³⁺ concentration of 0.55 mM with the addition of 202 mL ultrapure water and 186 mL methanol. The Au³⁺

was reduced with 7.2 mL of a 0.25 mM aqueous sodium borohydride (Sigma Aldrich) solution. The reduction was allowed to proceed for 24 hours at room temperature with constant stirring. Gold nanoparticles were precipitated with the addition of 120 mmol of NaCl in 720 mL methanol followed by centrifugation at 3200 RCF for 5 minutes. Precipitated nanoparticles were reconstituted in water. The concentration was measured by UV-visible spectroscopy using the extinction coefficient of $400,000 \text{ M}^{-1}\text{cm}^{-1}$ at 510 nm. The diameter of the *p*MBA-Au nanoparticles was $1.7 \pm 0.40 \text{ nm}$ as determined by transmission electron microscopy (TEM). This size is similar to *p*MBA-Au nanoparticles characterized by x-ray crystallography to have a molecular formula of $\text{Au}_{144}(\text{pMBA})_{60}$.¹⁴⁶ The diameter of the GSH-Au nanoparticles was $2.0 \text{ nm} \pm 0.60 \text{ nm}$.

4.5.2 Place-exchange of PEG onto glutathione gold nanoparticles

Stock solutions of the cyclic disulfide-terminated Polyethylene Glycols (PEGs), from Quanta Biodesign, were prepared in either water (PEG4-Neutral, and PEG24-Neutral) or dimethyl sulfoxide (PEG4-Acid, PEG12-Neutral, PEG12-Acid). To a 10 μM solution of GSH-coated gold nanoparticles in Milli-Q water (18 m Ω), an aliquot of PEG stock solution is added to a final concentration of 1mM. Exchange was replicated in 20 individual tubes each with a total volume of 4 mL. Solutions were placed on a shaker at 19°C and allowed to mix for 24 hours. Particles were precipitated by adding 2.0 mL of a 4.0 M NaCl solution followed by centrifugation at 3200 RCF for 15 minutes. Precipitated particles were allowed to air dry for 24 hours. Particles were then suspended in water, all 20 tubes combined, washed three times over a 30K MWCO amicon filter. The final concentration was determined by UV-visible spectroscopy as described above.

4.5.3 Place-exchange of Lilly Drug onto 2.0 gold nanoparticles

Stock solutions of the drug were prepared in dimethyl sulfoxide. To a 10 μ M solution of GSH-coated or *p*-MBA gold nanoparticles in Milli-Q water (18 m Ω), an aliquot of PEG stock solution is added to a final concentration of 200-400x the concentration of the gold nanoparticles. Exchange was replicated in 15 mL individual tubes each with a total volume of 4 mL. Solutions were placed on a rotisserie at 25°C and allowed to mix for 24 hours. Particles were concentrated 10x with 10 kDa MWCO amicon by centrifugation at 3200 RCF for 15 minutes and then dialyzed against 1x phosphate-buffered saline pH 7.4 for 48 hours with buffer changes every 4 hours. Particles were then characterized and quantitated by NMR, PAGE, HPLC, and UV-Vis.

4.5.3.1 UV-Vis characterization

The spectrum for the Lilly drug was recorded in triplicate. The drug had its strongest peak at 268 nm and no absorbance at 510 nm. Serial dilutions of the drug were made and their spectra recorded in order to create a calibration curve for the drug, which can be seen in appendix A27. The spectra of the stock gold nanoparticles were recorded in triplicate, and the ratio of absorbance at 510nm/268nm was calculated to be 1.83. The gold nanoparticle had a surface plasmon peak at 510 nm, and also absorbed at 268 nm. For each gold drug conjugate the absorbance at the wavelength of 510 nm was recorded, and then concentration of total gold nanoparticle and theoretical absorbance was calculated for the base gold nanoparticle at 268 nm. The observed absorbance at 268 nm of the gold drug conjugate was subtracted from the theoretical absorbance. The subsequent value was inputted into the calibration curve to determine the drug

concentration. The ratio of drug ligand to nanoparticle was calculated by dividing the calculated concentration of drug by nanoparticle.

4.5.4 Gold Nanoparticle Stability Assay in Cell Culture Media

Into a NUNC 96-well flat bottom plate cell culture media, Gibco Dulbecco's Modified Eagle Medium (D-Glucose 4.5g/L, no L-glutamine, no sodium pyruvate, no calcium chloride, no dye), Reference #21068-028 500 mL, was distributed by 300 μ L of per well with 5 repeats per the blank, no gold nanoparticle control, and experimental. 3.0 μ L of gold nanoparticles was added per well as to achieve an absorbance less than 1.0 O.D. Each well was pipette mixed and the zero time point taken by UV-Vis. Further time points were taken every 10 minutes immediately after being rotary mixed by the Omega 96-well plate UV-Vis reader.

4.5.5 Nuclear Magnetic Resonance spectroscopy (NMR)

NMR was used to assess the extent of ligand substitution. The gold nanoparticle samples were analyzed by ^1H NMR on a 500 MHz Varian Inova spectrometer in a solution of deuterium oxide/water with a water suppression program. For comparison, pure ligands were suspended in a mixture of deuterium oxide/water for all PEG and small molecules except for PEG12N, which was in a mixture of 90% D_2O :10% DMSO. A gradient COSY was run on both the GSH ligand and GSH coated nanoparticle to show correlative cross peaks of J-coupled signals. All spectra can be found either in figure 4.4 or within the appendices, A16-A23.

4.5.6 Transmission Electron Microscopy (TEM)

TEM grids were prepared by placing a drop of the gold nanoparticles on a carbon film-covered copper mesh grid for a minute and then excess solution was

wicked away with a paper filter. Grids were then allowed to air dry for 45 min before being imaged by TEM. The subsequent TEM images were analyzed by Image-J to determine the size distribution of the gold nanoparticle cores. A minimum of 100 particles were measured before analysis of size distribution.

Samples of urine were concentrated of 30 kDa MWCO amicons and washed three times with 400 μ L volumes of milli-Q water. Then 5 μ L of the resultant sample was applied to a copper grid and the excess solution wicked away. Due to excess salt the grids were rinsed twice with ultrapure water, by applying 10 μ L of milli-Q water, wicking the solution away, and allowing the grid to dry.

4.5.7 Animal Models

Animals were housed at the Keck Facility, a University of Colorado Division of Animal Care (DAC) facility, fully certified by the Association for Assessment and Accreditation of Laboratory Animal Care (AALAC). Animals were housed under the full supervision of the full-time veterinarian and staff. All procedures performed were previously approved by the University of Colorado's Institutional Animal Care and Use Committee (IACUC). Balb/c, 5-6 week, 15-16 gram, female mice were purchased from Harlan Laboratories. Nanoparticle formulations were prepared in Milli-Q water (n = 5 mice per formulation). Plastic oral gavage needles (20 gauge, 3.8mm length) were purchased from Instech Soloman. A 60 μ M or 120 μ M concentration in 200 μ L volume of each nanoparticle formulation was administered to five individual mice by oral gavage (45 mice total). Blood was drawn via submandibular bleeding techniques,²⁴ in compliance with our protocol and bleeding guidelines for mL/kg body weight per week.¹⁴⁷ Urine was collected on cellophane with precautions taken to avoid fecal contamination.¹⁴⁸ Feces were also

collected separately on cellophane. Mice were euthanized at 24 hours by carbon dioxide asphyxiation followed by cervical dislocation. Three mice were sampled from each group for biodistribution analysis.

4.5.8 Sample Collection and Preparation

Blood, urine, and tissue samples were prepared as described in Simpson et al. with no modifications or exceptions.²⁰ Fecal samples were prepared by digestion in 500 μ L of 70% Hydrochloric Acid Optima overnight and the emulsion was diluted with ultrapure water down to 7% HCl.

4.5.9 Inductively Coupled Plasma-Mass Spectrometry (ICP-MS) analysis

Analysis of gold content in biological samples was performed using a Perkin Elmer SCIEX ICP-MS (Model # Elan DRC-e, Vernon Hills, Illinois) at the University of Colorado Laboratory for Environmental and Geological Sciences (LEGS). Statistical analysis of samples was performed involving the student T-test (95% confidence level) with units in μ g/mL. The detection limit of the instrument was 0.02 ppb (0.02 ng Au/mL) sample.

4.5.10 Aggregation study using relative stomach and intestinal pH

In order to determine if the gold nanoparticles could withstand the pH and temperature of the mouse and human gastrointestinal system—37 °C and pH as low as 2 and as high 8—samples of each gold nanoparticle formulation were tested for stability in aqueous solutions with pH ranging from 2 to 8.¹⁴⁹ This was accomplished by adjusting the pH of 20 μ M solutions of gold nanoparticles to pH 2 with HCl, heating to 37 °C, and shaking for 2 hrs. The samples were monitored by UV-visible spectroscopy to determine the extent of aggregation. The samples were then adjusted to pH 8 to simulate conditions with the intestine, and

subsequently warmed to 37 °C and shaken for an additional 4 hours. The results were then compared to a set of controls at pH 5 that did not undergo any pH adjustments.

4.5.11 Polyacrylamide Gel Electrophoresis

Pre-made 15% polyacrylamide gels were purchased from Bio-rad. Each gold nanoparticle sample was prepared by loading 2 μL of $\sim 700 \mu\text{M}$ gold nanoparticle with 6 μL of 50% glycerol. Samples were loaded into the wells of the gel. The electric field was applied with 150 Volts and 2 Watts of power for a total of 40 minutes. Gold nanoparticle migration was visible by eye and imaged with a camera.

Chapter 5: Toxicity and Bioavailability of Potential Gold Nanoparticle Antibiotics *in vivo*

5.1 Introduction

Emerging infectious diseases are a perpetual problem world-wide as new multi-drug resistant strains of bacteria develop and spread. These new bacterial strains create a clamor for better therapeutics as existing antibiotics lose efficacy.¹⁵⁰ The CDC has listed current national threat levels corresponding to emerging infectious pathogens like Methicillin Resistant *Staphylococcus Aureus* (MRSA), drug resistant Tuberculosis (MDR-TB and XDR-TB), and *Clostridium difficile*.⁸ Many of the CDC listed pathogens have been categorized under urgent or serious threat levels, which emphasizes the need for new antibiotics.⁸ As a solution some research groups have been investigating the use of ligand capped gold nanoparticles as possible antimicrobials, including the Feldheim group. In this project, the gold nanoparticle antimicrobial LAL-32 has been investigated in a murine model to determine its toxicity and bioavailability *in vivo*.

5.1.1 Small Variable Ligand Display Antimicrobials

In the combinatorial library approach mentioned in chapter 1, the Feldheim group developed a gold nanoparticle system for use against drug resistant pathogens called Small Ligand

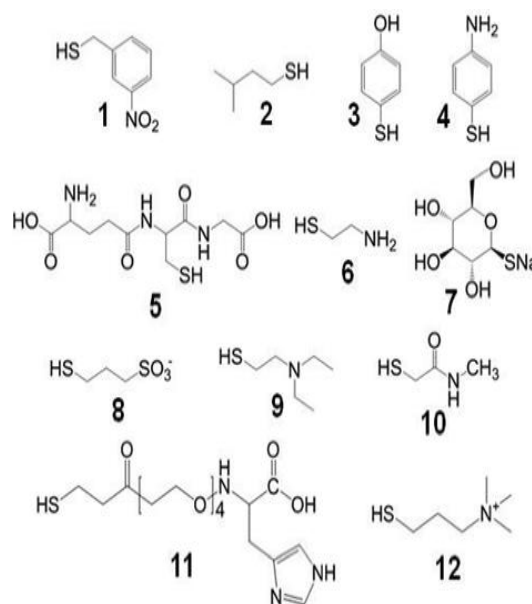


Figure 5.1. Core library of thiols used to create mixed ligand monolayers on the gold

Variable Display (SMVLD).⁴⁶ The SMVLD method utilizes *para*-mercaptobenzoic acid (pMBA) modified gold nanoparticles as the base material. Specific ratios of small molecule thiol ligands are then exchanged onto the base particles to form mixed monolayer conjugates, often compromised of 2-4 different thiols.⁴⁷ Figure 5.1, shows the core library of thiols used to make the variable ligand gold conjugates. From the core library of thiol ligands, a 120 gold conjugate library was created and each conjugate was tested to determine its ability to inhibit or kill pathogens like *E. coli*, *K. pneumonia*, *S. Aureus*, *M. smegmatis*, and etc.^{46,48,49}

A gold conjugate's ability to inhibit or kill bacteria is determined by the minimum inhibitory concentration (MIC_{99.9}) of gold nanoparticles necessary to retard bacterial growth by 99.9%.¹⁵¹ Some of the SMVLD sourced gold conjugates have antimicrobial properties on par with small molecule antibiotics in regards to their potency, stability, and *in vitro* toxicity.^{46-48,152} Gold conjugates have MICs

Table 5.1. Gold Conjugates and their MIC_{99.9} values for specific bacteria

Conjugate ID	Thiol ligands	Inhibited Bacteria	IC _{99.9} (μM)
LAL-6	1, 2, 8	<i>S. Aureus</i> (ATCC 29213)	10.0
LAL-32	5, 6, 8	<i>E. coli</i> (BAA-199)	0.156
LAL-32	5, 6, 8, EG	<i>E. coli</i> (ATCC 25922)	0.25
LAL-32	5, 6, 8	<i>K. pneumoniae</i> (BAA-2146)	0.625
LAL-3346	6, 8, 9	<i>M. smegmatis</i>	6.0
LAL-52	5, 6, 11	<i>K. pneumoniae</i> (BAA-2146)	1.25

ranging from 0.25 - 25.0 nM (see table 5.1). Comparatively the common antibiotics, Ciprofloxacin and Imipenem are potent against multiple bacterial

strains, with MICs ranging from 7.0 nM-42.0 μ M.¹⁵² Similar to other liquid antibiotics, aqueous solutions of gold antimicrobials are stable for weeks to months.¹⁵³ In mammalian cell toxicity *in vitro* many of the gold conjugates have therapeutic indices above the narrow therapeutic standard, which means they are potent antimicrobials that have low toxicity to mammalian cells. All common antibiotics have therapeutic indices greater than the narrow therapeutic standard^{154,155} Under section 320.33(c) of Code of Federal Register 21, the Food and Drug Administration defines a drug product as having a narrow therapeutic ratio if there is less than a 2-fold difference between the median lethal dose and effective dose.¹⁵⁶ In other words, it is the difference of how effective a drug is compared to lethality. The gold conjugates isolated from the SMVLD method encompass positive attributes on par with antibiotics.

The LAL-32 conjugate may be the most promising antibiotic candidate. LAL-32 incorporates 3 main ligands, see figure 5.2. It has been shown to be potent against multiple strains of bacteria (see table 5.1) and a therapeutic index of 400, which is well above the narrow therapeutic ratio. Most intriguing, LAL-32 has low susceptibility to drug resistance; in fact data indicated that *E.coli* failed to gain resistance to LAL-32 during a 50 day resistance assay. These qualities make LAL-32 an excellent candidate as an antimicrobial in general, but further studies needed to be done to determine its *in vivo* toxicity, biodistribution, and to maximize its delivery to the body.

5.2 Results and Discussion

5.2.1 Initial *in vivo* Toxicity and Biodistribution of LAL-32

The following experiment details the *in vivo* toxicity, clearance, biodistribution of LAL-32 in a murine model. The initial toxicity was tested in a 24 hour time course as part of humane animal husbandry. The dosage administered was a single 200 μL intraperitoneal injection at a concentration of 10.0 μM and 60.0 μM . The initial dosage of LAL-32 to be administered was determined from a preliminary toxicity study, which mice were administered 2.0 nm gold nanoparticles composed of a glutathione (GSh) surface monolayer.¹³⁶ GSH is one of the three ligands incorporated into the LAL-32 surface monolayer, see figure 5.2. Drug formulations diffuse from the injection site based off of size and charge.^{157,158} Although, the GSH and LAL-32 nanoparticles have the equivalent size dispersity, they may diffuse at different rates into tissue. Despite differing ligand composition between the nanoparticles, basing the initial dosage on GSH remains a good estimation method.

Figure 5.3, shows clearance and biodistribution data for vital organs, urine, and blood data of all concentrations of LAL-32 utilized for the initial study. 24 hours post-administration of LAL-32, it was found that the mice tolerated the 10.0

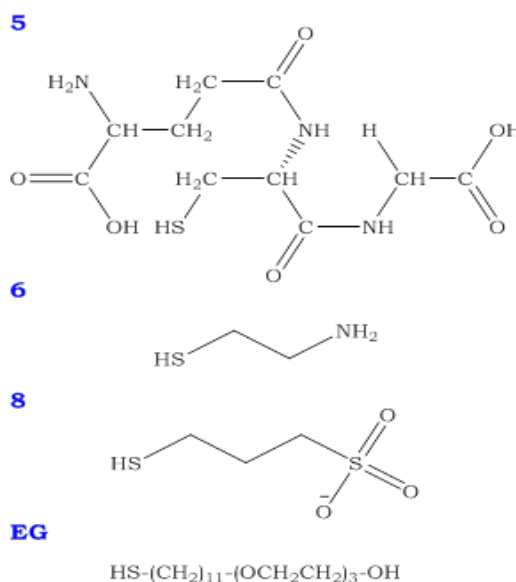


Figure 5.2. Ligands of LAL-32 are glutathione (5), cystamine (6), and 3-mercapto-1-propanesulfonate (8). and LAL-32EG also includes ligand EG.

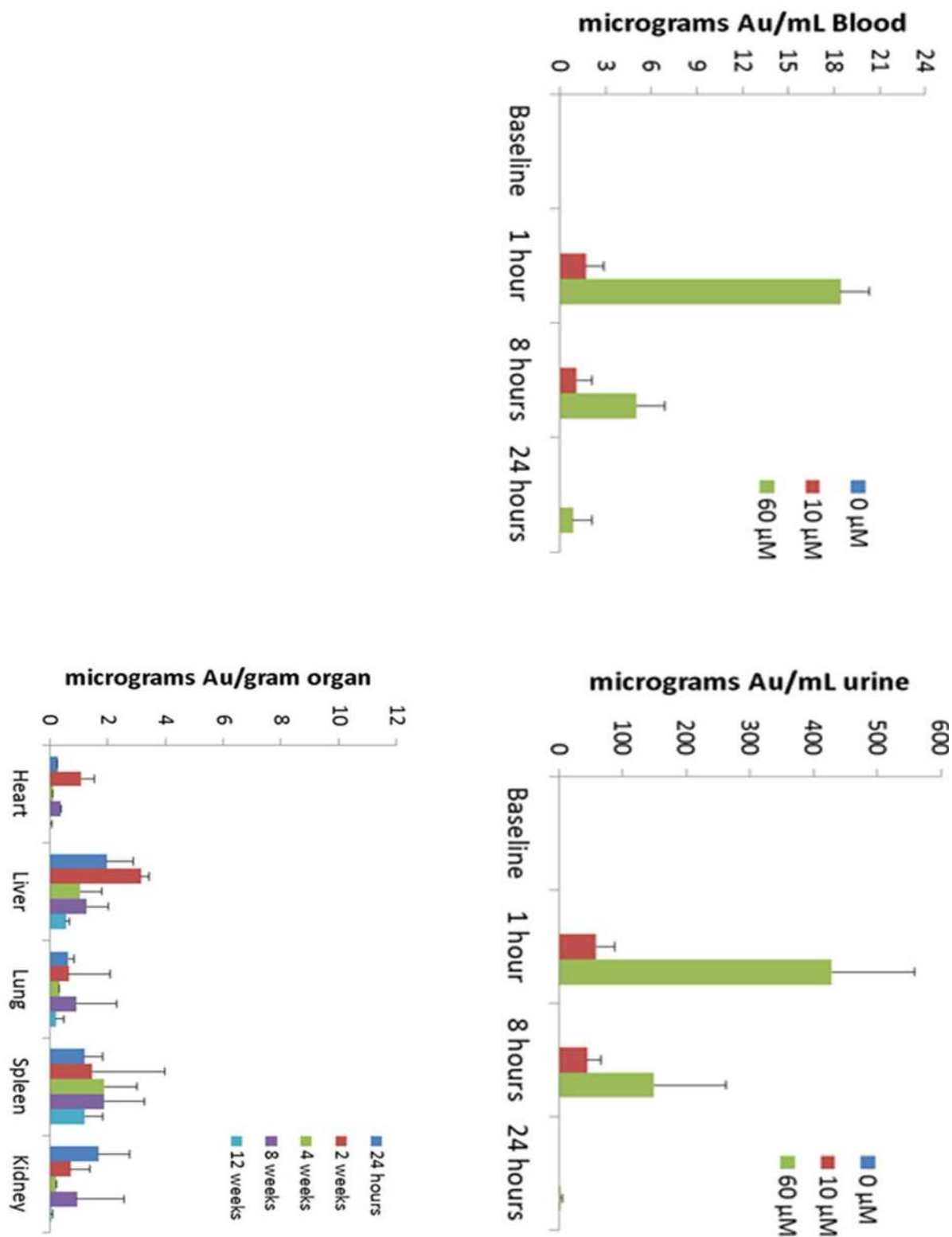


Figure 5.3. Biodistribution data of blood, urine, and organ data. The 10 μM concentration has biodistribution data from 24 hour through 12 weeks. However, the 60 μM concentration has organ data for only the first 24 hours.

μM dose well. However, the mice given a higher dose of $60.0 \mu\text{M}$ showed visible distress and excreted abnormal appearing dark brown urine; in consequence, all mice treated with a $60.0 \mu\text{M}$ dose were euthanized according to humane practices prescribed in the IRB protocol. The abnormally dark urine could indicate either rapid particle clearance or blood in the urine. Blood in the urine would point to serious renal toxicity. Kidney samples were sent to Histotox Labs in Boulder for histology and pathology analysis to determine renal damage. Figure 5.4 displays the confocal microscopy images of

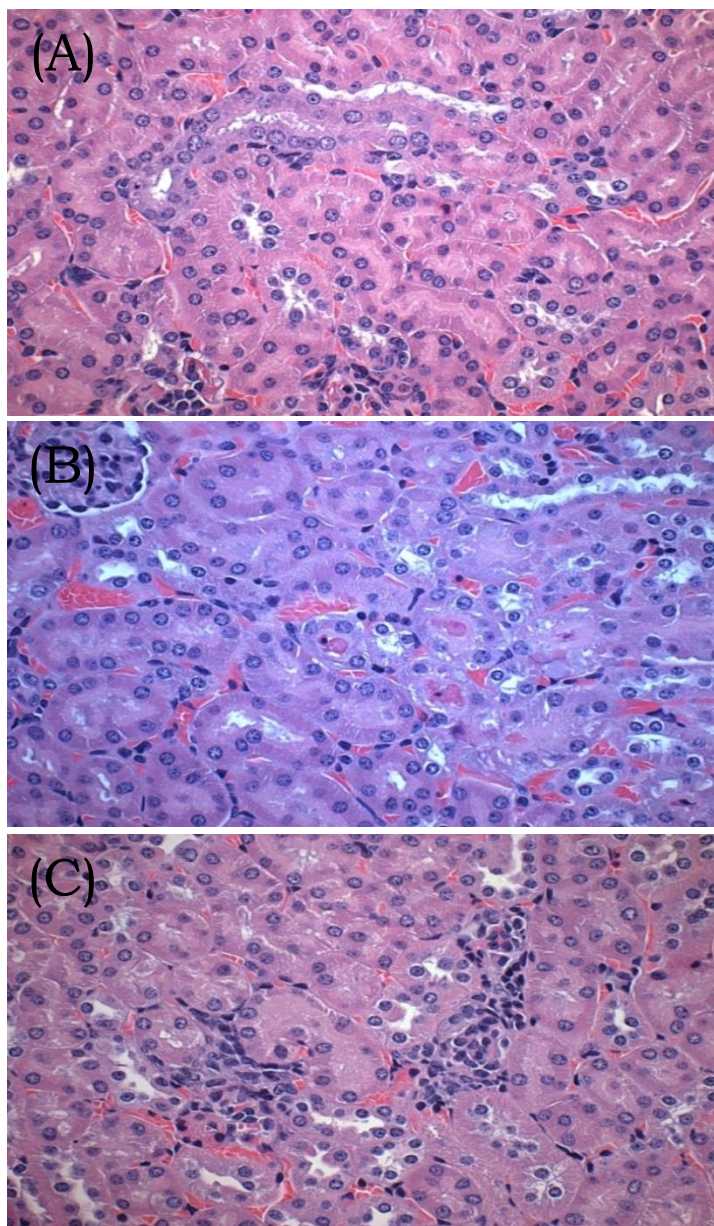


Figure 5.4. Microscopy images of mouse renal samples: (A) control mouse administered $0 \mu\text{M}$ gold nanoparticle solution of buffer only, (B) mouse administered $10 \mu\text{M}$ dose of LAL-32, (C) mouse administered $60 \mu\text{M}$ dose of LAL-32.

the kidneys for the three dosages of gold conjugates administered to the mice. Histology of the kidneys conducted by Laura Healy DVM at Histotox determined

that the gold nanoparticles did not induce any apparent renal toxicity for any gold nanoparticles samples administered to the mice. All findings were well within normal background including: basophilic tubules as they are typically a regenerative response with increased nuclear density and basophilic cytoplasm, the minimal evidence of tubule epithelial cell degeneration is considered normal epithelial turnover, and minimal lymphocyte infiltrates are normal in the kidney. From the clearance, biodistribution, and toxicity results it was determined that the clearance rate of the gold nanoparticles did not cause any apparent toxicity to the mice.

5.2.2 Modifying LAL-32 with Polyethylene glycol

The next step of the study aimed to increase LAL-32's half-life in the body and in to reduce stress on the mice. To obviate the problem, a small amount of a thiolated polyethylene glycol (EG), $\text{HS}-(\text{CH}_2)_{11}-(\text{OCH}_2\text{CH}_2)_3-\text{OH}$, was incorporated into the LAL-32 monolayer in a 5:1 ratio of PEG to the LAL-32 gold conjugate. Conjugation of PEG to a drug carrier can increase circulation time by slowing diffusion rates from injection sites.¹⁵⁹⁻¹⁶¹ Pegylation of the particle is better than adding PEG to the injection formulation, because it diffuses with the particle. It is possible that when PEG is used as part of the drug formulation, it will diffuse out of the tissue quicker than the drug. This could destabilize the drug and cause it to precipitate in the tissue.¹⁵⁸ Incorporation of an undecane chain linker between the thiol and PEG ligand could increase circulation half-life of the gold conjugate, based on research showing that longer alkane chains on PEG can enhance circulation half-life in liposomes.¹⁶² Most importantly, the ratio of five PEGs to one LAL-32 nanoparticle was utilized to prevent the PEG from monopolizing more than

10% of the monolayer surface, the threshold level in which the LAL-32 particles began losing antimicrobial activity.¹⁶³ The newly modified conjugate was labeled LAL-32EG, and *in vitro* tests showed equivalent potency to *E. coli* and lack of toxicity for mammalian cells equivalent to LAL-32. The experiment moved forward, and mice were administered a single intraperitoneal LAL-32EG dosage of 200 μ L at 60 μ M

It was found that the mice could safely tolerate the 60 μ M dosage

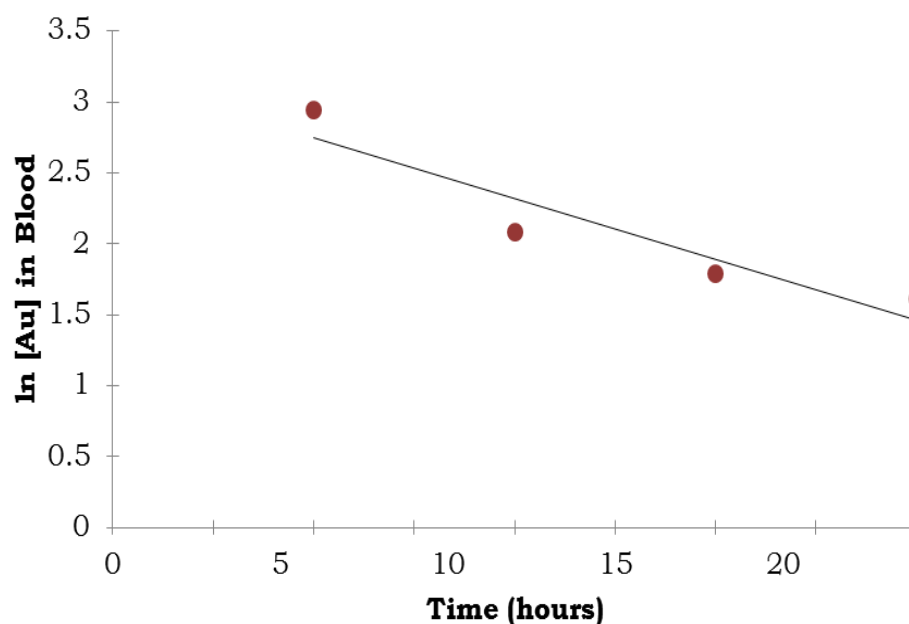


Figure 5.6 Blood half-life graph for 60 μ M injection of LAL-32EG gold conjugate.

administered of the LAL-32EG gold conjugate. As shown in the data of the ICP-MS gold elemental analysis of Figure 5.7, the LAL-32EG nanoparticles have slower blood and urine clearance, which could reduce stress on the mice. The gold blood circulation half-life was estimated to be 7.4 ± 3.0 hours using a first-order kinetics

and 50% confidence limit model as shown in Figure 5.7. Pathology results of LAL-32EG confirmed the particles did not cause renal toxicity.

Figure 5.8 displays the gold ICP-MS results from main bodily organs. When comparing LAL-32 and LAL-32EG biodistribution, the pegylated version has lower

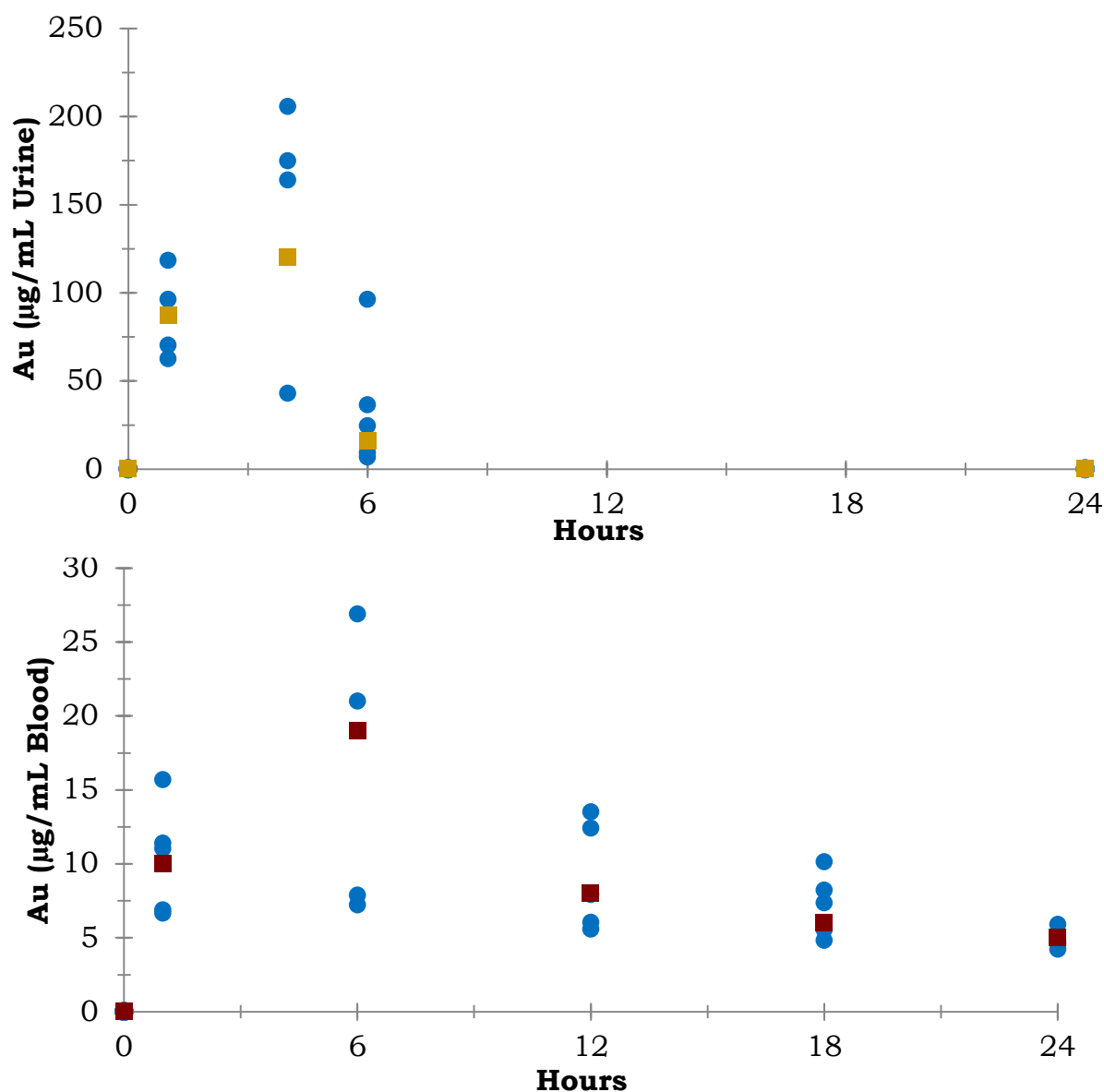


Figure 5.7. Urine and Blood clearance of LAL-32EG from mice during a 24-hour time period. Blue indicates individual data values, and square points indicate the average gold concentration per time period.

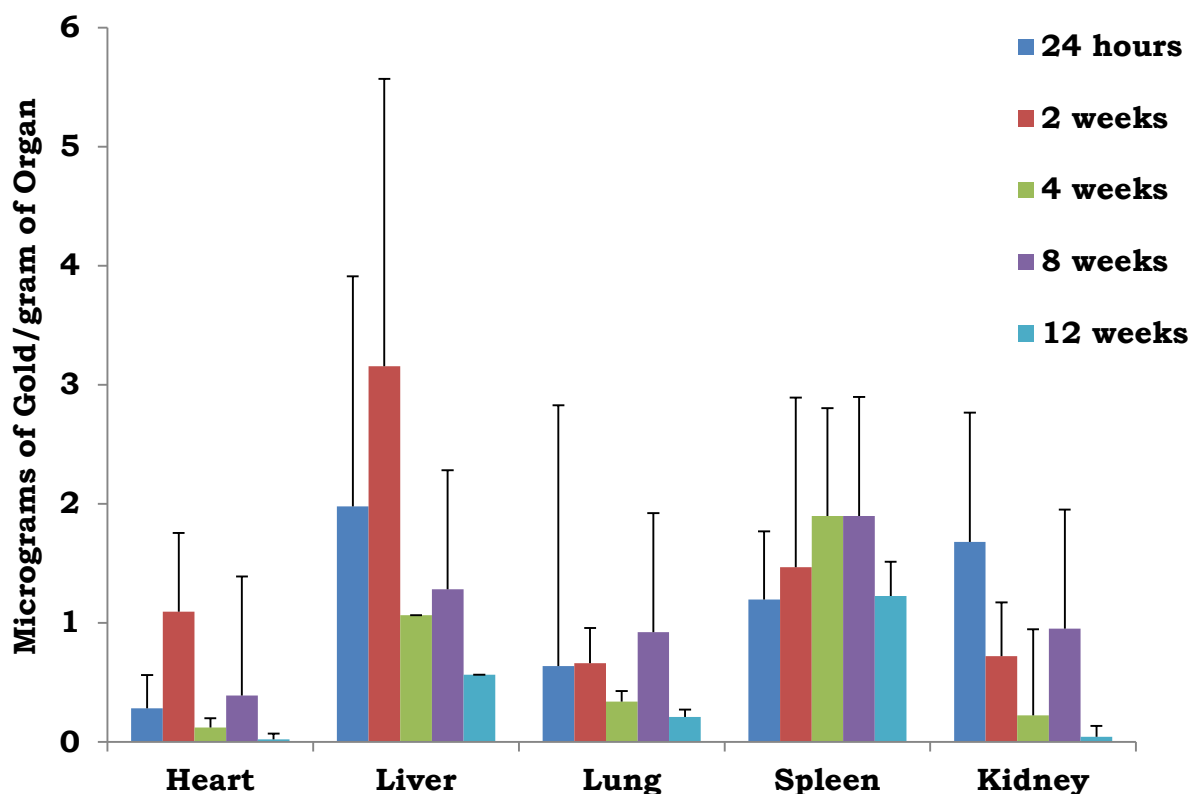


Figure 5.8. Organ distribution data for a 60 μ M injection of LAL-32EG from 24 hours through 12 weeks.

initial concentration at 24 hours, which may be due to the particles slowly diffusing from the intraperitoneal cavity into the body. The particles require an extensive amount of time to clear the organs. Unlike LAL-32, the pegylated version of the conjugate had not completely cleared the body by 3 months time.

5.3 Conclusions & Discussion

Gold nanoparticles have the promise to being beneficial antibiotics. The benefit of the SMVLD antibiotics is the ability to tune the surface monolayers for inhibition of specific pathogens; possibly leaving other important microbiome residents safe. In this chapter, studies of LAL-32 have been carried into animal studies. The work here showed that it is possible to safely administer this

nanoparticle to mice without significant toxicity. The pegylation of LAL-32 slowed clearance of LAL-32EG from the body. Longer circulation time could translate to improved efficacy times *in vivo*. Next steps for LAL-32 should include testing in a disease model *in vivo* to determine what real life infection scenarios that the nanoparticles would have highest efficacy. Possible examples could include use in topical wound dressings or for gastrointestinal infections, as both would permit facile administration to a patient in large quantities. At the time of original research, it was difficult to determine how much of these gold conjugates could be available in the body via oral administration.

5.4 Methods and Materials

5.5.1 Synthesis of gold nanoparticles

para-mercaptobenzoic acid-capped gold nanoparticles (p-MBA-Au) were synthesized as previously described.⁴⁷ A solution of 11.1 mM HAuCl₄ (Sigma Aldrich), 37.8 mM p-mercaptobenzoic acid (p-MBA) (TCI-America), 178 mM NaOH in 55.6% (v/v) aqueous methanol was prepared and allowed to equilibrate for 24 hours with constant stirring. 50 mL of this solution (0.556 mmoles of Au³⁺) were diluted to a final Au³⁺ concentration of 0.48 mM with the addition of 260 mL methanol and 740 mL water. The Au³⁺ was reduced with the addition of 10 mL of 0.25 M NaBH₄ (Sigma Aldrich). The final methanol concentration was adjusted to 25.8% with the addition of 100 mL of water. The reduction of gold was allowed to proceed for 48 hours at room temperature with constant stirring. Gold nanoparticles were precipitated with the addition of 68 mmoles of NaCl and 500 mL of methanol (final methanol concentration of 47% v/v) followed by centrifugation at 3200 RCF for five minutes. The precipitated nanoparticles were

reconstituted in water. The concentration was measured by UV-visible spectroscopy, using the $\epsilon_{510\text{ nm}}$ of 409,440 M⁻¹cm⁻¹. Further, it was noted that the source of reagents for this synthesis is important to the preparation. Ensuring that reagents were not stored with other chemicals that could react or contaminate them was also critical. Transmission electron microscopy (TEM) was used to determine the average size of the particles.

5.5.2 Place exchange **reactions**

One-pot place exchange reactions were conducted with 7.4 μ M gold nanoparticles in 4 mL of 20 mM pH 9.5 sodium phosphate buffer. Feed ratios of thiols were as follows: thiols 5 and 8 were utilized in 33X molar excess of gold nanoparticles, while thiol 6 was utilized at 46X molar excess of gold nanoparticles. Thiol EG was utilized in 5X molar excess of gold. Stocks of thiols were 20 mM in water. Reactions were placed on a plate shaker and agitated for 24 hours at 19°C. The exchange product was harvested through the addition of 40 mmoles of NaCl and a volume of methanol equal to that of phosphate buffer and added salt. Reactions were centrifuged at 3200 RCF for 30 minutes. Precipitated nanoparticles were resuspended and precipitated with the addition of NaCl and methanol two times to remove excess unreacted thiol. Particles were allowed to dry to completion overnight at room temperature and resuspended in water and washed with water over a 10K MWCO amicon filter to remove excess salt and thiol. TEM was used to determine the size of the exchange product LAL-32. The size distribution was observed to increase slightly, with particles ranging in size from ca. 1.3 nm to 2.7 nm (size standard deviation of 0.4 nm vs. 0.2 for pMBA-Au). As the molar extinction coefficient for gold nanoparticles in this size regime does

not change considerably ($2.33 \times 10^5 \text{ M}^{-1}\text{cm}^{-1}$ and $1.29 \times 10^6 \text{ M}^{-1}\text{cm}^{-1}$ for 1.3 nm and 2.7 nm diameter gold nanoparticles),¹⁶⁴ the extinction coefficient reported above for 2.2 nm diameter particles was used to prepare solutions of LAL-32 for bacterial growth inhibition assays. UV-visible spectroscopy confirmed that the major product in the synthesis of LAL-32 consisted of particles with similar visible light extinction characteristics to the starting pMBA-Au nanoparticles. This experimental section is from Dr. Jamee Bresee.

5.5.3 Animal protocols

Animals were housed at the Keck Facility, a University of Colorado Division of Animal Care (DAC) facility, fully certified by the Association for Assessment and Accreditation of Laboratory Animal Care (AALAC). Animals were housed under the full supervision of the full-time veterinarian and staff. All procedures performed were previously approved by the University of Colorado's Institutional Animal Care and Use Committee (IACUC) under the IRB IACUC protocol 1110.01, approved on 11/2011. Balb/c, 5-6 week, 15-16 g, female mice were purchased from Harlan Laboratories. All animals were allowed 1 week for acclimation prior to experimentation. Nanoparticle formulations were prepared in Dulbecco's PBS ($n = 15$ mice per concentration of LAL-32; $n = 25$ mice per concentration for LAL-32EG). A $10 \mu\text{M}$ or $60 \mu\text{M}$ concentration in 200 mL volume of each nanoparticle formulation was administered to individual mice by intraperitoneal injection. Blood was drawn via submandibular bleeding techniques in compliance with our protocol and bleeding guidelines for mL/kg body weight per week. Urine was collected on cellophane with precautions taken to avoid fecal contamination. Mice were euthanized at 24 hours, 2 weeks, 4 weeks, 8 weeks and 12 weeks by carbon

dioxide asphyxiation followed by cervical dislocation. Five mice were sampled from each group for biodistribution analysis.

5.5.4 Inductively Coupled Plasma Mass Spectrometry (ICP-MS)

Fluid and tissue samples were prepared as follows a 20 μ L standard blood and 10 μ L urine samples were used due to limitations in fluid collection. The fluid sample was then added to a 5.0 mL solution of distilled water. Organ samples were excised, weighed, and digested in nitric acid (Optima grade, 70%). The samples were then heated to dryness, at which point the remnants were transferred to a solution of 5.0 mL distilled water. All samples were then analyzed in duplicate by ICP-MS for gold content using a standard calibration. A blank and three standards were used for calibration. Analyses of diluted fluid and tissue samples were performed on a Perkin Elmer SCIEX ICP-MS (Model # Elan DRC-e) at the University of Colorado Laboratory for Environmental and Geological Sciences (LEGS). Statistical analysis of samples was performed as described in Simpson et al. with no exceptions. The detection limit of the instrument was 0.02 ppb or .02 ng Au/mL sample.

BIBLIOGRAPHY

- (1) Daniel, T. M. The History of Tuberculosis. *Respir. Med.* **2006**, 100, 1862–1870.
- (2) Crawford, M. H. *The Origins of Native Americans: Evidence from Anthropological Genetics*; Cambridge University Press, 2001.
- (3) A Boire, N. Tuberculosis: From an Untreatable Disease in Antiquity to an Untreatable Disease in Modern Times? *J. Anc. Dis. Prev. Remedies* **2013**, 01, 1–11.
- (4) World Health Organization. *Global Tuberculosis Report 2014*; 2014.
- (5) Weinstein, L. Tuberculosis Diagnostics in 2015: Landscape, Priorities, Needs, and Prospects. *J. Infect. Dis.* **2015**, 211.
- (6) Morens, D. M.; Folkers, G. K.; Fauci, A. S. The Challenge of Emerging and Re-Emerging Infectious Diseases. *Nature* **2004**, 430, 242–249.
- (7) Marks, S. M.; Flood, J.; Seaworth, B.; Hirsch-Moverman, Y.; Armstrong, L.; Mase, S.; Salcedo, K.; Oh, P.; Graviss, E. a.; Colson, P. W.; *et al.* Treatment Practices, Outcomes, and Costs of Multidrug-Resistant and Extensively Drug-Resistant Tuberculosis, United States, 2005–2007. *Emerg. Infect. Dis.* **2014**, 20, 812–821.
- (8) Centers for Disease Control. Biggest Threats to Antibiotic/Antimicrobial Resistance http://www.cdc.gov/drugresistance/biggest_threats.html (accessed Mar 16, 2015).
- (9) World Health Organization. *Global Strategy and Targets for Tuberculosis Prevention , Care and Control after 2015*; 2015.
- (10) Rom, W.; Garay, S. M. *Tuberculosis*; Little Brown: Boston, 1996.
- (11) Golden, M. P.; Vikram, H. R. Extrapulmonary Tuberculosis: An Overview. *Am. Fam. Physician* **2005**, 72, 1761–1768.

- (12) Lin, P. L.; Flynn, J. L. *Nonhuman Primates in Biomedical Research*; Elsevier, 2012.
- (13) Parsons, L. M.; Somoskövi, Á.; Gutierrez, C.; Lee, E.; Paramasivan, C. N.; Abimiku, A.; Spector, S.; Roscigno, G.; Nkengasong, J. Laboratory Diagnosis of Tuberculosis in Resource-Poor Countries: Challenges and Opportunities. *Clin. Microbiol. Rev.* **2011**, *24*, 314–350.
- (14) Siddiqi, K.; Lambert, M.-L.; Walley, J. Clinical Diagnosis of Smear-Negative Pulmonary Tuberculosis in Low-Income Countries: The Current Evidence. *Lancet Infect. Dis.* **2003**, *3*, 288–296.
- (15) Parikh, R.; Mathai, A.; Parikh, S.; Chandra Sekhar, G.; Thomas, R. Understanding and Using Sensitivity, Specificity and Predictive Values. *Indian J. Ophthalmol.* *56*, 45–50.
- (16) Davis, J. L.; Cattamanchi, A.; Cuevas, L. E.; Hopewell, P. C.; Steingart, K. R. Diagnostic Accuracy of Same-Day Microscopy versus Standard Microscopy for Pulmonary Tuberculosis: A Systematic Review and Meta-Analysis. *Lancet Infect. Dis.* **2013**, *13*, 147–154.
- (17) Molicotti, P.; Bua, A.; Zanetti, S. Cost-Effectiveness in the Diagnosis of Tuberculosis: Choices in Developing Countries. *J. Infect. Dev. Ctries.* **2014**, *8*, 24–38.
- (18) Boyle, D.; Pai, M. UNITAID Tuberculosis Diagnostic - Technology and Market Landscape - 3rd Edition. **2014**.
- (19) Gates Foundation. Public-Private Partnership Announces Immediate 40 Percent Cost Reduction for Rapid TB Test | The Bill & Melinda Gates Foundation <http://www.gatesfoundation.org/media-center/press-releases/2012/08/publicprivate-partnership-announces-immediate-40-percent-cost-reduction-for-rapid-tb-test> (accessed Apr 18, 2015).
- (20) FIND. FIND - Price for Xpert® MTB/RIF and FIND country list http://www.finddiagnostics.org/about/what_we_do/successes/find-negotiated-prices/xpert_mtb_rif.html (accessed Apr 18, 2015).
- (21) World Health Organization. Systematic Screening for Active

- tuberculosis: Principles and Recommendations. *Who/Htm/Tb/2013.04* **2013**, 1–123.
- (22) Mukundan, H.; Kumar, S.; Price, D. N.; Ray, S. M.; Lee, Y. J.; Min, S.; Eum, S.; Kubicek-Sutherland, J.; Resnick, J. M.; Grace, W. K.; *et al.* Rapid Detection of Mycobacterium Tuberculosis Biomarkers in a Sandwich Immunoassay Format Using a Waveguide-Based Optical Biosensor. *Tuberculosis* **2012**, 92, 407–416.
 - (23) World Health Organization. *Commercial Serodiagnostic Tests for Diagnosis of Tuberculosis*; 2011.
 - (24) Alere Determine TB test <http://www.alere.com/au/en/product-details/determine-tb-lam.html>.
 - (25) World Health Organization. Commercial Serodiagnostic Tests for Diagnosis of Tuberculosis: Policy Statement. *Geneva WHO* **2011**.
 - (26) Gubala, V.; Harris, L. F.; Ricco, A. J.; Tan, M. X.; Williams, D. E. Point of Care Diagnostics: Status and Future. *Anal. Chem.* **2012**, 84, 487–515.
 - (27) Goldstein, B. P. Resistance to Rifampicin: A Review. *J. Antibiot. (Tokyo)*. **2014**, 67, 625–630.
 - (28) Andrews, J. R.; Shah, N. S.; Gandhi, N.; Moll, T.; Friedland, G. Multidrug-Resistant and Extensively Drug-Resistant Tuberculosis: Implications for the HIV Epidemic and Antiretroviral Therapy Rollout in South Africa. *J. Infect. Dis.* **2007**, 196 Suppl , S482–S490.
 - (29) World Health Organization. *Treatment of Tuberculosis: Guidelines*. **2010**.
 - (30) World Health Organisation. Anti-Tuberculosis Drug Resistance in the World. *World Health* **2008**, 1–153.
 - (31) Schnippel, K.; Rosen, S.; Shearer, K.; Martinson, N.; Long, L.; Sanne, I.; Variava, E. Costs of Inpatient Treatment for Multi-Drug-Resistant Tuberculosis in South Africa. *Trop Med Int Heal.* **2013**, 18, 109–116.

- (32) Gopinath, K.; Singh, S. Urine as an Adjunct Specimen for the Diagnosis of Active Pulmonary Tuberculosis. *Int. J. Infect. Dis.* **2009**, *13*, 374–379.
- (33) Pisitkun, T.; Shen, R.-F.; Knepper, M. a. Identification and Proteomic Profiling of Exosomes in Human Urine. *Proc. Natl. Acad. Sci. U. S. A.* **2004**, *101*, 13368–13373.
- (34) Pollock, N. R.; Macovei, L.; Kanunfre, K.; Dhiman, R.; Restrepo, B. I.; Zarate, I.; Pino, P. a.; Mora-Guzman, F.; Fujiwara, R. T.; Michel, G.; *et al.* Validation of Mycobacterium Tuberculosis Rv1681 Protein as a Diagnostic Marker of Active Pulmonary Tuberculosis. *J. Clin. Microbiol.* **2013**, *51*, 1367–1373.
- (35) Minion, J.; Leung, E.; Talbot, E.; Dheda, K.; Pai, M.; Menzies, D. Diagnosing Tuberculosis with Urine Lipoarabinomannan: Systematic Review and Meta-Analysis. *Eur. Respir. J.* **2011**, *38*, 1398–1405.
- (36) Lawn, S. D. Point-of-Care Detection of Lipoarabinomannan (LAM) in Urine for Diagnosis of HIV-Associated Tuberculosis: A State of the Art Review. *BMC Infect. Dis.* **2012**, *12*, 103.
- (37) Vaught, J. D.; Bock, C.; Carter, J.; Fitzwater, T.; Otis, M.; Schneider, D.; Rolando, J.; Waugh, S.; Wilcox, S. K.; Eaton, B. E. Expanding the Chemistry of DNA for in Vitro Selection. *J. Am. Chem. Soc.* **2010**, *132*, 4141–4151.
- (38) Bridonneau, P.; Bunch, S.; Tengler, R.; Hill, K.; Carter, J.; Pieken, W.; Tinnermeier, D.; Lehrman, R.; Drolet, D. W. Purification of a Highly Modified RNA-Aptamer. Effect of Complete Denaturation during Chromatography on Product Recovery and Specific Activity. *J. Chromatogr. B Biomed. Sci. Appl.* **1999**, *726*, 237–247.
- (39) Park, B. J.; Sa, Y. S.; Kim, Y. H.; Kim, Y. Spectroscopic and Electrochemical Detection of Thrombin/5'-SH or 3'-SH Aptamer Immobilized on (porous) Gold Substrates. *Bull. Korean Chem. Soc.* **2012**, *33*, 100–104.
- (40) Jimmy, B.; Jose, J. Patient Medication Adherence: Measures in Daily Practice. *Oman Med. J.* **2011**, *26*, 155–159.

- (41) Shepherd, M. Administration of Drugs 1: Oral Route. *Nurs. Times* **2011**, 107, 107.
- (42) Pokhrel, L. R.; Dubey, B.; Scheuerman, P. R. Impacts of Select Organic Ligands on the Colloidal Stability, Dissolution Dynamics, and Toxicity of Silver Nanoparticles. *Environ. Sci. Technol.* **2013**, 47, 12877–12885.
- (43) Rodov, V.; Droby, S.; Horev, B.; Vinokur, Y.; Poverenove, E.; Shlar, I. High-Throughput Screening of Nanoparticle-Stabilizing Ligands: Application to Preparing Antimicrobial Curcumin Nanoparticles by Antisolvent Precipitation. *Nano-Micro Lett.* **2015**, 7, 68–79.
- (44) Kudgus, R. A. Gold Nanoparticle Therapeutics: Disrupting Protein/Protein Interactions and the Treatment of Multidrug Resistant Pathogens, North Carolina State University, 2010.
- (45) Guignard, B.; Entenza, J. M.; Moreillon, P. Beta-Lactams against Methicillin-Resistant Staphylococcus Aureus. *Curr. Opin. Pharmacol.* **2005**, 5, 479–489.
- (46) Bresee, J.; Maier, K. E.; Melander, C.; Feldheim, D. L. Identification of Antibiotics Using Small Molecule Variable Ligand Display on Gold Nanoparticles. *Chem. Commun. (Camb)*. **2010**, 46, 7516–7518.
- (47) Bresee, J.; Bond, C. M.; Worthington, R. J.; Smith, C. a.; Gifford, J. C.; Simpson, C. a.; Carter, C. J.; Wang, G.; Hartman, J.; Osbaugh, N. a.; *et al.* Nanoscale Structure-Activity Relationships, Mode of Action, and Biocompatibility of Gold Nanoparticle Antibiotics. *J. Am. Chem. Soc.* **2014**, 136, 5295–5300.
- (48) Bresee, J.; Maier, K. E.; Boncella, A. E.; Melander, C.; Feldheim, D. L. Growth Inhibition of Staphylococcus Aureus by Mixed Monolayer Gold Nanoparticles. *Small* **2011**, 7, 2027–2031.
- (49) Gifford, J. C.; Bresee, J.; Carter, C. J.; Wang, G.; Melander, R. J.; Melander, C.; Feldheim, D. L. Thiol-Modified Gold Nanoparticles for the Inhibition of Mycobacterium Smegmatis. *Chem. Commun.* **2014**, 50, 15860–15863.

- (50) Tucci, P.; González-Sapienza, G.; Marin, M. Pathogen-Derived Biomarkers for Active Tuberculosis Diagnosis. *Front. Microbiol.* **2014**, *5*, 549.
- (51) Porter, M. D.; Lipert, R. J.; Siperko, L. M.; Wang, G.; Narayanan, R. SERS as a Bioassay Platform: Fundamentals, Design, and Applications. *Chem. Soc. Rev.* **2008**, *37*, 1001.
- (52) Yoon, K. J.; Seo, H. K.; Hwang, H.; Pyo, D.; Eom, I. Y.; Hahn, J. H.; Jung, Y. M. Bioanalytical Application of SERS Immunoassay for Detection of Prostate-Specific Antigen. *Bull. Korean Chem. Soc.* **2010**, *31*, 1215–1218.
- (53) Ma, X.; Qu, Q.; Zhao, Y.; Luo, Z.; Zhao, Y.; Ng, K. W.; Zhao, Y. Graphene Oxide Wrapped Gold Nanoparticles for Intracellular Raman Imaging and Drug Delivery. *J. Mater. Chem. B* **2013**, *1*, 6495.
- (54) Cheng, H.-W.; Huan, S.-Y.; Wu, H.-L.; Shen, G.-L.; Yu, R.-Q. Surface-Enhanced Raman Spectroscopic Detection of a Bacteria Biomarker Using Gold Nanoparticle Immobilized Substrates. *Anal. Chem.* **2009**, *81*, 9902–9912.
- (55) Jen Lin, Y. A Rapid and Sensitive Early Diagnosis of Influenza Virus Subtype via Surface Enhanced Raman Scattering. *J. Biosens. Bioelectron.* **2014**, *05*.
- (56) Park, H.; Porter, M. D.; Yeung, E. S.; Lin, V. S. Chip-Scale Bioassays Based on Surface-Enhanced Raman Scattering : Fundamentals and Applications. **2005**, 1–121.
- (57) Cho, H.; Baker, B. R.; Wachsmann-Hogiu, S.; Pagba, C. V.; Laurence, T. a.; Lane, S. M.; Lee, L. P.; Tok, J. B. H. Aptamer-Based SERRS Sensor for Thrombin Detection. *Nano Lett.* **2008**, *8*, 4386–4390.
- (58) Driscoll, A. J.; Harpster, M. H.; Johnson, P. A. The Development of Surface-Enhanced Raman Scattering as a Detection Modality for Portable in Vitro Diagnostics: Progress and Challenges. *Phys. Chem. Chem. Phys.* **2013**, *15*, 20415.
- (59) Chen, S.; Yuan, Y.; Yao, J.; Han, S.; Gu, R. Magnetic Separation and Immunoassay of Multi-Antigen Based on Surface Enhanced Raman

Spectroscopy. *Chem. Commun.* **2011**, 47, 4225.

- (60) Yakes, B. J.; Lipert, R. J.; Bannantine, J. P.; Porter, M. D. Detection of Mycobacterium Avium Subsp. Paratuberculosis by a Sonicate Immunoassay Based on Surface-Enhanced Raman Scattering. *Clin. Vaccine Immunol.* **2008**, 15, 227–234.
- (61) Granger, J. H.; Granger, M. C.; Firpo, M. A.; Mulvihill, S. J.; Porter, M. D. Toward Development of a Surface Enhanced Raman Scattering (SERS) Based Cancer Diagnostic Immunoassay Panel. *Analyst* **2013**, 138.
- (62) Fang, W.; Zhang, X.; Chen, Y.; Wan, L.; Huang, W.; Shen, A.; Hu, J. Portable SERS-Enabled Micropipettes for Microarea Sampling and Reliably Quantitative Detection of Surface Organic Residues. **2015**.
- (63) Owens, N. A.; Wampler, R. D.; Ying, Y.; Granger, J. H.; Porter, M. D. Succinimidyl Ester Surface Chemistry: Implications of the Competition between Aminolysis and Hydrolysis on Covalent Protein Immobilization. *Langmuir* **2014**, 30, 12868–12878.
- (64) Driskell, J. Surface-Enhanced Raman Scattering (SERS) for Detection in Immunoassays: Applications, Fundamentals, and Optimization. **2006**, 2006.
- (65) Prinzi, S.; Chatterjee, D.; Brennan, P. J. Structure and Antigenicity of Lipoarabinomannan from Mycobacterium Bovis BCG. *J. Gen. Microbiol.* **1993**, 139, 2649–2658.
- (66) Jarlier, V.; Nikaido, H. Mycobacterial Cell Wall: Structure and Role in Natural Resistance to Antibiotics. *Microbiol. Lett.* **1994**, 123, 11–18.
- (67) Russell, D. G.; Mwandumba, H. C.; Rhoades, E. E. Mycobacterium and the Coat of Many Lipids. *J Cell Biol* **2002**, 158, 421–426.
- (68) Briken, V.; Porcelli, S. a.; Besra, G. S.; Kremer, L. Mycobacterial Lipoarabinomannan and Related Lipoglycans: From Biogenesis to Modulation of the Immune Response. *Mol. Microbiol.* **2004**, 53, 391–403.

- (69) Chatterjee, D.; Khoo, K. H. Mycobacterial Lipoarabinomannan: An Extraordinary Lipoheteroglycan with Profound Physiological Effects. *Glycobiology* **1998**, 8, 113–120.
- (70) World Health Organization. New Laboratory Diagnostic Tools for Tuberculosis Control. *World Health* **2008**, 1–20.
- (71) Barrett; Rawlings; Woessner. *Handbook of Proteolytic Enzymes, 3rd Edition*; 2013.
- (72) Biochemicals, R. M. The Complete Guide for Protease Inhibition, 1999, 1–12.
- (73) Gerber, G.; Brendler, C. Evaluation of the Urologic Patient: History, Physical Examination, and Urinalysis. In *Campbell-Walsh Urology*; Elsevier, 2012.
- (74) WebMD. Total Serum protein <http://www.webmd.com/a-to-z-guides/total-serum-protein?page=2>.
- (75) Chen, R. F. MACROMOLECULES : Removal of Fatty Acids from Serum Albumin by Charcoal Treatment Removal of Fatty Acids by Charcoal Treatment from Serum Albumin. *J. Biol. Chem.* **1967**, 242, 173–181.
- (76) Scheider, W.; Fuller, J. K. An Effective Method for Defatting Albumin Using Resin Columns. *Biochim. Biophys. Acta* **1970**, 221, 376–378.
- (77) Baker, M. Blame It on the Antibodies. *Nature* **2015**, 521, 274–275.
- (78) Greenfield, E. A. *Antibodies: A Laboratory Manual*; Cold Spring Harbor Laboratory Press, 2014.
- (79) Kulbachinskiy, a V. Methods for Selection of Aptamers to Protein Targets. *Biochemistry. (Mosc)*. **2007**, 72, 1505–1518.
- (80) Gold, L.; Janjic, N.; Jarvis, T.; Schneider, D.; Walker, J. J. Aptamers and the RNA World , Past and Present Aptamers and the RNA World , Past and Present. **2010**, 1–9.

- (81) Eaton, B. E. The Joys of in Vitro Selection: Chemically Dressing Oligonucleotides to Satiating Protein Targets. *Curr. Opin. Chem. Biol.* **1997**, *1*, 10–16.
- (82) Chernecky, C. C.; Berger, B. J. *Laboratory Tests and Diagnostic Procedures*; Saunders Elsevier: St. Louis, Mo., 2008.
- (83) Davies, D. R.; Gelinas, A. D.; Zhang, C.; Rohloff, J. C.; Carter, J. D.; O'Connell, D.; Waugh, S. M.; Wolk, S. K.; Mayfield, W. S.; Burgin, A. B.; *et al.* Unique Motifs and Hydrophobic Interactions Shape the Binding of Modified DNA Ligands to Protein Targets. *Proc. Natl. Acad. Sci. U. S. A.* **2012**, *109*, 19971–19976.
- (84) Mazik, M.; Radunz, W.; Boese, R. Molecular Recognition of Carbohydrates with Acyclic Pyridine-Based Receptors. *J. Org. Chem.* **2004**, *69*, 7448–7462.
- (85) Sun, W.; Du, L.; Li, M. Aptamer-Based Carbohydrate Recognition. *Curr. Pharm. Des.* **2010**, *16*, 2269–2278.
- (86) Gold, L.; Ayers, D.; Bertino, J.; Bock, C.; Bock, A.; Brody, E. N.; Carter, J.; Dalby, A. B.; Eaton, B. E.; Fitzwater, T.; *et al.* Aptamer-Based Multiplexed Proteomic Technology for Biomarker Discovery. *PLoS One* **2010**, *5*.
- (87) Eaton, B. E.; Gold, L.; Hicke, B. J.; Janjić, N.; Jucker, F. M.; Sebesta, D. P.; Tarasow, T. M.; Willis, M. C.; Zichi, D. a. Post-SELEX Combinatorial Optimization of Aptamers. *Bioorganic Med. Chem.* **1997**, *5*, 1087–1096.
- (88) Hamula, C. L. a; Zhang, H.; Li, F.; Wang, Z.; Chris Le, X.; Li, X. F. Selection and Analytical Applications of Aptamers Binding Microbial Pathogens. *TrAC - Trends Anal. Chem.* **2011**, *30*, 1587–1597.
- (89) Alam, K. K.; Chang, J. L.; Burke, D. H. FASTAptamer: A Bioinformatic Toolkit for High-Throughput Sequence Analysis of Combinatorial Selections. *Mol. Ther. Acids* **2015**, *4*, e230.

- (90) Hianik, T.; Ostatná, V.; Sonlajtnerova, M.; Grman, I. Influence of Ionic Strength, pH and Aptamer Configuration for Binding Affinity to Thrombin. *Bioelectrochemistry* **2007**, *70*, 127–133.
- (91) Okazawa, a; Maeda, H.; Fukusaki, E.; Katakura, Y.; Kobayashi, a. In Vitro Selection of Hematoporphyrin Binding DNA Aptamers. *Bioorg. Med. Chem. Lett.* **2000**, *10*, 2653–2656.
- (92) Kang, S.; Hah, S. S. Improved Ligand Binding by Antibody-Aptamer Pincers. *Bioconjug. Chem.* **2014**, *25*, 1421–1427.
- (93) Verma, S.; Eckstein, F. Modified Oligonucleotides: Synthesis and Strategy for Users. *Annu. Rev. Biochem.* **1998**, *67*, 99–134.
- (94) Kusser, W. Chemically Modified Nucleic Acid Aptamers for in Vitro Selections: Evolving Evolution. *J. Biotechnol.* **2000**, *74*, 27–38.
- (95) Wang, L.; Clifford, B.; Graybeal, L.; Tolley, L.; McCarroll, M. E. Detection of Target Proteins by Fluorescence Anisotropy. *J. Fluoresc.* **2013**, *23*, 881–888.
- (96) Jameson, D. M. Fluorescence Polarisation/Anisotropy in Diagnostics and Imaging. *Burns* **2011**, *110*, 2685–2708.
- (97) Invitrogen. Fluorescence Polarization. *Tech. Resour. Guid.* **2006**.
- (98) Gradinaru, C. C.; Marushchak, D. O.; Samim, M.; Krull, U. J. Fluorescence Anisotropy: From Single Molecules to Live Cells. *Analyst* **2010**, *135*, 452–459.
- (99) Anisotropy, F. Fluorescence Anisotropy. *Princ. Fluoresc. Spectrosc.* **2006**, *64*, 353–382.
- (100) Zhang, D.; Lu, M.; Wang, H. Fluorescence Anisotropy Analysis for Mapping Aptamer À Protein. **2011**, 9188–9191.
- (101) Tran, D. T.; Janssen, K. P. F.; Pollet, J.; Lammertyn, E.; Anné, J.; Van Schepdael, A.; Lammertyn, J. Selection and Characterization of DNA

- Aptamers for Egg White Lysozyme. *Molecules* **2010**, *15*, 1127–1140.
- (102) Potty, A. S. R.; Kourentzi, K.; Fang, H.; Jackson, G. W.; Zhang, X.; Legge, G. B.; Willson, R. C. Biophysical Characterization of DNA Aptamer Interactions with Vascular Endothelial Growth Factor. *Biopolymers* **2009**, *91*, 145–156.
- (103) Unruh, J. R.; Gokulrangan, G.; Lushington, G. H.; Johnson, C. K.; Wilson, G. S. Orientational Dynamics and Dye-DNA Interactions in a Dye-Labeled DNA Aptamer. *Biophys. J.* **2005**, *88*, 3455–3465.
- (104) Perrier, S.; Ravelet, C.; Guieu, V.; Fize, J.; Roy, B.; Perigaud, C.; Peyrin, E. Rationally Designed Aptamer-Based Fluorescence Polarization Sensor Dedicated to the Small Target Analysis. *Biosens. Bioelectron.* **2010**, *25*, 1652–1657.
- (105) Lakowicz, J. R. *Principles of Fluorescence Spectroscopy, 3rd Edition*, Joseph R. Lakowicz, Editor, 2006.
- (106) Zhang, D.; Zhao, Q.; Zhao, B.; Wang, H. Fluorescence Anisotropy Reduction of Allosteric Aptamer for Sensitive and Specific Protein Signaling. *Anal. Chem.* **2012**, *84*, 3070–3074.
- (107) Blouin, S.; Craggs, T. D.; Lafontaine, D. A.; Penedo, J. C. DNA-Protein Interactions. *Methods Mol. Biol.* **2009**, *543*, 475–502.
- (108) Tuuminen, T. Urine as a Specimen to Diagnose Infections in Twenty-First Century: Focus on Analytical Accuracy. *Front. Immunol.* **2012**, *3*, 1–6.
- (109) Adachi, J.; Kumar, C.; Zhang, Y.; Olsen, J. V; Mann, M. The Human Urinary Proteome Contains More than 1500 Proteins, Including a Large Proportion of Membrane Proteins. *Genome Biol.* **2006**, *7*, R80.
- (110) Agilent, T. *BL21-Gold Competent Cells, BL21-Gold (DE3) Competent Cells, and BL21- Gold (DE3) pLysS Competent Cells - Instruction Manual*; 2014; Vol. 230130.
- (111) Cutler, J. I.; Auyeung, E.; Mirkin, C. A. Spherical Nucleic Acid. *J. Am.*

- Chem. Soc.* **2012**, 134, 1376–1391.
- (112) Prigodich, A. E.; et al. Multiplexed Nanoflares: mRNA Detection in Live Cells. *ACS Nano* **2009**, 3, 2147–2152.
- (113) Bardhan, R.; et al. Nanoshells with Targeted Simultaneous Enhancement of Magnetic and Optical Imaging and Photothermal Therapeutic Response. *Adv. Funtional Mater.* **2009**, 19, 3901–3909.
- (114) Lal, S.; Clare, S. E.; Halas, N. J. Nanoshell-Enabled Phtothermal Cancer Therapy: Impending Clinical Impact. *Acc. Chem. Res.* **2008**, 41, 1842–1851.
- (115) Lowery, A. R.; Gobin, A. M.; Day, E. S.; Halas, N. J.; West, J. L. Immunonanoshells for Targeted Photothermal Ablation of Tumor Cells. *Int. J. Nanomedicine* **2006**, 1, 149–154.
- (116) Dickerson, E. B.; et al. Gold Nanorod Assisted near-Infrared Plasmonic Photothermal Therapy (PPTT) of Squamous Cell Carcinoma in Mice. *Cancer Lett.* **2008**, 268, 57–66.
- (117) Huang, X. H.; Jain, P. K.; El-Sayed, I. H.; El-Sayed, M. A. Plasmonic Photothermal Therapy (PPTT) Using Gold Nanoparticles. *Lasers Med. Sci.* **2008**, 23, 217–228.
- (118) Xia, Y. N.; et al. Gold Nanocages: From Synthesis to Theranostic Applications. *Acc. Chem. Res.* **2011**, 44, 914–924.
- (119) Agbasi-Porter, C.; et al. Transcription Inhibition Using Oligonucleotide-Modified Gold Nanoparticles. *Bioconjug. Chem.* **2006**, 17, 1178–1183.
- (120) Ryan, J. A.; et al. Cellular Uptake of Gold Nanoparticles Passivated with BSA-SV40 Large T Antigen Conjugates. *Anal. Chem.* **2007**, 79, 9150–9159.
- (121) Targeting., M. gold nanoparticle-peptide complexes for nuclear. Tkachenko, A.G. et Al. *J. Am. Chem. Soc.* **2003**, 125, 4700–4701.

- (122) Zheng, D.; et al. Topical Delivery of siRNA-Based Spherical Nucleic Acid Nanoparticle Conjugates for Gene Regulation. *Proc. Natl. Acad. Sci. U. S. A.* **2012**, *109*, 11975–11980.
- (123) Bowman, M.-C.; Ballard, T. E.; Ackerson, C. J.; Feldheim, D. L.; Margolis, D. M.; Melander, C. Inhibition of HIV Fusion with Multivalent Gold Nanoparticles. *J. Am. Chem. Soc.* **2008**, *130*, 6896–6897.
- (124) Hillyer, J. F.; Albrecht, R. M. Gastrointestinal Persorption and Tissue Distribution of Differently Sized Colloidal Gold Nanoparticles. *J. Pharm. Sci.* **2001**, *90*, 1927–1936.
- (125) Schleh, C.; et al. Size and Surface Charge of Gold Nanoparticles Determine Absorption across Intestinal Barriers and Accumulation in Secondary Target Organs after Oral Administration. *Nanotoxicology* **2012**, *6*, 36–46.
- (126) Kiyono, H.; Fukuyama, S. NALT- VERSUS PEYER ' S-PATCH- MEDIATED MUCOSAL IMMUNITY. *Nat. Rev. Immunol.* **2004**, *4*, 699.
- (127) Beier, R.; Gebert, A. Kinetics of Particle Uptake in the Domes of Peyer's Patches. *Am J Physiol* **1998**, *275*, G130–G137.
- (128) Heel, A. K.; McCauley, R.; Papadimitriou, J. M.; Hall, J. C. SPECIAL ARTICLE REVIEW : Peyer ' S Patches. *J. Gastroenterol.* **1997**, *12*, 122–136.
- (129) Turner, J. R. Intestinal Mucosal Barrier Function in Health and Disease. *Nat. Rev. Immunol.* **2009**, *9*, 799–809.
- (130) Donovan, M.D., Flynn, G.L., Amidon, G. L. Absorption of Polyethylene Glycols 600 through 2000: The Molecular Weight Dependence of Gastrointestinal and Nasal Absorption. *scopus* **1990**, *7*, 863–868.
- (131) Cu, Y.; Saltzman, W. M. Controlled Surface Modification with Poly(ethylene)glycol Enhances Diffusion of PLGA Nanoparticles in Human Cervical Mucus. *Mol. Pharm.* **2010**, *6*, 173–181.

- (132) Bogart, L. K.; Pourroy, G.; Murphy, C. J.; Puentes, V.; Pellegrino, T.; Rosenblum, D.; Peer, D.; Lévy, R. Nanoparticles for Imaging, Sensing, and Therapeutic Intervention. *ACS Nano* **2014**, *8*, 3107–3122.
- (133) McConnell, E. L.; Basit, A. W.; Murdan, S. Measurements of Rat and Mouse Gastrointestinal pH, Fluid and Lymphoid Tissue, and Implications for in-Vivo Experiments. *J. Pharm. Pharmacol.* **2008**, *60*, 63–70.
- (134) Kararli, T. T. Comparison of the Gastrointestinal Anatomy, Physiology, and Biochemistry of Humans and Commonly Used Laboratory Animals. *Biopharm. Drug Dispos.* **1995**, *16*, 351–380.
- (135) Degen, L. P.; Phillips, S. F. Variability of Gastrointestinal Transit in Healthy Women and Men. *Gut* **1996**, *39*, 299–305.
- (136) Simpson, C. A.; Salleng, K. J.; Cliffel, D. E.; Feldheim, D. L. In Vivo Toxicity, Biodistribution, and Clearance of Glutathione-Coated Gold Nanoparticles. *Nanomedicine* **2013**, *9*, 257–263.
- (137) Witschi, A.; Reddy, S.; Stofer, B.; Lauterburg, B. H. The Systematic Availability of Oral Glutathione. *Eur. J. Clin. Pharm.* **1992**, *43*, 667–669.
- (138) Simpson, C. a; Rape, A. C.; Balinski, A.; Harkness, K. M.; Cliffel, D. E. Short-Chain PEG Mixed-Monolayer Protected Gold Clusters Increase Clearance and Red Blood Cell Counts SI. *ACS Nano* **2011**, 1–8.
- (139) Häkkinen, H. The Gold–sulfur Interface at the Nanoscale. *Nat. Chem.* **2012**, *4*, 443–455.
- (140) Dubois, L. H.; Nuzzo, R. G. Synthesis, Structure, and Properties of Model Organic Surfaces. *Annu. Rev. Phys. Chem.* **1992**, *43*, 437–463.
- (141) Gronbeck, H.; Curioni, A.; Andreoni, W. Thiols and Disulfides on the Au (111) Surface: The Headgroup - Gold Interaction. *J. Am. Chem. Soc.* **2000**, *122*, 3839–3842.
- (142) Garusinghe, G.; Bessey, S.; Aghamoosa, M.; McKinnon, M.; Bruce, A.; Bruce, M. Disulfide Competition for Phosphine Gold(I) Thiolates:

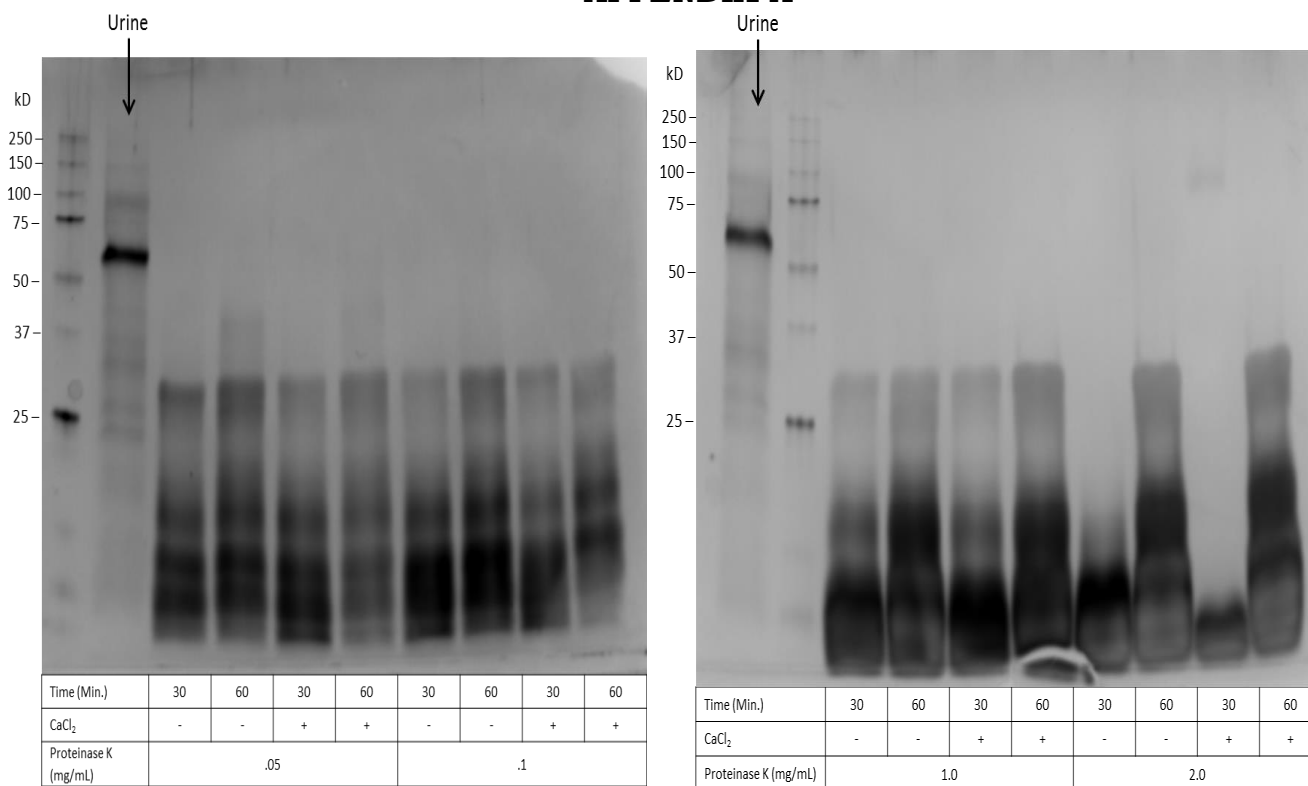
Phosphine Oxide Formation vs. Thiolate Disulfide Exchange. *Inorganics* **2015**, 3, 40–54.

- (143) Fremont, P. de. *Synthesis of Well-Defined N-Heterocyclic Carbene (NHC) Complexes of Late Transition Metals*; ProQuest, 2007.
- (144) Liu, X.; Yu, M.; Kim, H.; Mameli, M.; Stellacci, F. Determination of Monolayer-Protected Gold Nanoparticle Ligand-Shell Morphology Using NMR. *Nat. Commun.* **2012**, 3, 1182.
- (145) Hellmig, S.; Von Schöning, F.; Gadow, C.; Katsoulis, S.; Hedderich, J.; Fölsch, U. R.; Stüber, E. Gastric Emptying Time of Fluids and Solids in Healthy Subjects Determined by ¹³C Breath Tests: Influence of Age, Sex and Body Mass Index. *J. Gastroenterol. Hepatol.* **2006**, 21, 1832–1838.
- (146) Jadzinsky, P. D.; Calero, G.; Ackerson, C. J.; Bushnell, D. A.; Kornberg, R. D. Structure of a Thiol Monolayer-Protected Gold Nanoparticle at 1.1 Angstrom Resolution. *Science (80-.).* **2007**, 318, 430–433.
- (147) NIH <http://oacu.od.nih.gov/ARAC/Bleeding.pdf>.
- (148) Kurien, B. T.; Scofield, R. H. Mouse Urine Collection Using Clear Plastic Wrap. *Lab Anim. (NY)*. **1998**, 33, 83–86.
- (149) Guyton, A. C.; Hall, J. E. *Textbook of Medical Physiology*; 2006.
- (150) Gottfried, J. *History Repeating? Avoiding a Return to the Pre-Antibiotic Age*; Boston, 2015.
- (151) Clinical and Laboratory Standards institute. *Methods for Dilution Antimicrobial Susceptibility Testing for Bacteria That Grow Aerobically*; 2009; Vol. 29.
- (152) Andrews, J. M. Determination of Minimum Inhibitory Concentrations. *J. Antimicrob. Chemother.* **2001**, 48 Suppl 1, 5–16.
- (153) Lyon, R. C.; Taylor, J. S.; Porter, D. A.; Prasanna, H. R.; Hussain, A. S. Stability Profiles of Drug Products Extended beyond Labeled Expiration

- Dates. *J. Pharm. Sci.* **2006**, 95, 1549–1560.
- (154) Bullock, S. *Fundamentals of Pharmacology*; Pearson Education Australia: Frenchs Forest NSW, 2007.
- (155) Reichlin, S. *Handbook of Experimental Pharmacology*; 1969; Vol. 258.
- (156) Code of Federal Regulations. In; U.S. Food and Drug Administration: United States of America, 2014.
- (157) Romich, J. *Fundamentals of Pharmacology for Veterinary Technicians*; Cengage Learning, 2010.
- (158) Florence, A. T. Parenteral Routes of Drug Administration. In *Physicochemical Principles of Pharmacy*; 2011; pp. 372–277.
- (159) Immordino, M. L.; Dosio, F.; Cattel, L. Stealth Liposomes: Review of the Basic Science, Rationale, and Clinical Applications, Existing and Potential. *Int. J. Nanomedicine* **2006**, 1, 297–315.
- (160) Dos Santos, N.; Allen, C.; Doppen, A. M.; Anantha, M.; Cox, K. a K.; Gallagher, R. C.; Karlsson, G.; Edwards, K.; Kenner, G.; Samuels, L.; *et al.* Influence of Poly(ethylene Glycol) Grafting Density and Polymer Length on Liposomes: Relating Plasma Circulation Lifetimes to Protein Binding. *Biochim. Biophys. Acta - Biomembr.* **2007**, 1768, 1367–1377.
- (161) Taylor, M. J.; Tanna, S.; Sahota, T. In Vivo Study of a Polymeric Glucose-Sensitive Insulin Delivery System Using a Rat Model. *J. Pharm. Sci.* **2010**, 99, 4215–4227.
- (162) Webb, M. S.; Saxon, D.; Wong, F. M. P.; Lim, H. J.; Wang, Z.; Bally, M. B.; Choi, L. S. L.; Cullis, P. R.; Mayer, L. D. Comparison of Different Hydrophobic Anchors Conjugated to Poly(ethylene Glycol): Effects on the Pharmacokinetics of Liposomal Vincristine. *Biochim. Biophys. Acta - Biomembr.* **1998**, 1372, 272–282.
- (163) Bresee, J. Combinatorial Display of Small Molecule Ligands on Gold Nanoparticles for Antimicrobial Properties, 2012.

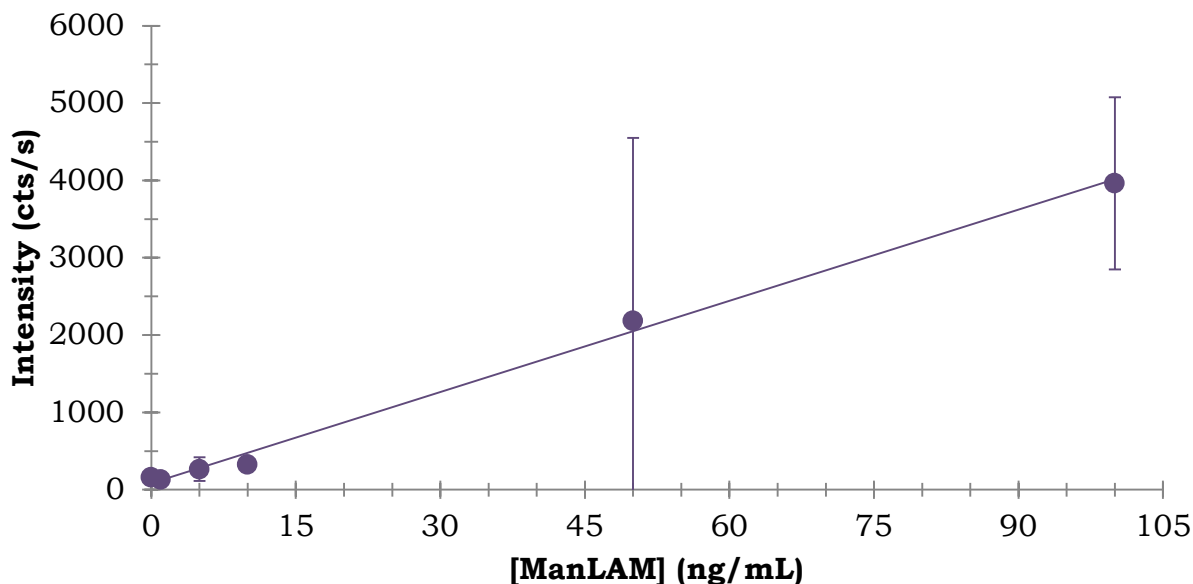
- (164) Rance, G. a.; Marsh, D. H.; Khlobystov, A. N. Extinction Coefficient Analysis of Small Alkanethiolate-Stabilised Gold Nanoparticles. *Chem. Phys. Lett.* **2008**, 460, 230–236.
- (165) mummy-and-man-extracting-hair.jpeg (1152×1443)
<http://picturescollections.com/wp-content/uploads/2012/04/mummy-and-man-extracting-hair.jpeg> (accessed Apr 21, 2015).
- (166) Kubica, G. P. Acid Fast Stained Mycobacterium Tuberculosis
<http://phil.cdc.gov/phil/details.asp?pid=4427> (accessed Apr 22, 2015).
- (167) Doucleff, M. (NPR); Hurt, A. (NPR); Menzies, D. R. (Montreal C. I. What It Takes To Cure Drug-Resistant Tuberculosis
<http://www.npr.org/blogs/health/2013/07/09/200387607/what-it-takes-to-cure-drug-resistant-tuberculosis>

APPENDIX A

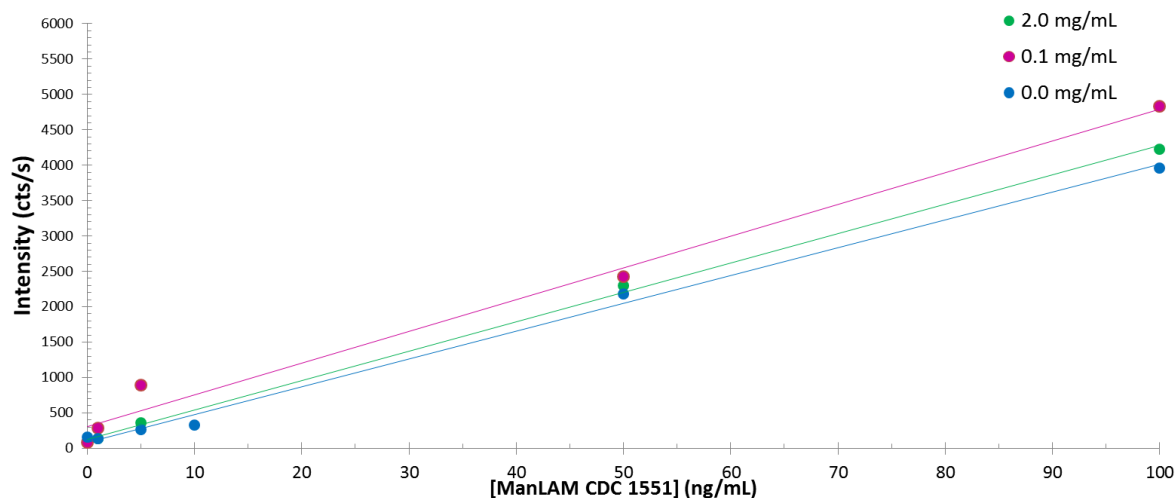


A1. Polyacrylamide gels of protein in 400 μL non-endemic urine before and after treatment with proteinase K. The gels have been stained with silver stain in order to visualize how the proteins ran on the gel. Variables in this experiment are time, CaCl_2 , and concentration of proteinase K. Calcium Chloride is a co-factor that improves performance of the proteinase K. It is evident from the gels that the enzyme only requires 30 minutes and 0.05 mg/mL proteinase K to degrade the protein, in fact it undergoes autolysis too.

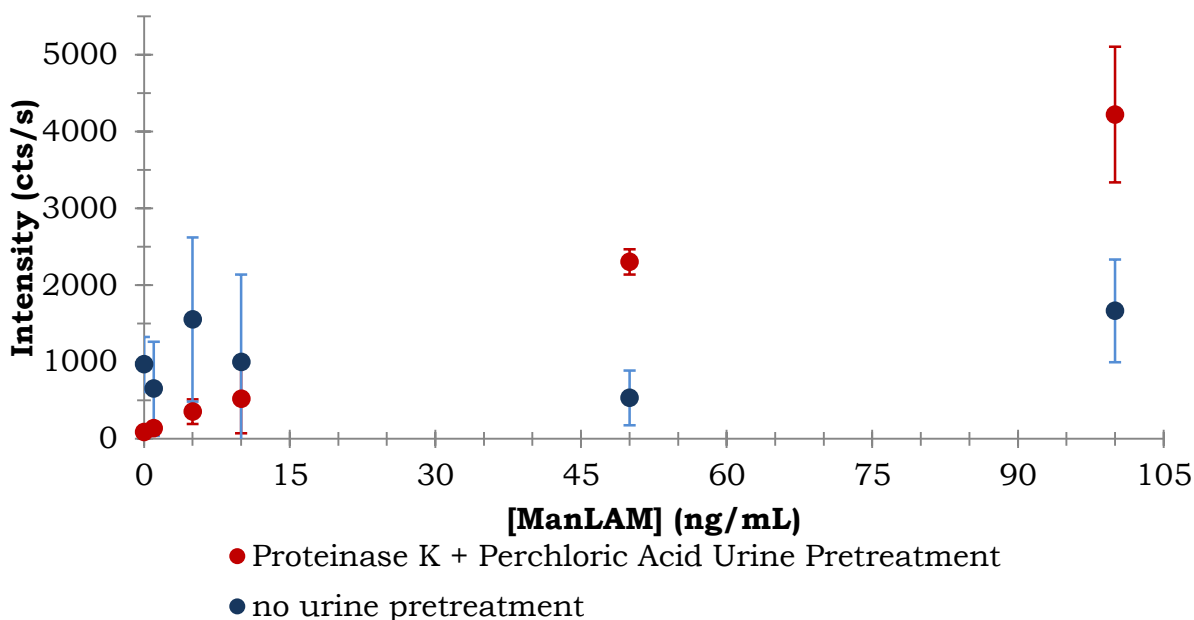
14000
12000



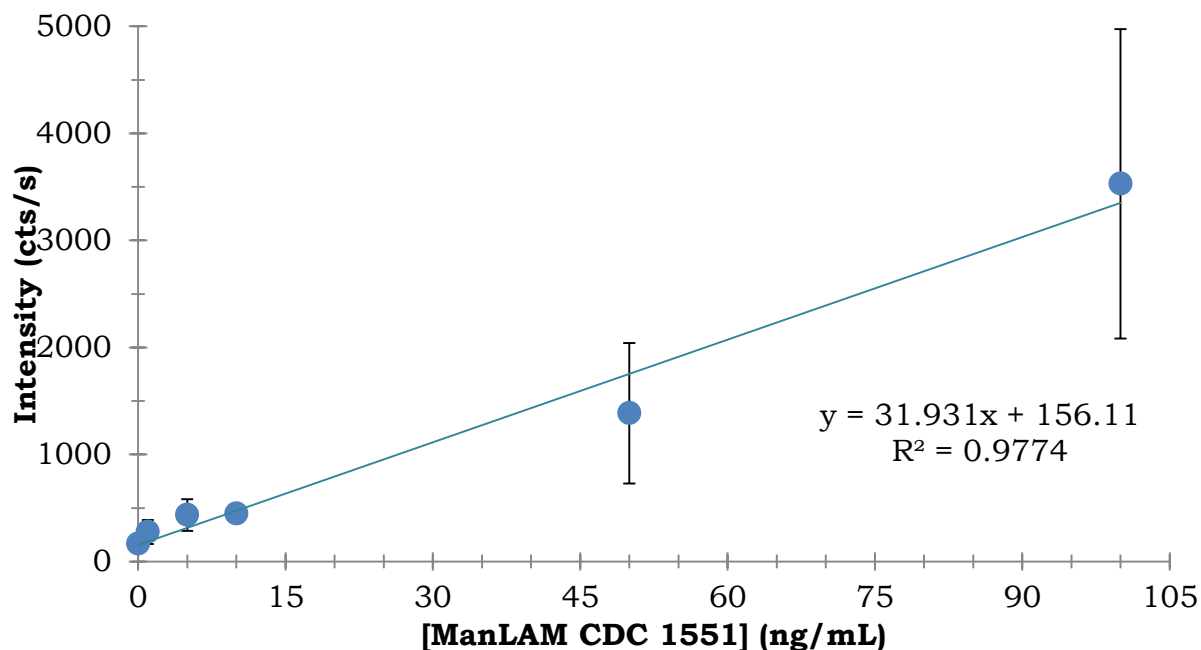
A3. SERS immunoassay dose response curve on non-endemic urine spiked with ManLAM and utilizing a perchloric acid pretreatment step meant to precipitate out any protein from the urine.



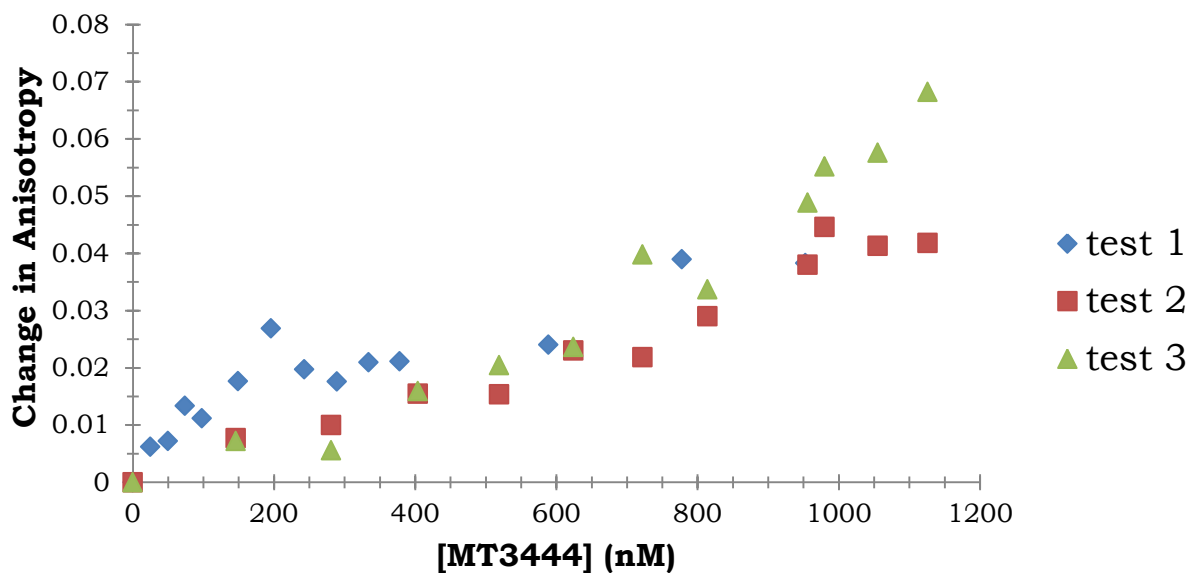
A4. SERS immunoassay dose response curve on non-endemic urine spiked with ManLAM; in addition to a pretreatment step involving a proteinase K step at a concentration (0.0-2.0 mg/mL) to degrade protein followed by a perchloric acid step to precipitate out any protein from the urine. The intensities for all three assays were within the standard deviation of the lowest proteinase K concentration. However, the standard deviation decreased with increasing



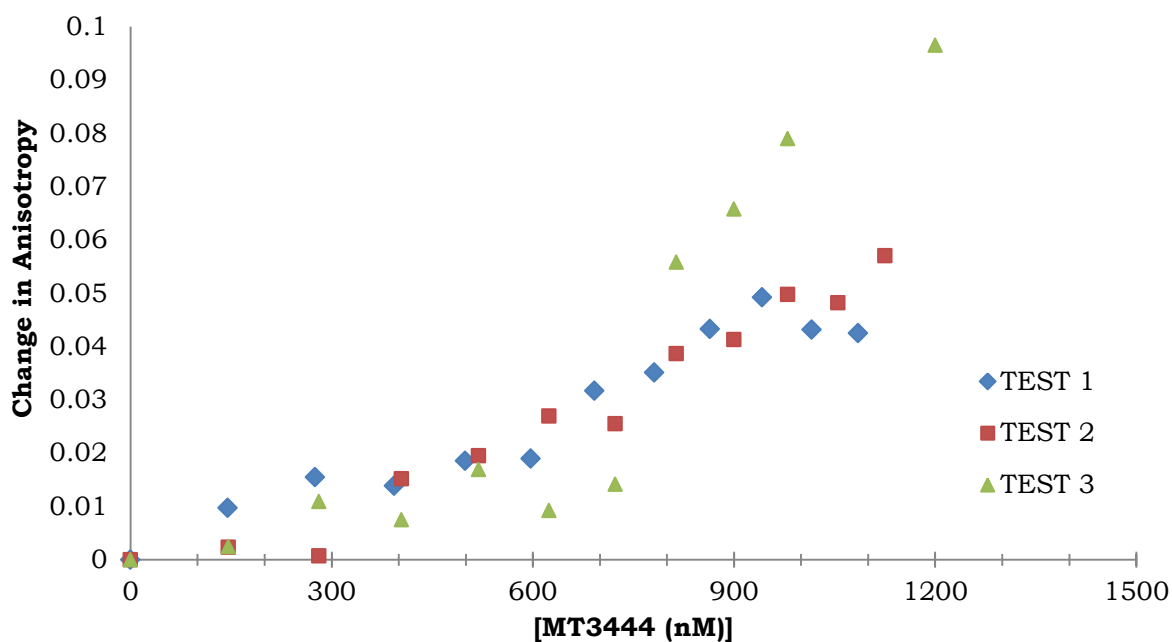
A5. SERS immunoassay dose response curve on non-endemic urine spiked with ManLAM. In red, a curve with 2 pretreatment steps involving proteinase K to degrade the protein and release ManLAM and perchloric acid to precipitate out any protein from the urine. In blue, a curve with no pretreatment.



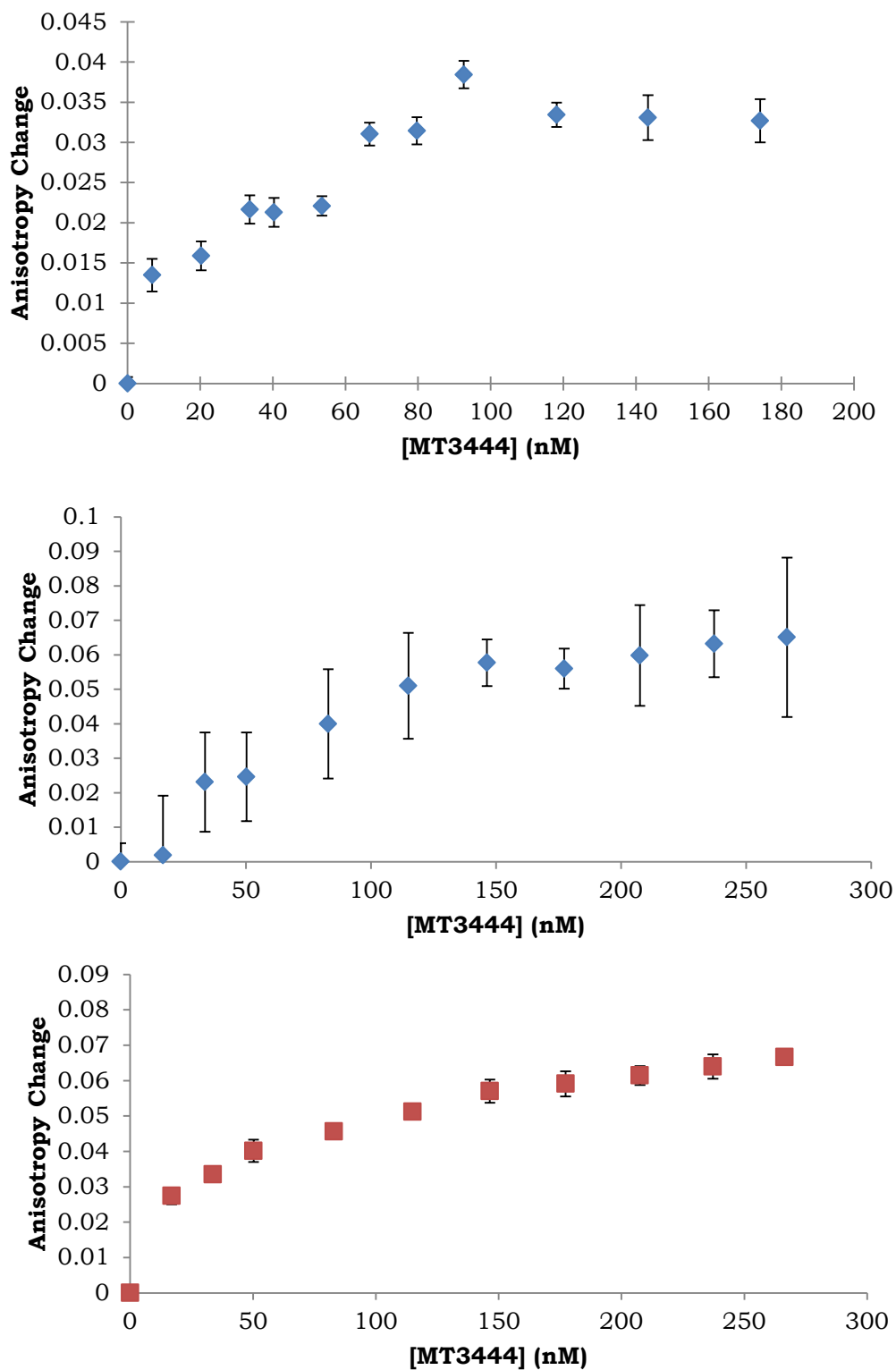
A6. SERS immunoassay dose response curve on non-endemic urine spiked with ManLAM, and a pretreatment step involving a 1.0 mg/mL proteinase K and sulfo-salicylic acid to precipitate out any protein from the urine. Sulfo-salicylic acid is safer to use than perchloric acid. However, perchloric acid has better signal to noise.



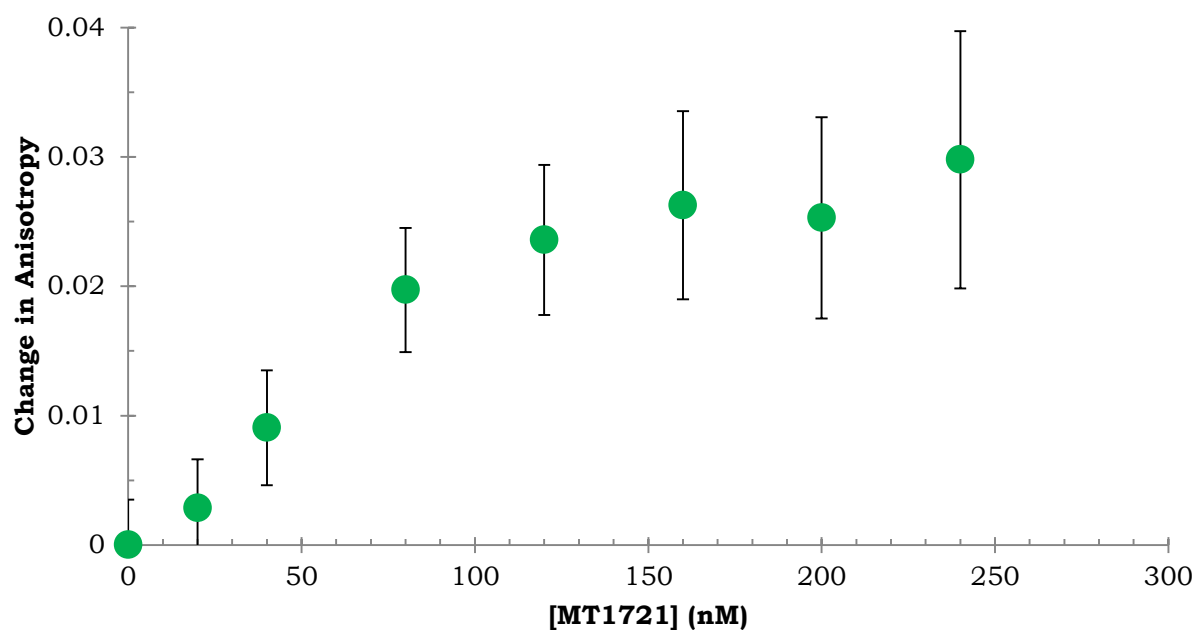
A7. FPA assay of a random library containing the modified-nucleotide naphthyl. According to Graphpad Prism, the data is not converged and a Kd cannot be calculated from the data.



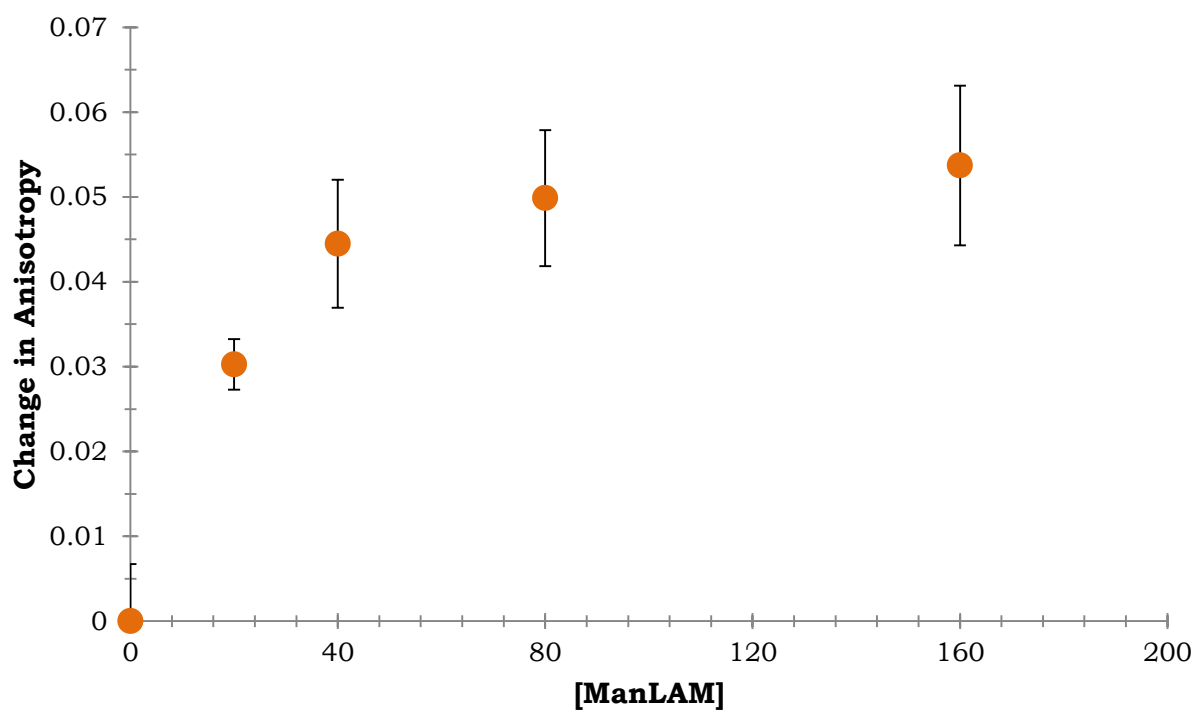
A8. FPA assay of a random library containing the trypt-amino modified-nucleotide. According to Graphpad Prism, the data is converged and the approximate Kd is 800 nM \pm 200 nM.



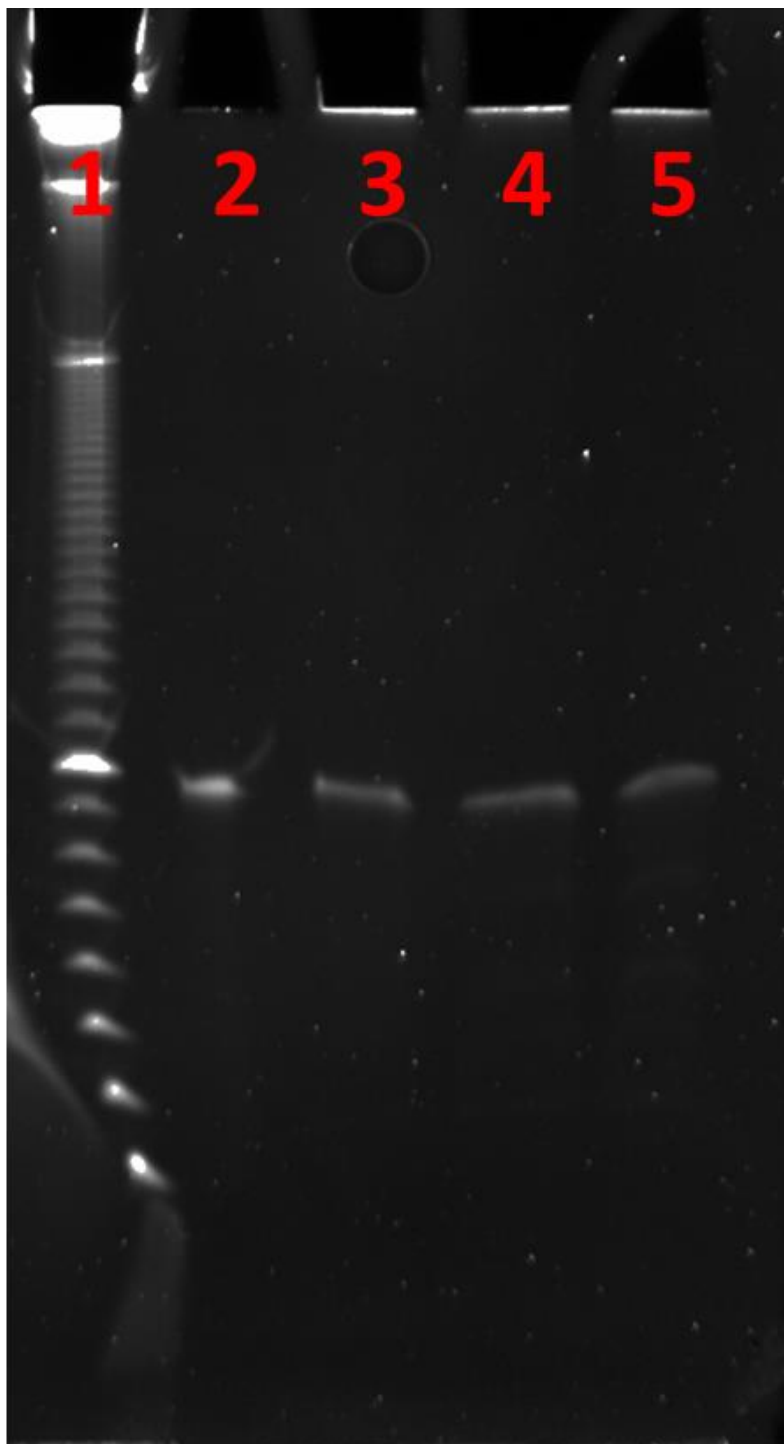
A9. FPA assays of aptamer T01 that binds MT3444: (top) assay in buffer, (middle) assay in urine, and (bottom) assay in dialyzed urine.



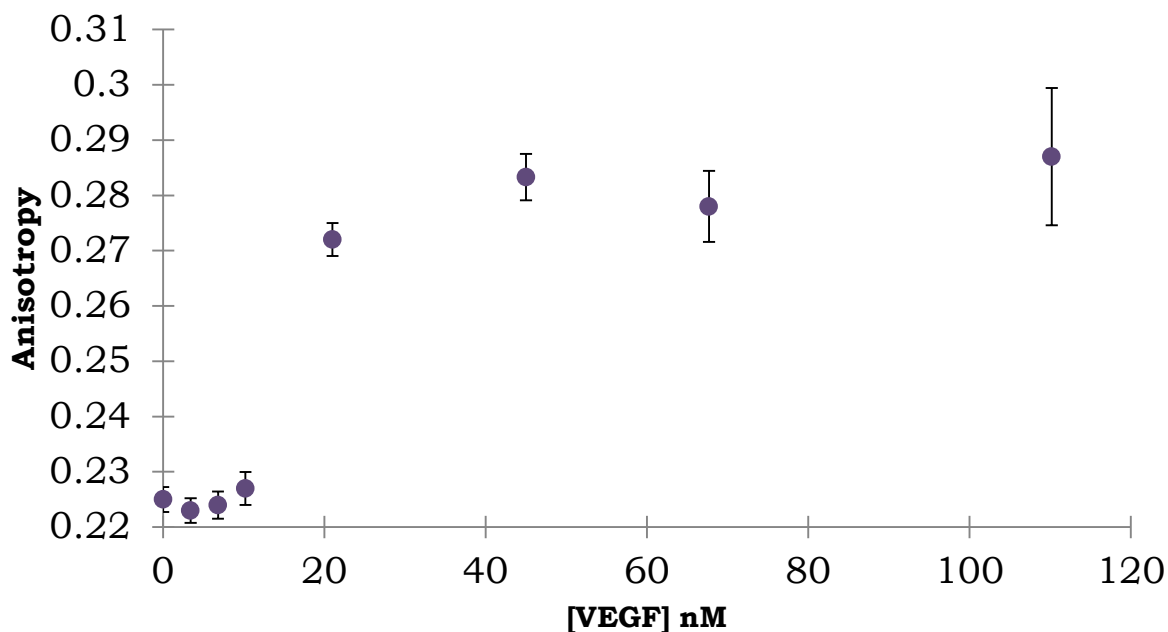
A10. FPA assays of aptamer 9T that binds MT1721 in buffer.



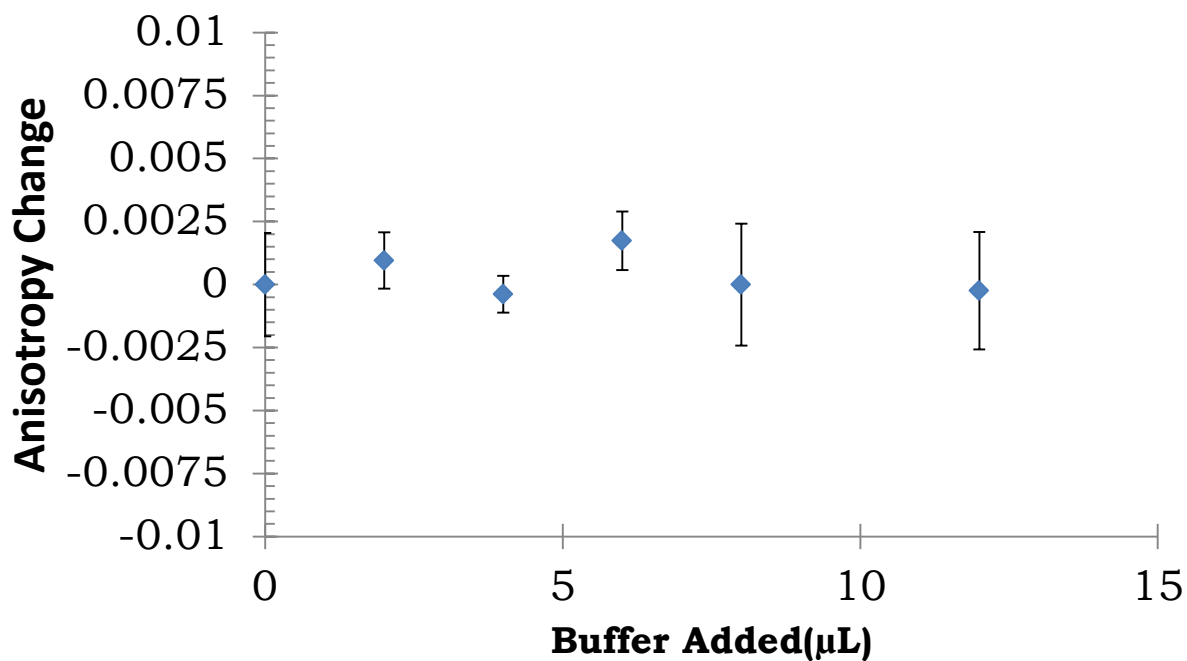
A11. FPA assays of aptamer CS09 that binds ManLAM in buffer.



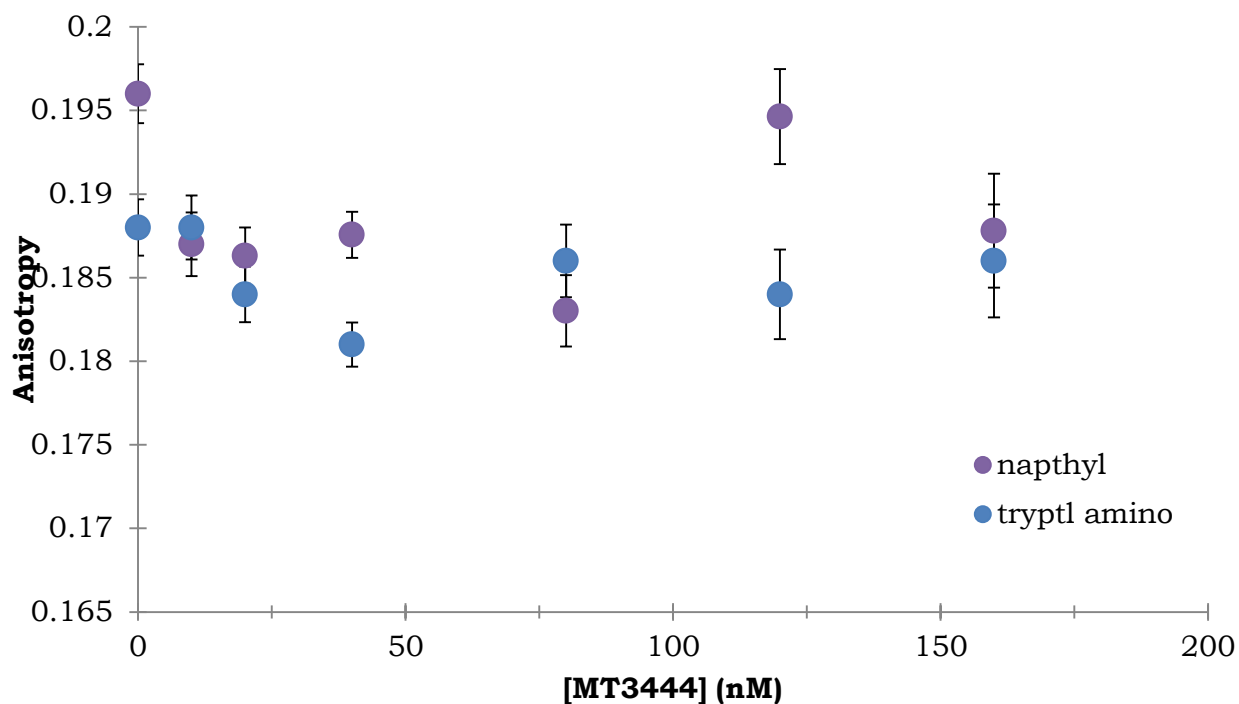
A12. Aptamer degradation assay in urine. A sample of aptamer was incubated with urine and then run on a denaturing polyacrylamide gel. The gel has 4 samples and one lane with a DNA standard control called a ladder. The single bands in lanes 2-5 are aptamer at an approximate length of ~92 base pairs. The lanes were as follows: (lane 1) DNA ladder, (lane 2) 0 minute incubation, (lane 3) 20 minute incubation, (lane 4) 40 minute incubation, and (lane 5) 60 minute incubation.



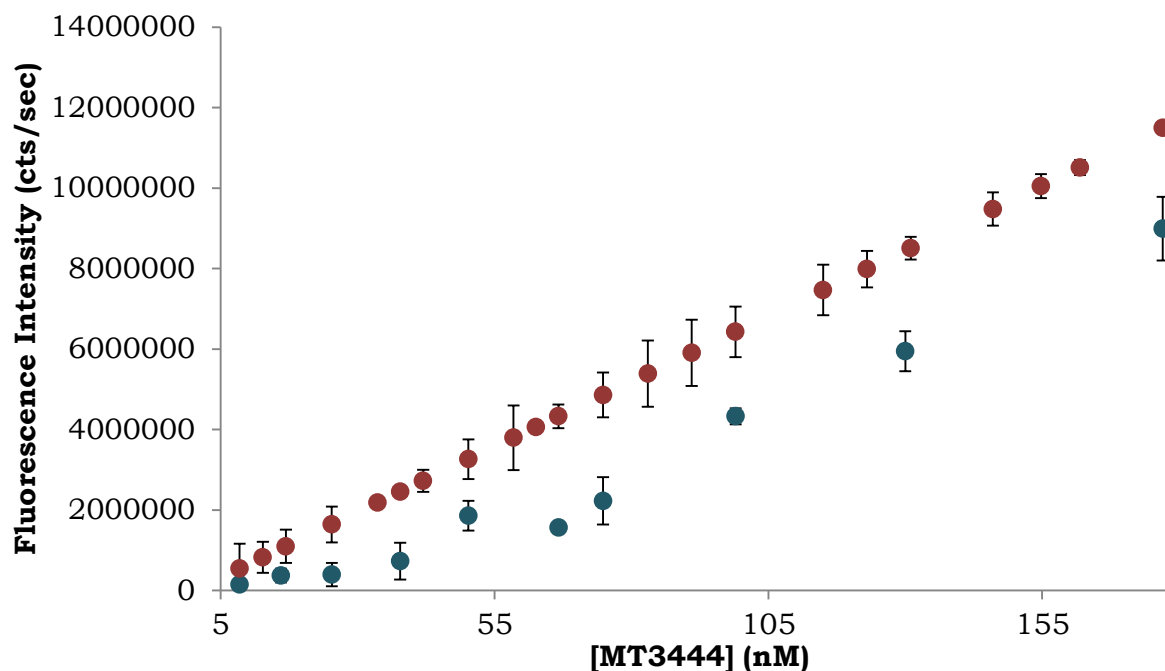
A13. FPA assay positive control to confirm that the assay is being run correctly for aptamers. The VEGF protein aptamer binds and creates a positive change in anisotropy. The raw data is shown above.



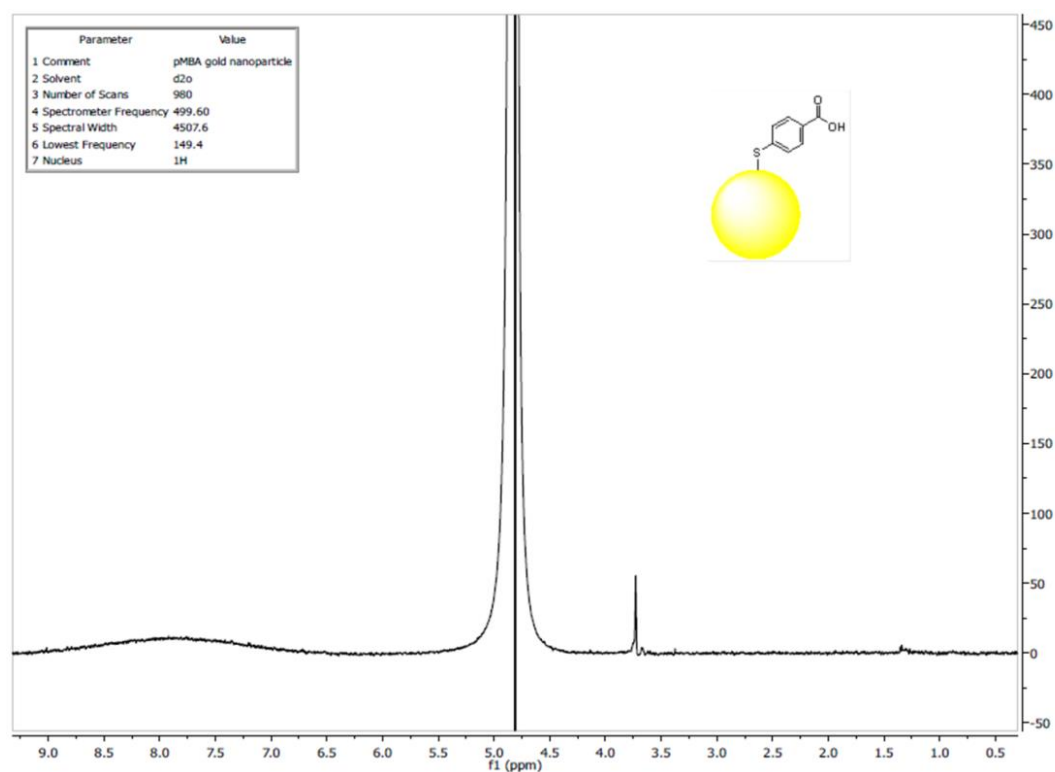
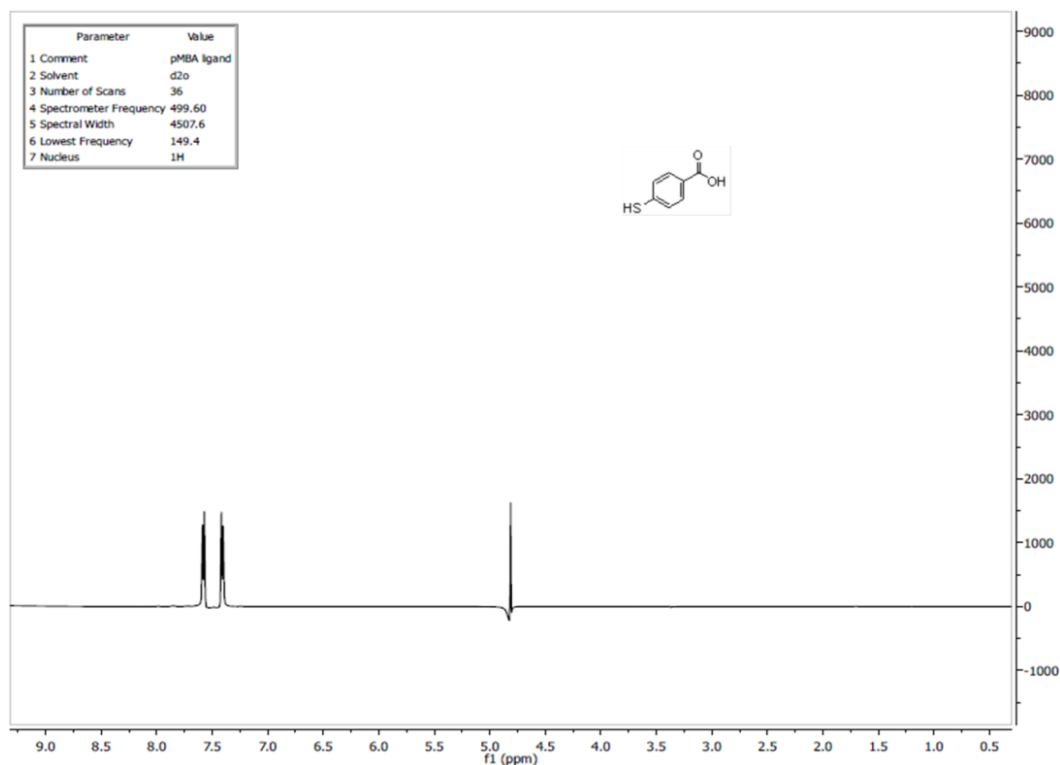
A14A. FPA assay negative control of aptamer N18 with just buffer added to the cuvette.



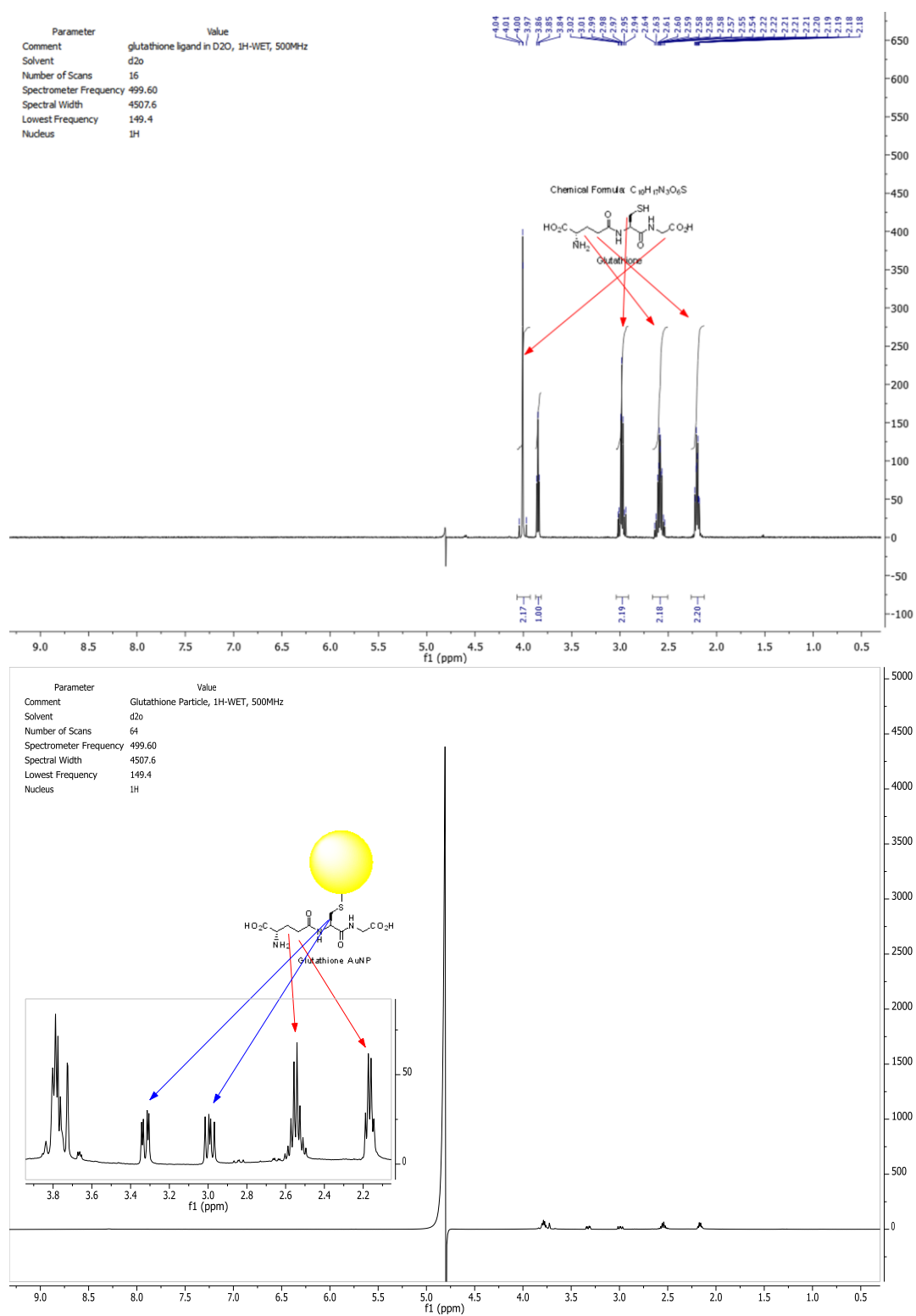
A14B. FPA assay negative control of aptamer with scrambled sequence for both a naphthyl sequence (purple) and a tryptl amino sequence (blue).



A15. Tryptophan Quenching assay for aptamer N18 binding its target protein MT3444. The fluorescence intensities of the MT3444 protein both exposed to aptamer N18 in (blue) and with protein only (yellow).

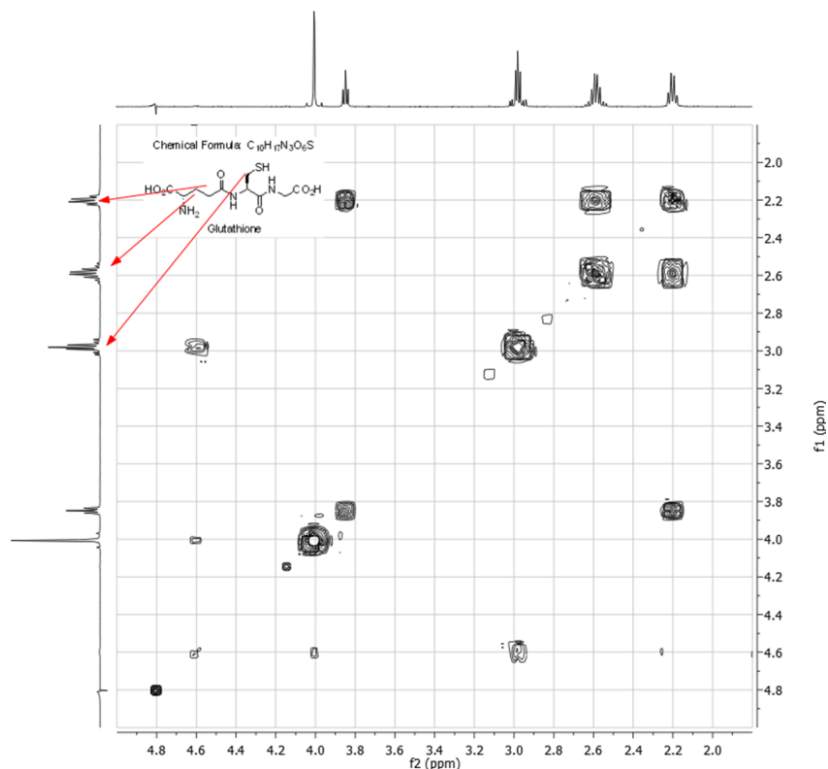


A16. ¹H NMR spectra in D₂O/H₂O for the *para*-mercaptobenzoic acid (pMBA) (top) and pMBA-coated gold nanoparticles (bottom). The ligand spectrum shows two sharp aromatic protons of pMBA. The pMBA-coated gold nanoparticle spectrum displays a broad peak spanning the same region. The broadening is due to the decreased rotational freedom of the ligand when attached to the surface of the nanoparticle and also the slow tumbling of that nanoparticle as it rotates in solution compared to a free pMBA in solution.

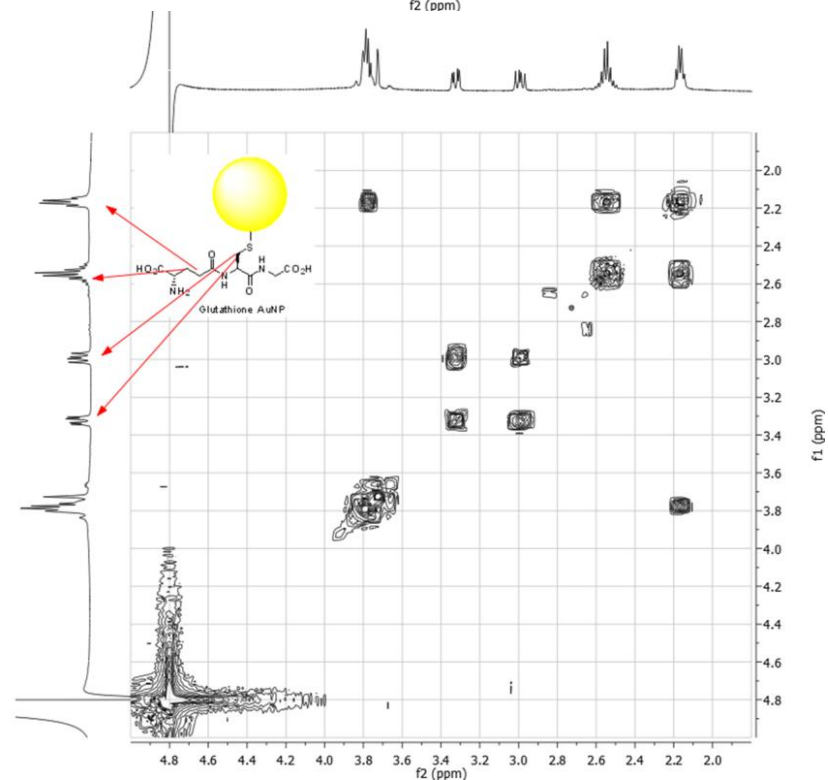


A17. NMR spectra in D₂O/H₂O for glutathione ligand (top) and glutathione-coated gold nanoparticles (bottom) .

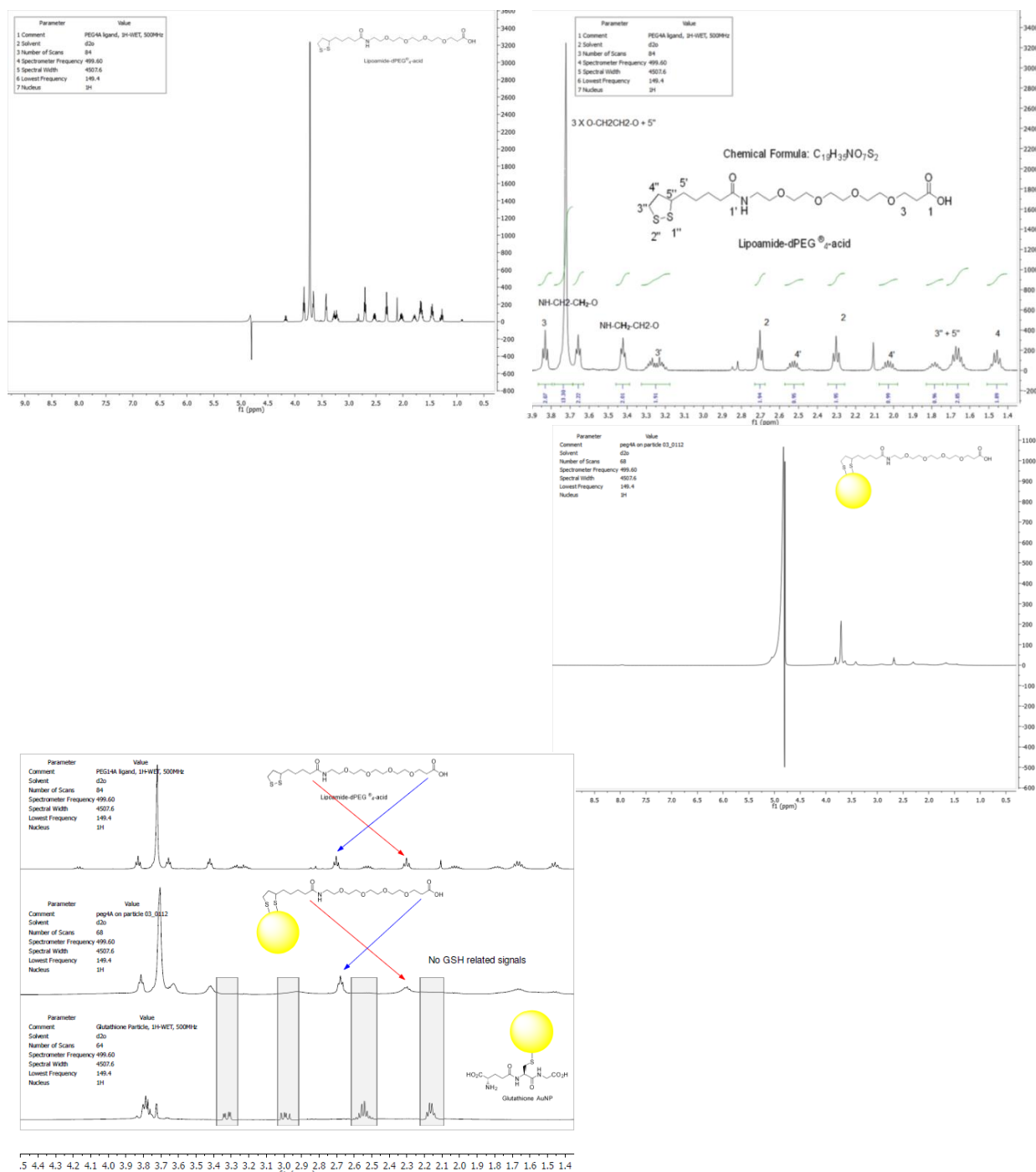
Parameter Value (f2, f1)
 Comment Glutathione ligand,
 WET-gCOSY, 500MHz
 Solvent d2o
 Number of Scans 2
 Spectrometer Frequency (499.60, 499.60)
 Spectral Width (4507.6, 4507.6)
 Lowest Frequency (149.4, 149.4)
 Nucleus (1H, 1H)



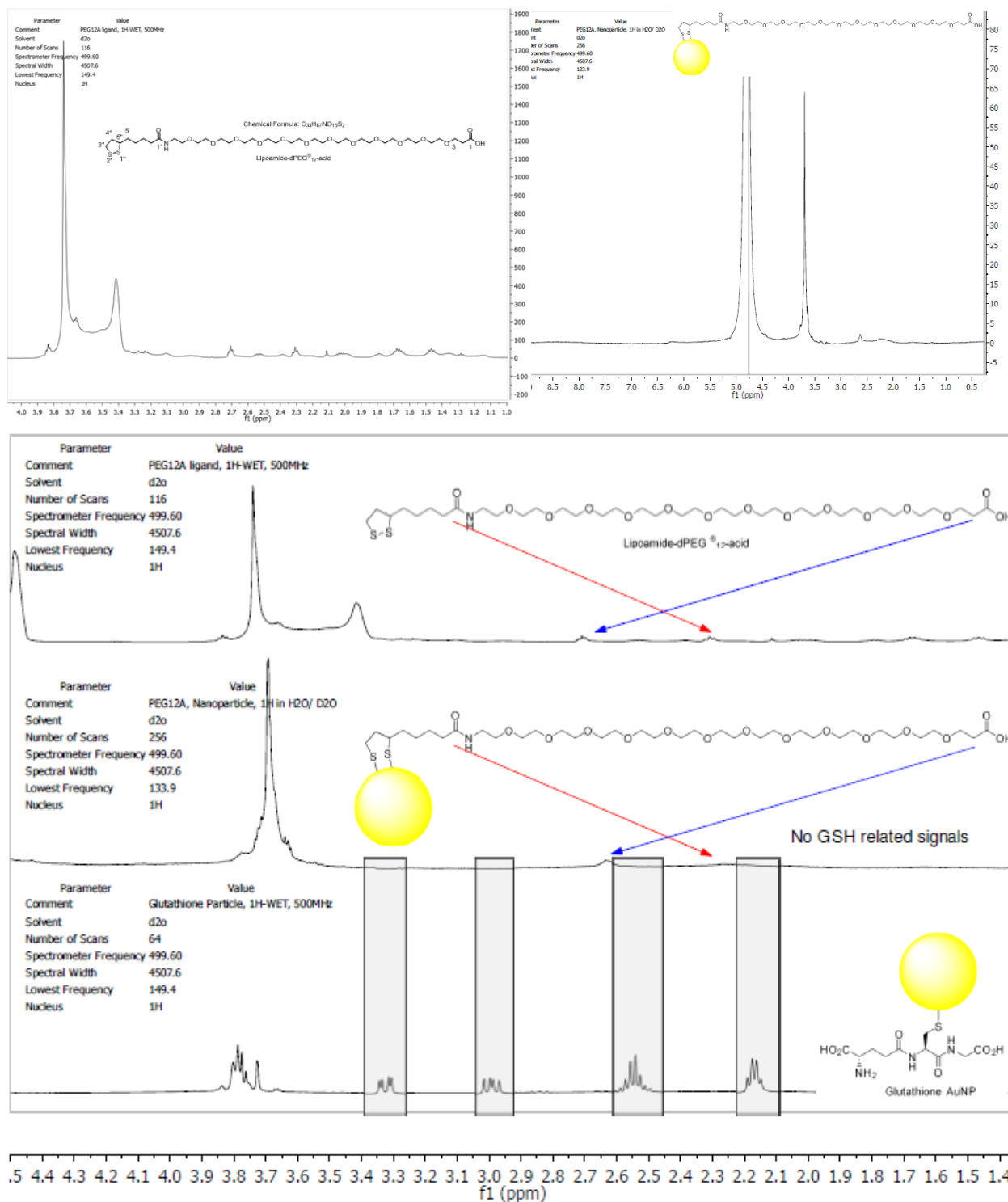
Parameter Value (f2, f1)
 Comment Glutathione Particle,
 WET-gCOSY, 500MHz
 Solvent d2o
 Number of Scans 2
 Spectrometer Frequency (499.60, 499.60)
 Spectral Width (4507.6, 4507.6)
 Lowest Frequency (149.4, 149.4)
 Nucleus (1H, 1H)



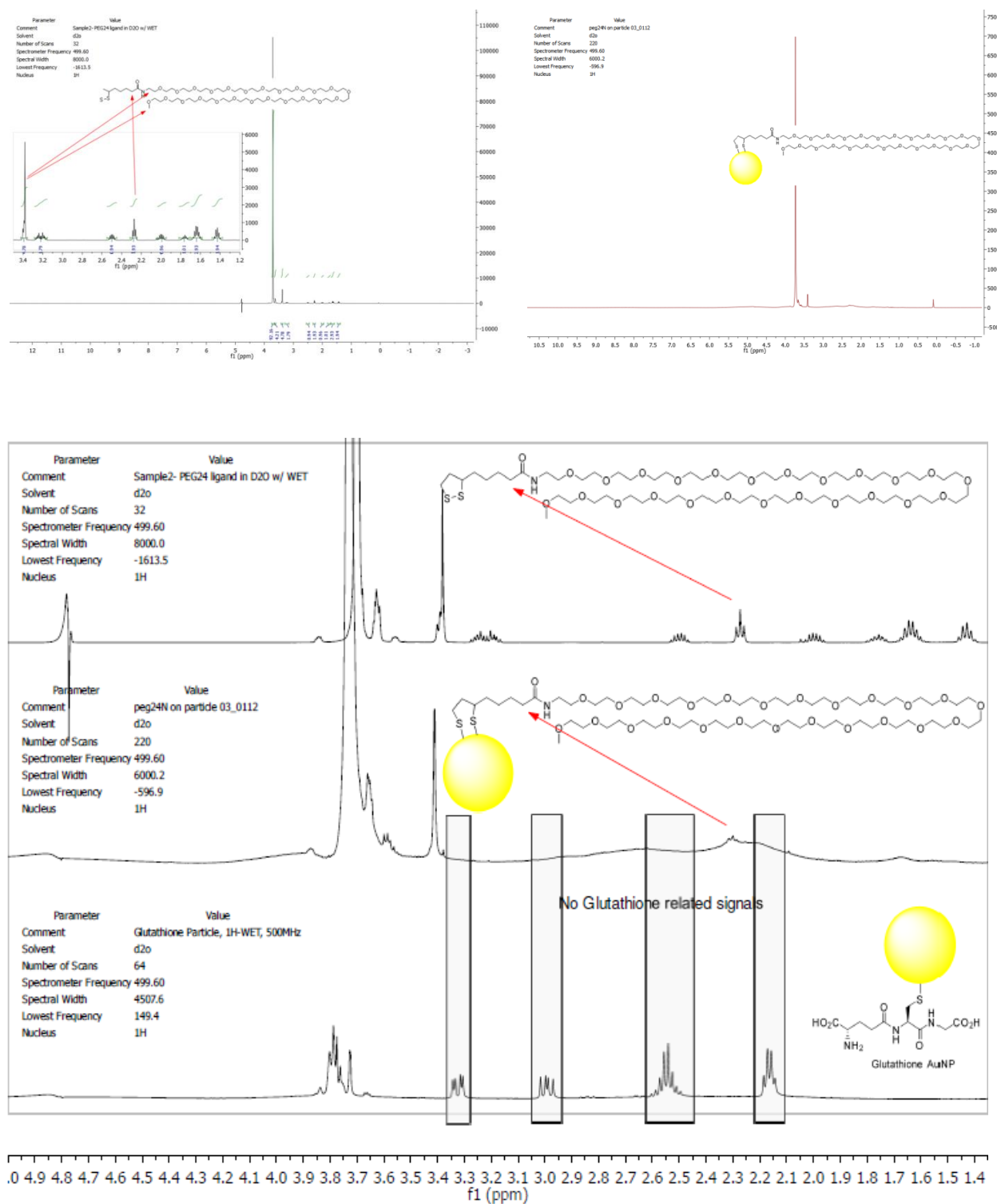
A18. Gradient COSY 1H NMR spectra in D₂O/H₂O for the glutathione (GSH) ligand and gold nanoparticles. Spectra are as follows GSH ligand (top) and GSH gold nanoparticles (bottom).



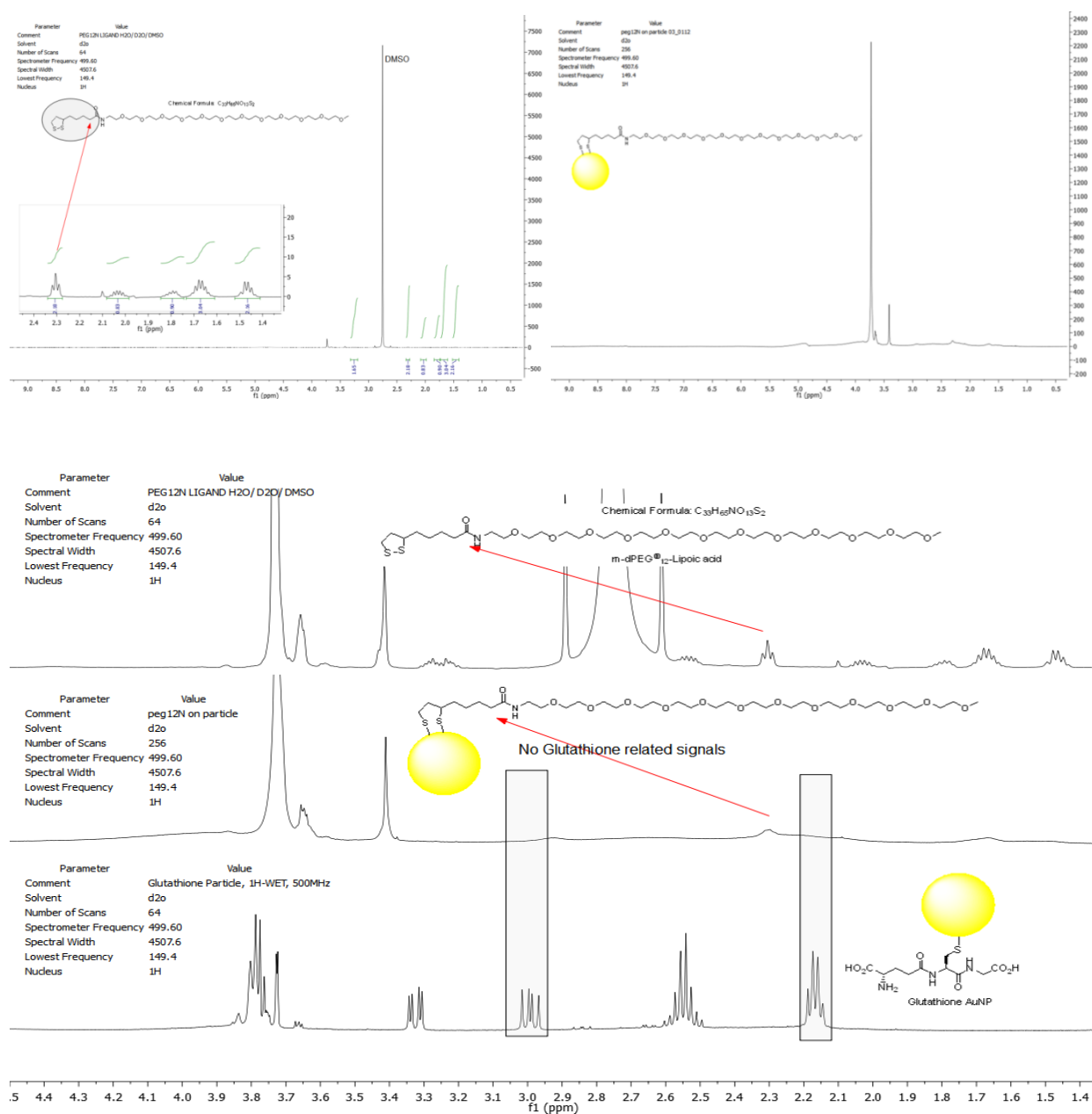
A19. ¹H NMR spectra of PEG4A ligand (top left), PEG4A ligand with integrations (top right), PEG4A nanoparticle (middle), and a stackplot of PEG4A ligand/PEG4A Au NP/ GSH Au NP (bottom). The PEG4A stackplot clearly indicates broadening of signal from PEG4A on particle, and there is no indication of any signal associated with glutathione on the Au NP. The arrows in the spectra highlight signal from protons close to the gold nanoparticle surface similar in distance as would be protons from glycine or glutamic acid proton signal from GSH.



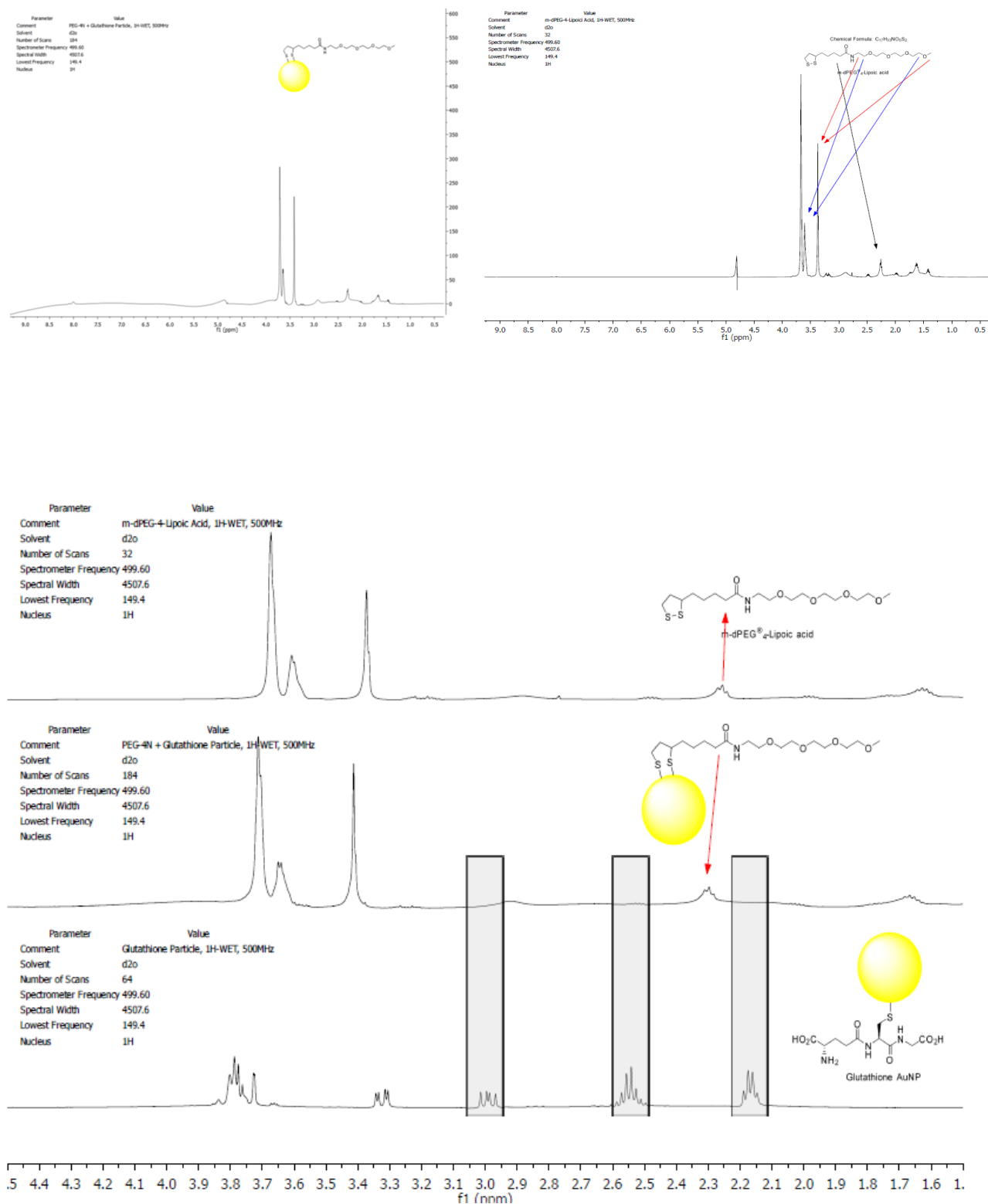
A20. ¹H NMR spectra in D₂O/H₂O of PEG12A ligand (top left), PEG12A gold nanoparticle (top right), and a stackplot of PEG12A ligand/PEG12A Au NP/GSH Au NP (bottom).



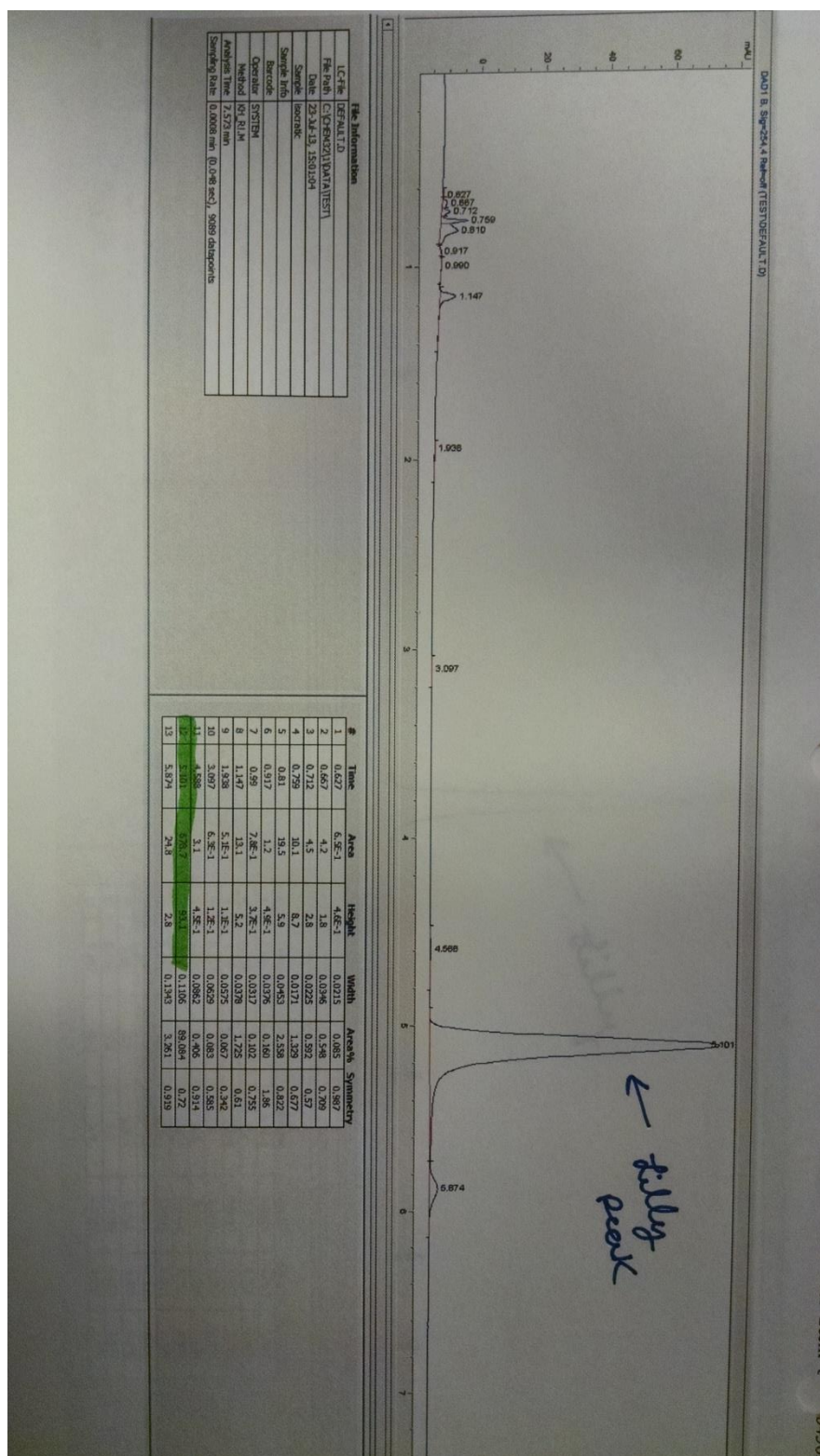
A21. ¹H NMR spectra in D₂O/H₂O of PEG24N ligand (top left), PEG24N gold nanoparticle (top right), and a stackplot of PEG24N ligand/PEG24N Au NP/GSH Au NP (bottom).



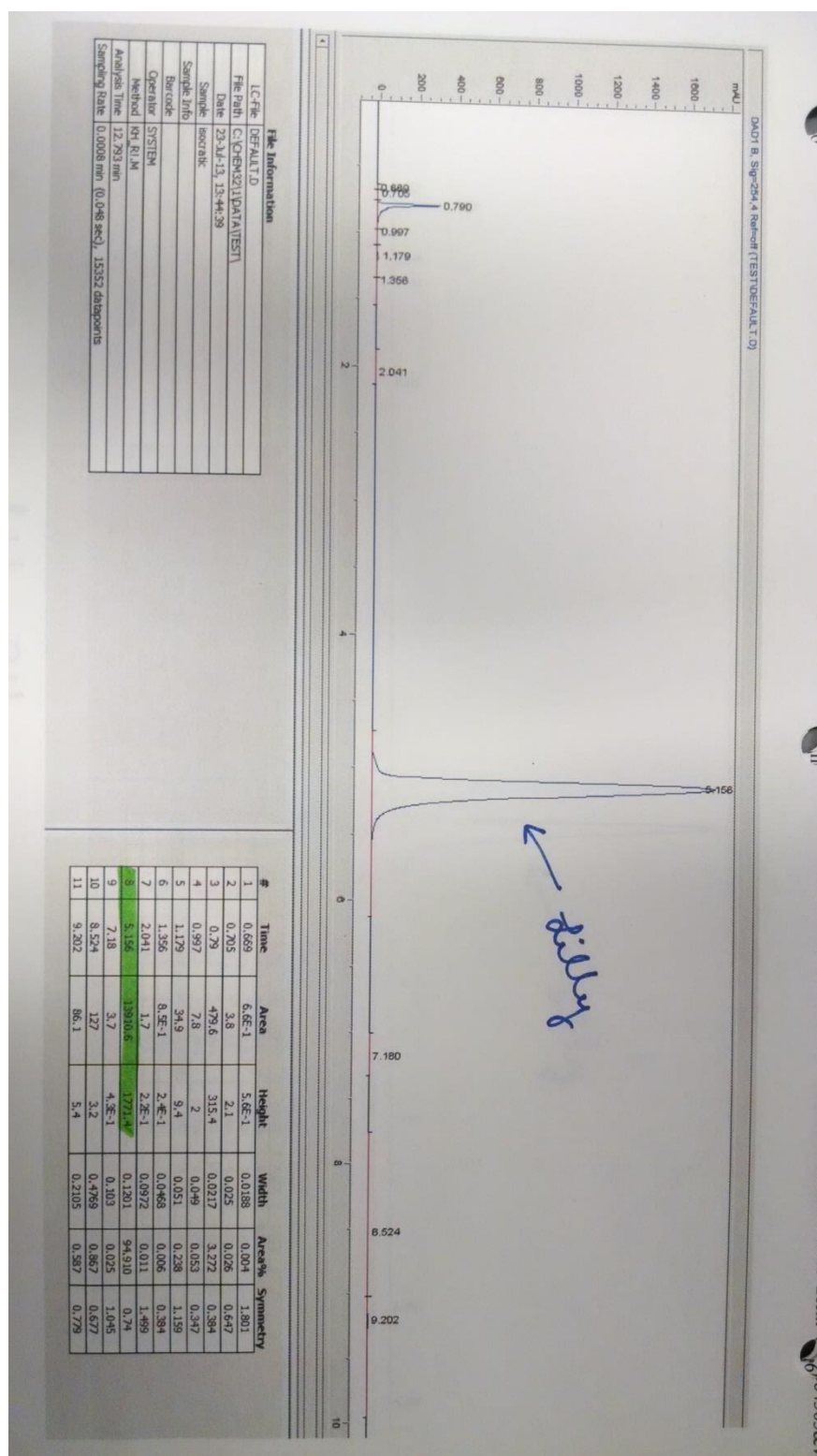
A22. ¹H NMR spectra for PEG12N ligand (top), PEG12N gold nanoparticle (middle), and a stackplot of PEG12N ligand/ PEG12N Au NP/ GSH Au NP (bottom).



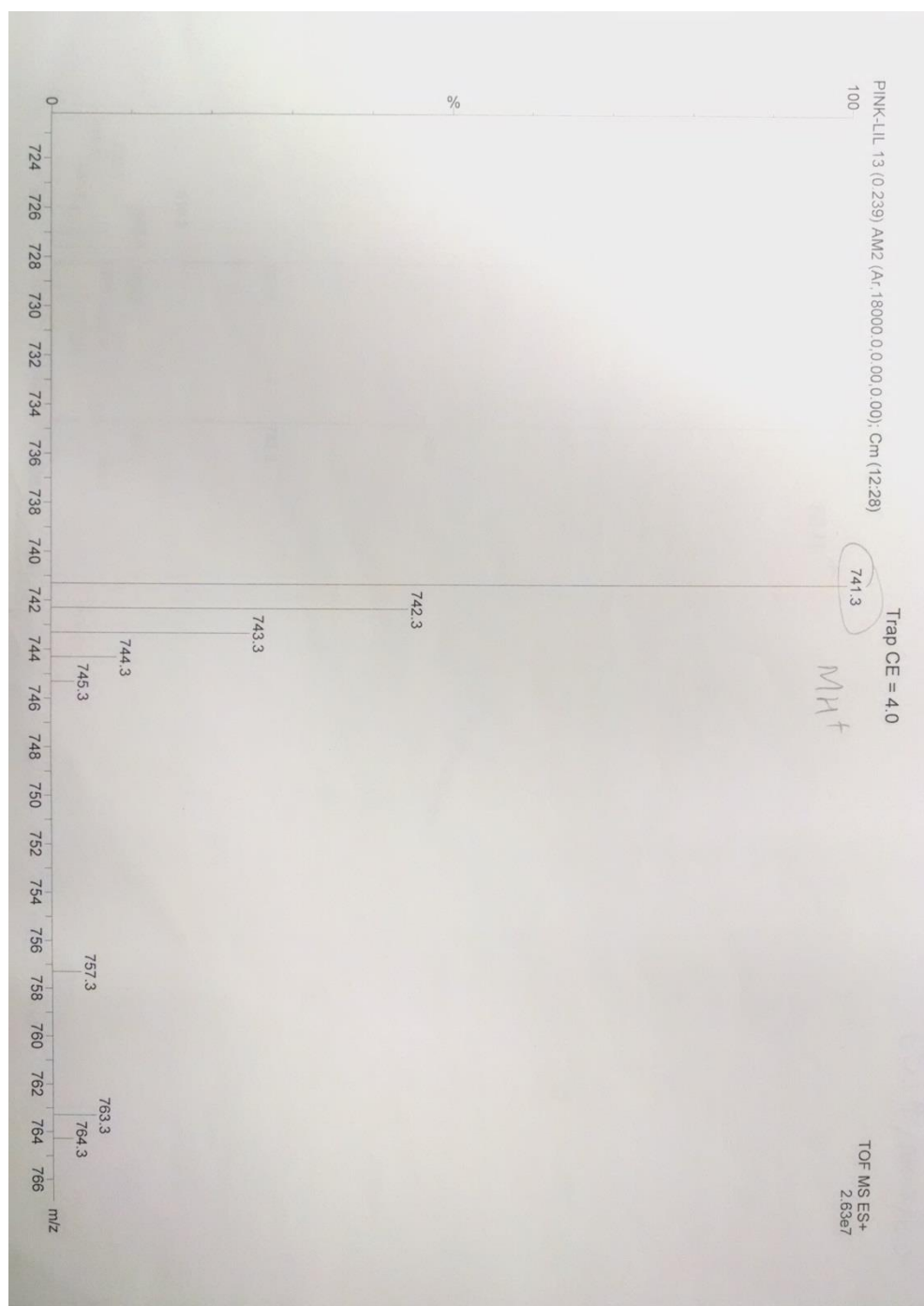
A23. ^1H NMR spectra in $\text{D}_2\text{O}/\text{H}_2\text{O}$ for PEG4N ligand (top), PEG4N gold nanoparticle (middle), and a stackplot of PEG4N ligand/ PEG4N Au NP/ GSH Au NP (bottom).



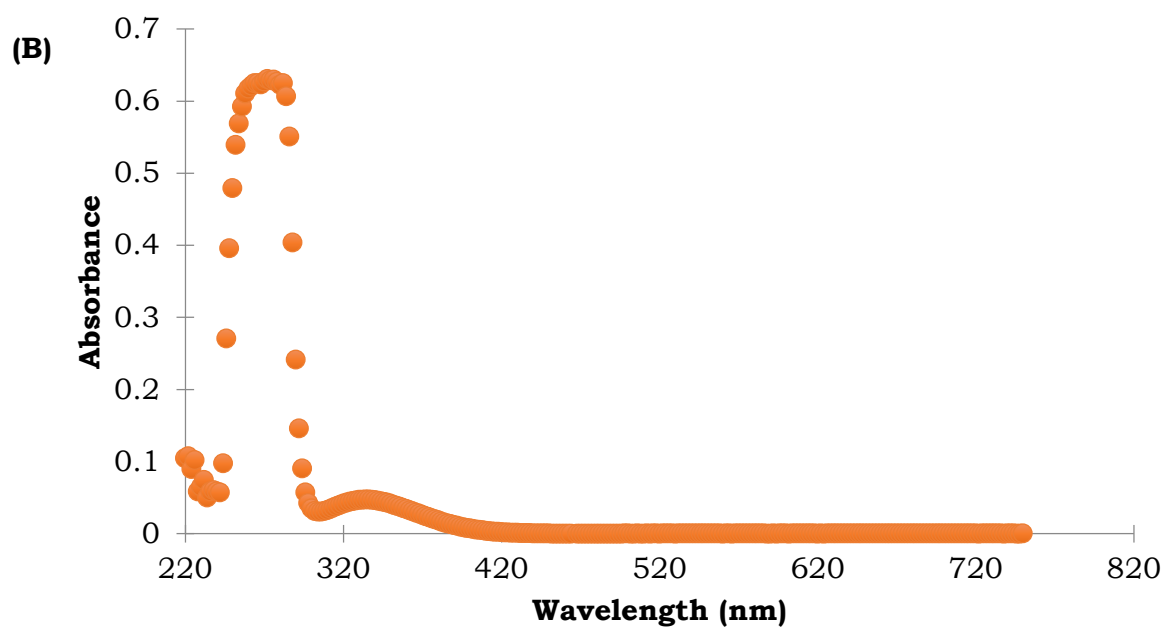
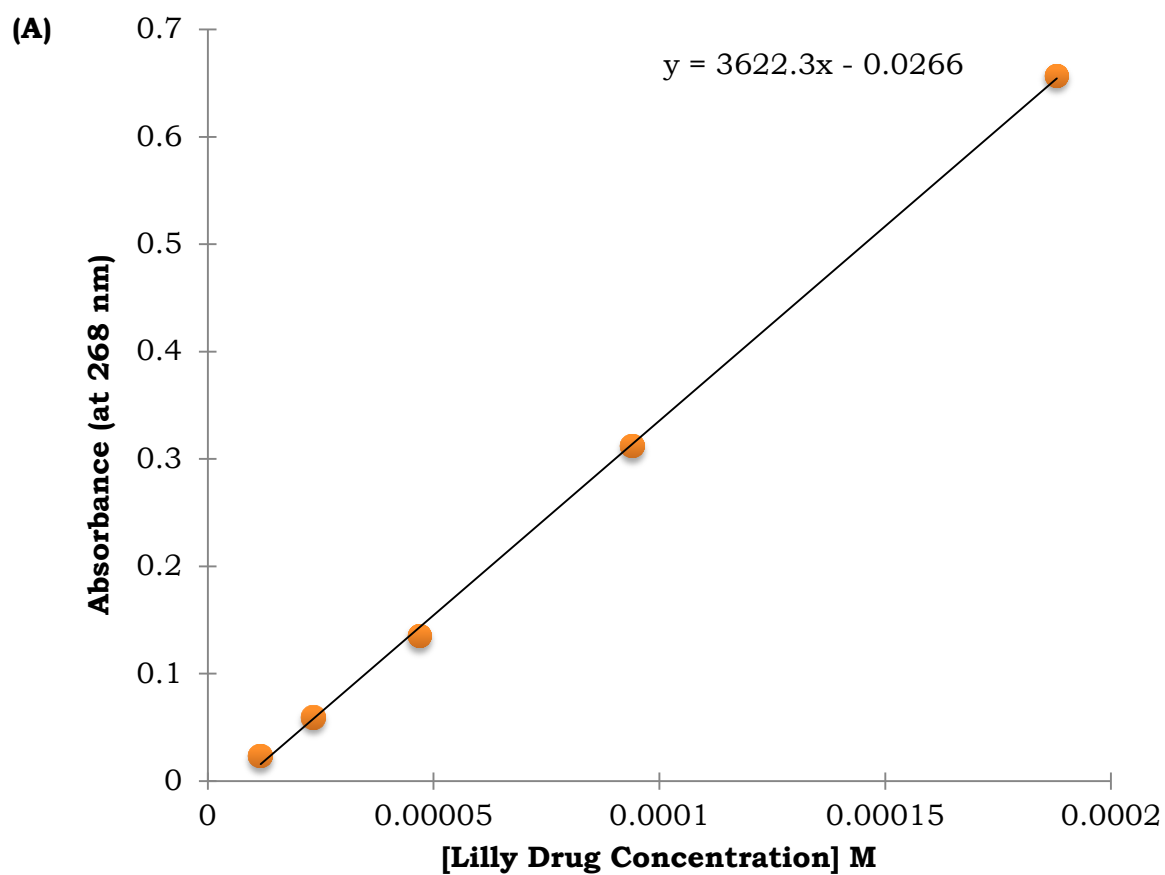
A24. HPLC chromatogram of the Eli Lilly drug thiol stock.



A25. HPLC chromatogram of the etched drug gold conjugate.



A26. LC-MS spectra of the etched gold drug conjugate. Note the peak at M/Z of 740, which matches the molecular weight of the intact drug molecule.



A27. (A) calibration curve of the Eli Lilly drug molecule

Post-exchange	Exchange solvents (% volume)					Au NP base monolayer	Exchange Ratio
Number of drug ligands on each Au NP	H ₂ O	DMSO	Glycerol	Methanol	10mM Phosphate Buffer pH 7.4		Moles ligand: moles Au NP
0	0	0.25	0	0	99.75	GSH	400:1
0	0	0.25	0	0	99.75	pMBA	400:1
0	50	0.25	25	25	0	GSH	100:1
0	50	0.25	25	25	0	pMBA	100:1
0	100, pH 5	0.25	0	0	0	pMBA	50:1
0	100, pH 5	0.25	0	0	0	GSH	200:1
2	100, pH 10	0.25	0	0	0	GSH	200:1
5	100, pH 10	0.25	0	0	0	GSH	400:1
3	90, pH 10	10	0	0	0	pMBA	100:1
6	90, pH 10	10	0	0	0	pMBA	200:1
8	90, pH 10	10	0	0	0	pMBA	400:1
11	90, pH 10	10	0	0	0	GSH	50:1
14	90, pH 10	10	0	0	0	GSH	100:1
11	90, pH 10	10	0	0	0	GSH	200:1

A28. Gold nanoparticle exchange results and conditions from different solvents. The best overall results occurred at 10% DMSO and 90% H₂O, pH 10.

(A)

The target protein, MoA related protein was observed with 89% sequence coverage:

MoA-related-His (100%), 39,024.9 Da

MoA-related-His

44 unique peptides, 82 unique spectra, 218 total spectra, 323/361 amino acids (89% coverage)

HHHHHHSSGLVPRGWSWHPQFEKENLYFQGMVIIELMRRVVGLAQQGATAEVAVYGDRDRD
LAERWCANTGNTLVRADVDQTGVGTLVRRGHPPDPASVLGPDRLPGVRLWLYTNFHCNL
CCDYCCVSSSPSTPHRELGAERIGRIVGEAARWGVRELFLTGGEPFLLPDIDTIIATCVK
QLPTTVLTNGMVFKGRGRRALES LPRGLALQISLDSATPELHDAHRGAGTWVKAVAGIRL
ALSLGFRVRVAATVASPAPGELTAFHDFLDGLGIAPGDQLVRPIALEGAASQGVALTRES
LVPEVTVTADGVYWHPVAATDERALVTRTVEPLTPALDMVSRLFAEQWTRAEEEAALFPC
A

(B)

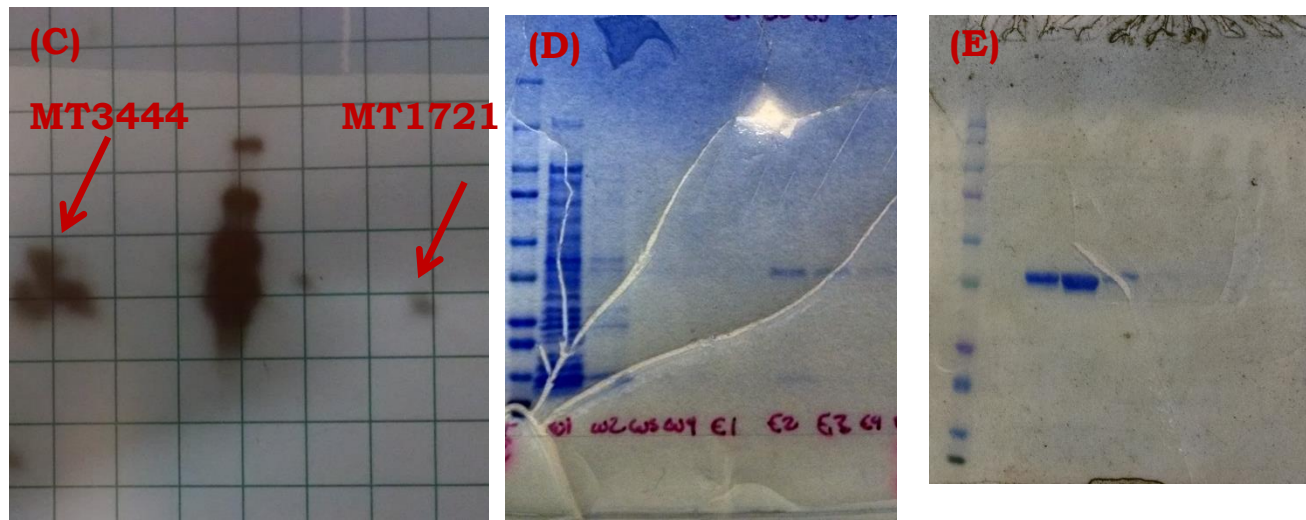
The target protein was the most abundant species in the sample and was detected with 74% sequence coverage:

MT_3444 (100%), 41,472.2 Da

MT_3444

36 unique peptides, 68 unique spectra, 239 total spectra, 290/392 amino acids (74% coverage)

WSHPQFEKENLYFQGTISDVPTQTLPAGEIGEIGLIDVGSLLQLESGAVIDDVCIQVQRWGKL
SPARDNVVVVLHALTGDSHITGPAGPGHPTPGWWDGVAGPAPIDTTRWCATNVVLGGCR
GSTGPSSLARDGKWPWGSRFPLISIRDQVQADVAALAALGITEVAADVGGSMGGARALEWV
VGYPDRVRAGLLAVGARATADQIGTQTTQIAAIKADPDWQSGDYHETGRAPDAGLRRLAR
RFAHLTYRGEIELDTRFANHNQGNEDPTAGGRYAVQSYLEHQGDKLLSRFDAGSYVILTE
ALNSHDVGRGRGGVSAALRACPPVPPVGGITSDRLYLRLQQLADLLPGCAGLRVSV
YGHGDFLVETEAVGELIRQTLGLADREGACRR



A29. Characterization data of protein TB Biomarkers MT3444 and MT1721.

(A) is the MS characterization data for MT1721 and (B) MT3444. They had significant sequence identity. (C) Western blot for MT3444 and MT1721, which indicates presence of the His tag located at the C-terminus of the protein. The band in the center is from the protein ladder used in the experiment. (D) A PAGE gel image, protein MT1721 eluted from the column in E2-E4 and the single band midway through the image is the protein of interest. (E) A PAGE gel of MT3444 after purification on a Strep-tag affinity column, the protein of interest are the single 3 bands mid-way through the gel to the right of the protein ladder.